EUROPEAN ORGANIZATION FOR NUCLEAR RESEARCH

CERN-EP/80-27
6 March 1980

PARTICLE DETECTORS

C.W. Fabjan and H.G. Fischer

CERN, Geneva, Switzerland

Submitted to Reports on Progress in Physics

EUROPEAN ORGANIZATION FOR NUCLEAR RESEARCH

CERN-EP/80-27
6 March 1980

PARTICLE DETECTORS

C.W. Fabjan and H.G. Fischer

CERN, Geneva, Switzerland

Submitted to Reports on Progress in Physics

CONTENTS

During the past decade, the methods and techniques of particle detection have seen a spectacular development. Today, the physicist dealing with a specific problem in the field of detectors is confronted with a wide and often tantalizing choice of methods, each of them offering possibilities and performances far superior to what was feasible only a few years ago. On the other hand, each method imposes it own highly developed and specialized technology in detector design and construction as well as in the fields of signal processing and data handling -- modern detectors require a highly interdisciplinary approach.

To a large extent, this development has been linked to the evolution of particle physics. If today we approach a unified picture of the basic interactions of matter, and if the impressive number of elementary particles begins to form an ordered structure, this progress in understanding has been made possible by an equally important progress in accelerator and detector physics. In fact, most of the recent detector developments have their origin in the ever-increasing demands on detection capability imposed by the modern high-energy particle physics experiments.

In this context it is interesting to note that the basic methods of detection are still the "classical" ones: very few new concepts have been added to the fundamentals of detector physics. It is the exploitation of the known methods to their limits, the full use of electronics and computer technology, and the integration of many different types of detectors into large systems that characterize the situation.

The introduction of the multiwire proportional chamber (MWPC) (Charpak 1968) which opens up our period of review is in this sense a typical example. The application of large-scale electronics (made possible by modern transistor technology) to the well-known detection technique, by means of proportional amplification in gases, created a new class of detectors that quickly revolutionarized the whole field of position-sensitive detectors and, in turn, had strong repercussions on electronics technology.

In this review we will consider the evolution of particle detectors from the point of view of the particle physicist and try to give an overview of the most remarkable recent developments in this fast-moving field of research.

1. INTRODUCTION

1.1 Purpose of detectors

In modern terms, the detection of a particle means much more than its mere localization in space. One has generally to measure its energy-momentum four vector and its quantum numbers, and to separate it from other particles in space and time.

A look at a typical high-energy physics experiment may clarify the situation.

Two primary particles collide at high energy and create a large number of secondaries (see figure 1). In this collision, a whole spectrum of elementary particles can be produced, e.g. charged and neutral hadrons of different mass, leptons, and photons.

A multitude of tasks has to be performed in order to extract the necessary information on each of the particles:

- the charged particle trajectories have to be localized in space, i.e. their space coordinates and directions have to be measured;
- to measure charge and momentum, a curvature on each trajectory in a magnetic field has to be determined;
- a simultaneous measurement of momentum and energy or momentum and velocity determines the particle mass;
- the energy, direction, and nature of the neutral particles have to be obtained;
- the details of each particle's interaction with matter, be it strong, weak, or electromagnetic, are used in its classification within the hierarchy of elementary states.

Usually, the space density of secondaries is high. Therefore the detectors must be able to separate near-by particles in space, a task quite different from the one of space resolution. Also, the density of events in time -- the interaction rate -- is frequently high, and may severely limit the choice of detectors. Therefore the time separation capability is of great importance in planning the layout and efficient use of a detector system.

The variety of tasks outlined above cannot be met by a single type of detector. The trend has therefore been to develop detector systems which integrate many different methods of detection in an often complex layout.

1.2 Means of detection

Each method of detection has to use the particle interaction with the detector medium in order to create an observable signal. This interaction will change some of the quantities that characterize the detected particle: it may lose some of its energy, it may change its direction of movement, or it may even change its identity during the detection process.

We have emphasized that particle detection means in general the measurement of several observables in distinct measuring processes. We will therefore subdivide the detection methods into two broad classes: the non-destructive methods, which allow multiple measurements to be performed without changing the identity of the detected particle; and the destructive methods, which destroy the particle identity during its detection.

All neutral particles have to be detected by the latter method: photons have to be transformed into charged particles by the electromagnetic interaction; neutral hadrons have to decay or interact through the strong or weak interaction in order to become observable; and neutrinos can only be detected by their weak interaction with matter. These interaction cross-sections may be quite small, and therefore most destructive methods employ large amounts of material in dense detectors that aim at high conversion efficiency and at absorbing all the produced secondary particles. A multitude of detectors for electromagnetic and hadronic cascades have been developed during the past years.

In contrast, it is the electromagnetic interaction of charged particles with matter that allows non-destructive observation. The interaction cross-section is high enough to leave detectable signals even in very small layers of material, with negligible or small energy loss of the detected particle.

Many of the non-destructive methods are based on the energy loss of charged particles by excitation and ionization. The Čerenkov effect and, more recently, the detection of transition radiation, present additional detection methods that are sensitive to the particle velocity.

1.3 Information processing

One of the most striking consequences of modern detector technology is the very high information rate that is created by the detectors and which has to be stored and processed before one can evaluate the experimental data.

Typical of recent high-energy physics experiments (figure 1) are the large amounts of digital and analog data which are recorded for every event. Each of the many particle trajectories is characterized by a number of coordinates from the position-sensitive detectors, for instance in the form of digital wire addresses in a multiwire chamber. Often, this information is obtained in more indirect ways, e.g. as a ratio of analog signals or as a drift time measurement.

Detector systems with many thousand digital and analog signal channels are now in common use, generating for each event a data flow of several hundred or thousand logical words. These data have to be channelled through on-line computers and stored on data storage devices, typically on magnetic tapes. Since this data transmission is limited in speed, the filtering of information has gained in importance. Sophisticated trigger systems, working on the raw data from the detectors at different levels of logic decisions, are employed to match the rate of primary interactions with the data transmission speed.

The task of reconstructing the physical event out of a multitude of logical bits of information stored on magnetic tape has become a major limit in experimentation. Today's fastest and biggest computers frequently need more time to reconstruct an event off-line than was needed to record it on-line in the experiment. This difficulty is partly due to the formidable problem of pattern recognition, i.e. the reconstruction of particle trajectories from logical information in a complicated environment of detectors and magnetic fields. It is also caused by the trend to use more refined analysis methods for the detector information.

The problem of data analysis has strongly influenced the development and layout of detectors: computer processing of particle events has to be considered together with the experimental apparatus, requiring careful optimization already at the design phase of such a detector system.

1.4 Layout of review

This review is subdivided into two parts on detection methods and one on detector systems. The section on non-destructive methods will deal with detection by energy loss, Čerenkov radiation, and transition radiation. The one on destructive methods will describe the detection of particle cascades induced by leptons and hadrons. The section on detector systems attempts an overview of the utilization of detectors and the problems connected with it: the flow of information from the detectors to the data storage devices; the role of electronics and computers both in data transmission and in data analysis. The complexity of modern detector systems and the corresponding interplay of different techniques will be illustrated by some typical examples. An outlook on future trends will conclude the article.

2. NON-DESTRUCTIVE DETECTION METHODS

2.1 Energy loss of charged particles

Charged particles traversing matter lose energy mainly by collisions with the atomic electrons of the medium, leading to excitation and ionization. At high velocity $\beta = v/c$, $\beta > 1/n$, where n is the refraction index of the medium, Čerenkov radiation starts to contribute. At very high velocities, $\gamma = (1 - \beta)^{-1/2} \gtrsim 1000$, transition radiation (i.e. radiation emitted upon the traversal of interfaces between different media) becomes detectable. All these manifestations of the electromagnetic interaction are used for particle detection, provided that the corresponding energy loss is high enough to leave detectable signals in the medium. Since this energy loss is a unique function of the particle velocity β and not of the particle mass m, a combined measurement of momentum $p = mv$ and energy loss provides information on the mass and hence on the identity of a particle.

2.2 Energy loss by excitation and ionization

The energy loss due to atomic collisions in thin samples of matter is a statistical process: it displays, in general, a wide, non-Gaussian distribution (Landau 1944) around a mean value (Bohr 1913, Bethe 1930).

The theory of the mean energy loss was developed during the last 50 years (Bethe 1933, Fermi 1940, Sternheimer 1952, 1956, 1971, Crispin 1970). Typical of this is the dependence on $\beta\gamma = p/mc$ of the mean energy loss, as shown in figure 2 for gaseous argon. For $\beta\gamma < 2$, the energy loss drops as β^{-2} for all media. With the onset of relativistic effects, it reaches a characteristic minimum at around $\beta\gamma = 3$ and then shows a logarithmic increase ("relativistic rise") which flattens out in the region $\beta\gamma \gtrsim 100$ ("Fermi plateau"). The height and onset of the plateau depend on the nature and density of the medium.

Recently, considerable interest has been shown in the possibility of identifying particles by energy loss measurement over the β-range of the relativistic rise. The height and onset of the Fermi plateau have been calculated for a wide range of solid, liquid, and gaseous media. Comparison with measurements (Crispin 1970, Chechin 1972, Cobb 1976), notably in gases (Allison 1976, Lehraus 1978) and at different gas pressures (Walenta 1979), show good agreement of the calculations.

For all measurements of energy loss, the fluctuation around the mean value (the "Landau fluctuation") has to be taken into account. Although a reasonable description of the energy loss distribution in dense media was achieved rather early (Vavilov 1957, Blunck 1950), the fluctuations at very small detector thickness and density (gases) were not properly predicted. Recently, the detailed treatment of shell effects using Monte Carlo techniques (Cobb 1976, Chechin 1976) and analytical methods (Talman 1978) has established good agreement with experiment for thin gas samples.

In conclusion, it can be said that the detailed features of the mean energy loss by ionization and excitation, and its fluctuation, are today well understood and can be reliably predicted for most detector applications over the full range of particle velocities.

2.3 Detection of excitation

The detection of excitation light quanta in transparent media became possible with the introduction of the photomultiplier about 30 years ago (see the historical reviews by Hofstadter 1975 and Morton 1975). The conversion of excitation energy into luminescent light emission (scintillation) is a rather complex process

that has been investigated in a wide range of media, from noble gases to anorganic single crystals and organic liquids and plastics (Birks 1964, Heath 1979, Brooks 1979). Since the scintillation signal is prompt and its decay time only of the order of 10^{-9} to 10^{-6} s, depending on the medium, scintillation counters are ideal instruments for precise timing measurements and high-rate experimentation. In addition, the light output is proportional to the energy loss of the detected particle in most applications. Because of these features, scintillation counters have been the universal detectors in every field of particle physics over the last 30 years. They have been at the origin of many of the modern developments in fast electronics circuitry and pulse analysis, especially in analog-to-digital and time-to-digital conversion.

More recently, their application for position measurement has somewhat declined with the evolution of the multiwire chambers. Nevertheless they are still indispensable as time-reference and triggering devices, and their use in total absorption calorimetry has led to the conception of very large systems with many hundreds of photomultipliers.

Owing to these developments, the emphasis of recent research has been on the improvement of timing capabilities on the one hand, and the introduction of low-price scintillator materials and new read-out methods for large-scale applications on the other.

The identification of particle mass by time-of-flight (TOF) measurement, i.e. simultaneous determination of momentum and velocity, is a well-established method in the region of low and medium momenta, up to approximately 1 to 2 GeV/c. The limits are imposed by the permissible flight path in an experiment and by the achievable timing precision. Organic scintillators coupled to fast photomultipliers are capable of time resolutions of the order of 0.2 ns FWHM (Lynch 1975). The outstanding problem arises if one tries to achieve this with large systems with many square metres of scintillator and up to 100 phototubes -- a common situation in high-energy physics experiments. However, Braunschweig et al. (1976) have shown that a resolution of 0.6 ns FWHM is possible in large systems. Here, careful optimization of scintillator dimensions and light collection (Massam 1977)

onto two tubes per scintillator are needed. Regular procedures for calibration and gain control are equally important. In this context, calibration systems using fast flash-lamps or laser pulses coupled via fibre optics are being developed.

For very precise timing measurements, the channel-plate multipliers (Pietri 1977) have been available for some years. Here, the focusing dynode structure of the classical photomultiplier is replaced by a flat plate with thin (about 20 μm) and short (about 40 times the diameter) microscopic channels (figure 3). By having a combination of, typically, two plates, very fast multipliers with gains above 10^6 and transit times of the order of 1 ns can be achieved (Lo 1977). These devices have a timing resolution in the 0.1 ns range and are very insensitive to external magnetic fields -- one of the major drawbacks of conventional phototubes.

Its promising features notwithstanding, the channel-plate multiplier has not yet become a standard detector component (Lecomte 1978). This is in part due to its high price, in part to rate limitations and long-term stability problems (Meunier 1978).

For applications of large-volume scintillation devices, the prohibitive cost of anorganic single crystals such as NaI(Tl) or high-quality organic plastics have led to the development of scintillators on a polystyrene or acryl base; these bases are doped with variable concentrations of scintillating chemicals and wavelength shifting agents to adjust light output and attenuation length (Thévenin 1979). In addition, very elegant methods for optimum light collection from very large scintillators (Garwin 1960, Barish 1977) or scintillator stacks (Atwood 1976, Eckardt 1978) have been examined. The light from the scintillator sheets is coupled across an air gap into a "wave-shifter" sheet where it is absorbed and isotropically re-emitted at increased wavelength. Because of total reflection, a large part of the re-emitted light is trapped inside the sheet and is guided with high efficiency to the photomultiplier. Many independent scintillators can thus be connected to a single phototube. Extremely large assemblies using tons of scintillator and up to several thousand multipliers are under construction for calorimetric applications (see § 3).

The scintillation properties of noble gases have recently been studied for novel detector applications. The direct excitation light from charged particles is normally regarded as a detrimental background for other detection methods, for instance in Čerenkov counters. If, however, the ionization electrons are accelerated in modest electric fields below the onset of secondary multiplication, they will induce gas scintillation on the level of, typically, 10 to 100 photons per electron. This avoids the large fluctuations in the avalanche process and can be used for high-resolution spectroscopy (Policarpo 1977), especially for space physics applications (Andresen 1977).

Gas scintillation can also help to reduce the counting-rate limits of multiwire proportional chambers (MWPC) (§ 2.4) by avoiding space-charge saturation. Its use in high-rate, high-precision detectors has been studied by Charpak (1975).

2.4 Detection of ionization

From the detection point of view, ionization appears as a two-step process: in the first step, primary electron-ion pairs are created in the atomic collisions of the detected particle with the medium. In the second step, the energy of the primary electrons (with a spectrum following roughly a $1/E^2$ law) is dissipated into secondary ionization. It is by this process that the produced total ionization becomes proportional to the energy loss of the detected particle.

At minimum ionization, the number of primary collisions n_p is of the order of a few thousand per g/cm^2 traversed in gases, liquids, or solids. Exact values have been calculated for a few gases only and are rather difficult to measure (Ermilova 1969; see also Sauli 1977). Since the rate of primary collisions follows Poisson statistics, the inefficiency of a detector is given by $\exp(-n_p)$ which imposes, at least for gaseous detectors, a lower limit of detector thickness.

In contrast, the total number of ion pairs n_T is well known for most media through the dosimetric measurements of W, the effective energy needed to produce one ion pair, and the mean energy loss ΔE: $n_T = \Delta E/W$ (Christophorou 1971). In comparing n_T and n_p it is found that on the average each primary electron creates three or four secondaries.

Since the range of primary ionization electrons -- except for a few high-energy "delta-rays" -- is usually small compared to the mean distance of ionizing collisions, we obtain in the medium a number of ionization clusters along the particle trajectory. This track image is made directly visible by the bubble chamber and the avalanche or streamer chamber techniques. In most detectors, however, the total ionization is collected onto electrodes by an electric field. Here, the detection limit is given by the input sensitivity of the recording device. Modern charge amplifiers are sensitive to a few 10^2 to 10^3 electrons (Radeka 1974, Brandt 1977). The direct collection of ionization (ion chamber technique) is therefore limited to dense media or to highly ionizing particles. In gases, one has to use the gas amplification process by avalanche formation in high electric fields. Amplification factors up to 10^4 can be achieved in the proportional mode, i.e. the amplified charge being strictly proportional to the initial ionization. In this regime, there is therefore sensitivity to a few primary ionization electrons. For gas amplifications above 10^5, a wide regime of transition into streamer or spark formation sets in, which is used in flash-tube detectors, in avalanche and streamer chambers, and in spark chambers.

2.4.1 Bubble chambers

For more than 20 years the bubble chamber has been an indispensable tool of the particle physicist for studying complex multiparticle events. The principle of bubble formation around ionizing tracks in superheated fluids was discovered by Glaser (1952). In the subsequent years an impressive technological development has allowed the construction of bigger and bigger chambers, culminating in the huge bubble chambers at CERN and the Fermi National Accelerator Laboratory (Reinhard 1973) which contain many cubic metres of liquid in strong magnetic fields and thus form a large, completely homogeneous, detector medium.

Today the bubble chamber is still unmatched in its capability for track reconstruction and particle identification. The primary ionization clusters along the trajectories (see § 2.2) give rise to bubbles such that energy loss measurements by bubble-density counting permit mass identification up to $\beta \sim 0.8$ and,

for some liquids, in the region of relativistic rise (Chechin 1972). The development of the Track-Sensitive Target technology (Leutz 1966, Fisher 1973) has permitted a decisive improvement in identification capabilities: the combination of a liquid-hydrogen target section with a surrounding heavy liquid (neon) in the same chamber volume provides effective photon detection by pair conversion.

Since all the information is stored with high precision on photographic film, complete track reconstruction, even in the presence of severe background, and very efficient observation of secondary decay vertices from neutral and charged short-lived particles are feasible. A demonstration of the capabilities is given in figure 4. A neutrino reaction in the Big European Bubble Chamber (BEBC) has produced a heavy meson of the recently discovered "charm" family. The complex production and decay pattern of the event can be followed in every detail.

In spite of all these advantages, the use of bubble chambers in high-energy physics has somewhat diminished during the past years in favour of the purely electronic detectors. There are several reasons for this development:

- the bubble chamber cannot be used as a selective, triggerable detector;
- it has a low repetition rate (of the order of 1 to 10 per second);
- the reconstruction time of events from the film is slow, of the order of 10^5 events per year on automatic measuring devices;
- high-momentum particles from the modern accelerators cannot be measured in the chamber volume alone;
- bubble chambers cannot be used at colliding beam accelerators.

Consequently, most of the medium-size chambers have been taken out of operation during the last years. The big chambers are mainly used for neutrino physics with its low event rates. In addition, they are equipped with a variety of external detectors such as muon identifiers (Brand 1976) or hadron identifiers (Lehraus 1978).

The attempt to combine the unique features of the bubble chamber as a vertex detector with the versatility of electronic detectors in selecting rare events and improving the particle identification and momentum accuracy at very high

energies, has evolved into special "hybrid" systems. At the heart of these combined systems is a rapid-cycling bubble chamber with a repetition rate in the 10 to 100 Hz region (Ballam 1966, Fisher 1973). The surrounding detectors provide a trigger so that only the interesting events are selected for recording on film. Hybrid systems are operational at most of the major high-energy physics laboratories (see the recent review of Ballam 1977). The most sophisticated system is being constructed at CERN as a major European research facility (Montanet 1976). The evolution of the bubble chambers from stand-alone devices to integrated systems combining the advantages of many different types of detectors is a typical example of the recent trend in detector physics.

2.4.2 Ionization chambers

The detection of ionization by charge collection in ionization chambers has an extremely widespread range of applications. Gaseous, liquid, and solid detector media can be used to adjust detection efficiency and energy loss resolution to a variety of different projectiles, from the fast, minimum-ionizing particle to the heavy nuclear fragment.

Because of the low number of primary ionization collisions in gases, the classic gas ionization chamber (Curran 1965) has been limited to low-energy, heavy particles, and much of its attraction has been lost to the competing scintillation counter or solid-state detector methods. With the advent of the heavy ion accelerators, however, it has gained new importance (Fulbright 1979) for the detection of high specific ionizations. Its version as a parallel-plate, low-pressure avalanche chamber (Eyal 1978, Breskin 1978) is a high-efficiency device with sub-nanosecond time resolution, using the avalanche formation in flat electrode geometry.

Following the pioneering work of Willis (1974), the liquid-argon ionization chambers have found extensive use in high-energy physics experiments. Its application as a sampling device for electromagnetic shower detectors is described in § 3.4. Charge amplifiers with a sensitivity of 10^4 electrons (Radeka 1974) are needed for the detection of minimum-ionizing tracks. To avoid electron capture

the detector liquid has to be free of impurities at a level of a few ppm of oxygen for a drift of some millimetres. Nevertheless, studies for large-volume liquid ion chambers have been undertaken (Chen 1978, Gruhn 1978). Knies (1976) has investigated the possibility of particle identification by energy loss measurements in single gaps. Finally, the ion chamber application can be extended to solid media. On the one hand, solids offer high total ionization due to the low energy W needed per ion pair ($W \sim 3$ eV compared to $W \sim 30$ eV in gases). On the other hand, the impurity problem becomes even more severe than in fluid media.

Pisarev (1973) and Cobb (1977a) have demonstrated charge collection from solid argon and xenon.

It is, however, in the regime of semiconducting materials that the technique is most extensively used. Since 1960, semiconductor counters have become the standard detectors for nuclear radiation (McKenzie 1979). The idea is to use one or more semiconductor junctions in reverse bias. A depleted zone, free of carriers, is thus created which acts as ionization chamber: the excessive bulk current across the device is reduced to a small leakage current which permits the detection of the very small ionization signal. The effective thickness of the counter can vary from a few microns to more than one centimetre. Here, the impurity concentration becomes the major limitation: the high-purity germanium used for large depth counters is the purest material produced so far (1 part in 10^{13}).

Owing to their limited thickness and size, the use of semiconductors has been essentially limited to nuclear physics applications. For recent reviews, see Ewan (1979), Laegsgaard (1979).

2.4.3 Multiwire proportional chambers

During the past decade, no part of detector physics has been developed as extensively as the one using proportional amplification in gases. It is only 10 years ago that Charpak introduced the first MWPC (Charpak 1968, Charpak 1970a). Today, the class of track-sensitive detectors is dominated by multiwire structures operated in the proportional mode. These detectors come in an incredible variety:

from the small, high-precision device to the giant multi-square-metre drift chamber; from wire systems involving up to 10^5 individual read-out channels to the large-volume drift chambers collecting complete track images over metres of drift; from the digital device yielding simple coordinate information to the analog methods measuring coordinates and energy loss of the detected particles simultaneously.

The underlying physics principles, i.e. the drift and collection of electrons in gases, the mechanism of avalanche formation in high electric fields, and the formation of the corresponding electric signals on the collecting electrodes, have been known since a long time. Indeed the "classic" textbooks on these phenomena, e.g. Wilkinson (1950), Loeb (1961), Raether (1964), are still valid and have gained new importance and relevance.

The application of these principles to large-scale detectors, however, has only become possible very recently through the revolutionary developments in transistor electronics and computer technology. The linear amplification of fast signals requiring a sensitivity of femtocoulomb, the time-to-digital conversion with nanosecond resolution, and the analog-to-digital conversion with good linearity and high accuracy, have been limited until recently to expensive, laboratory-scale apparatus. Today, hundreds or even thousands of electronic channels fulfilling these functions can be employed owing to the rapid decrease in the cost of electronic components and the progress in large-scale integration. This gives the detector designer the freedom to perform (almost) any electronic manipulation with the signals from his chambers -- hence the large variety of different detector solutions.

i) Gas amplification, charge collection, and pulse formation

In all proportional detectors, the gas amplification takes place in the high electric field surrounding thin "sense" wires (diameter typically 10 to 50 μm). Efforts to use point-like amplification zones, e.g. needle points, have not yet reached large-scale application (Grunberg 1974, Comby 1979). Whatever the arrangement of the surrounding electrodes, the field in the immediate neighbourhood of

the sense wires will vary as 1/r and thus provide the high field levels of 10^4-10^5 V/cm necessary for avalanche formation. The field shape at some distance from the sense wires is essentially determined by the global distribution of electric potentials in the detector, i.e. the electrode geometry (see classic textbooks on electrostatics, e.g. Buchholz 1957).

The simple layout of a planar multiwire chamber is shown in figure 5. A series of sense wires (at a distance of typically 1 to 10 mm) are sandwiched between two flat cathode planes. The corresponding field distribution yields a homogeneous "drift" field over most of the chamber volume and a cylindrical field concentrated around the sense wires (Erskine 1972).

Planar multiwire chambers had been operated in the proportional mode many years ago (Rossi 1949). However, Charpak (1968) was the first to show that each sense wire acts as an independent detector. An avalanche formed close to a wire induces, by the motion of the positive ions in the field, a negative signal on this wire only and corresponding positive signals on all other electrodes. The capacitive cross-coupling of negative signals, which would spoil the space correlation, is thereby eliminated.

It took some time to understand the exact distribution of induced charges in space and time over the electrodes in a given detector geometry. The negative signal on the anode wire is formed by the time overlap of subsequent avalanches from the ionization electrons drifting into the high-field region. The rise-time of the current pulse from one avalanche is given by the electron mobility and is of the order of 100 ps. The decay time constant (given negligible influence from the detector electronics) is determined by the ion mobility and is of order 20 ns. Modern fast amplifiers allow a detailed study of this superposition mechanism (Fischer 1975, Frehse 1978 and Walenta 1978). Figure 6 shows the time-structure of a chamber signal from a minimum-ionizing particle as it is measured and calculated.

The space distribution of the induced signal over cathode and anode wires has only recently been clarified. Charpak (1978b) and Fischer (1978) have shown

that all electrodes except the anode wire creating the avalanche receive positive induced signals even if the avalanche does not surround the wire. The height and time development of the induced pulse depends, however, on the position of the avalanche relative to the different electrodes. This has been used to obtain the space position of avalanches with impressive accuracies in the range of 60 μm (Charpak 1979b).

ii) Drift chambers

The relation between the position of the ionization column created by a particle and its collection time on the sensitive wires can be used for accurate position measurements. This possibility was realized immediately with the introduction of multiwire chambers (Charpak 1968, 1970b, Walenta 1971). The typical geometry of a planar "drift" chamber is shown in figure 7. The electrode configuration is chosen such that a uniform drift field towards the sensitive wires is created, resulting in a linear relationship between distance and drift time. In typical detector gases and drift fields, a timing accuracy of a few nanoseconds is sufficient to reach space resolutions of the order of 100 μm.

The necessity of a constant drift field introduces heavy constraints on the electrode configuration and chamber construction. This problem can be partly eliminated by the choice of gas mixtures with constant electron mobility at least over a certain range of electric fields (Breskin 1975, Schultz 1977). Another problem is the influence of external magnetic fields (as they are present in most track-sensitive detector arrangements) on the drift direction (Breskin 1975). Finally, in view of the rather large drift distances (typically of the order of 10 cm), the electron diffusion imposes an ultimate limit on the space accuracy and a constraint on the choice of the detector gas (Sauli 1978).

Recent research on the problem of electron drift in gases (Palladino 1975, Schultz 1977) has provided some guidance in the choice of optimum gas mixtures (Heintze 1978). However, new operating modes of MWPCs, such as ionization measurement, and exposure to high particle rates and strong magnetic fields, indicate the necessity for further research into the fundamentals of ion-pair creation and migration.

iii) A look at the geometries of wire chambers

The planar wire structures shown in figures 5 and 7 have been only a starting point in the development of more complex detector geometries. Today, a detector configuration can be tailored to meet the specific demands of the experimentalist. A good example is again given by the detection problem posed by the multiparticle reaction shown in figure 1. In order to detect and reconstruct the particle trajectories emerging from a common vertex, one can simply arrange planar multiwire chambers in a box-like structure (figure 8a). Subsequent planes may have different wire orientation to obtain track determination in space. Large systems of this kind with up to 10^5 sensitive wires (Bouclier 1974) have been constructed and used successfully for high-multiplicity events. The technique can be extended to drift chambers measuring the track position and angle simultaneously (Ceradini 1978).

The next step is the construction of cylindrical proportional or drift chambers (Criegee 1975, Camilleri 1978) (see figure 8b). This idea has been pursued up to the introduction of low-density cylindrical chambers with open field geometry, where the number of potential wires is kept to a bare minimum and almost the whole chamber volume can be used for detection (Sadoulet 1975, DeBoer 1978, Davies-White 1979).

In cylindrical geometry, the measurement of the coordinate along the cylinder axis poses a problem. It can be solved by using the charge division technique on the sense wires (Fischer 1976, Fabjan 1978), by detecting the induced pulse on cathode strips (Fischer 1972, Criegee 1975) or on delay lines along the sense wires (Camilleri 1978). One can also achieve a "small-angle stereo" read-out by stretching wires, with a small angle of inclination, against the cylinder axis (Davies-White 1979).

Another wire geometry is used in the "jet chamber" (Heintze 1978, Fabjan 1978) where the wire planes are arranged radially (see figure 8c) to form wedge-like drift cells. The particle trajectories run nearly parallel to the wire planes, and the high space accuracy along the drift direction can be used for multiparticle separation and energy loss measurements.

The most radical development up to now in the field of multiparticle detectors is the time-projection chamber (Fancher 1979, Allison 1978, Rubbia 1978) (figure 8d). Here, the only sensitive element in a large drift volume is a single planar multiwire chamber. Complete track images formed by the ionization of the detector gas are drifted onto the wire plane by a strong electric field (100 kV/m). By using two-dimensional read-out of the pick-up chamber and the drift-time information, it is possible to reconstruct the complete three-dimensional trajectory ("time projection"). The undistorted drift over large gas volumes, and the simultaneous recording of time and charge for a multitude of tracks and electronic channels, exploit the state of the art of detector technology to its limits.

iv) Multiple energy loss detectors

The possibility of mass determination using the velocity-dependence of the energy loss has been mentioned in § 2.2. The application of this idea in the region of the relativistic rise is notoriously difficult: dense detector media show little or no relativistic rise, and in gaseous detectors one has to measure a small effect (of the order of a few percent) in the presence of considerable Landau fluctuations (typically 80% per detector cell). In order to reduce the energy loss fluctuations, it is necessary to measure the ionization loss in many samples over a large depth of gas: calculations show (Aderholz 1974, Cobb 1976) that several hundred samples over some metres of gas are needed to bring the level of fluctuations down to a few percent.

The first full-scale instrument which proved the feasibility of the method is the external particle identifier (EPI) working behind BEBC at CERN (Lehraus 1978). Figure 9 shows the separation of 50 GeV/c protons and pions achieved with 6% FWHM resolution.

ISIS, a large device of the time-projection type, is nearing completion (Allison 1978) and has shown encouraging results in a prototype stage (Allison 1979). Operation of other detectors, notably the time-projection chamber (Fancher 1979) and the "jet" drift chambers (Heintze 1978) will soon contribute experience to a field that is being vigorously explored in many laboratories.

v) Limits of the wire chamber technology

In the early days of wire chamber development, the construction and operation of wire systems used to have a touch of mystery. Today, an impressive body of practical experience has been accumulated, such that the sometimes "magic" rules of individual craftmanship can be replaced more and more by safe and well-understood procedures [a recent review on these problems has been given by Sauli (1977)].

There is no doubt that multiwire chambers are delicate instruments: large quantities of fragile wires (in some detectors up to a total of 100 km) are stretched to the limits of tensile strength in very high electrostatic fields, and are subjected to constant bombardment by intensive ionizing radiation.

This leads first of all to mechanical problems. The chamber mechanics defines the field geometry and the position accuracy of the detector. The electrodes have to be kept in stable equilibrium, and the question of electrostatic forces is one of the limiting factors in each specific field geometry (Trippe 1969, Sauli 1977). The positioning tolerances imposed by drift chambers are of the order of 50 μm for devices of typically several metres linear dimensions.

The more fundamental limitations are, however, imposed by the physics and chemistry of amplification and breakdown in gases.

It has recently been shown that the regime of proportional gas amplification is limited by space-charge saturation to values of the order of 10^3-10^4 (Breskin 1975, Frehse 1978, Kroeger 1978). Analog applications, for instance energy loss measurements, are therefore confined to the regime of low gas amplification, which demands electronics of high sensitivity. On the other hand, low gas gain has enormous practical advantages for the chamber operation: difficulties due to external high-voltage discharges and internal spark breakdown are reduced. In the early years of chamber construction, the trend was somewhat inverted: one tried to push the gas gain as high as possible, sometimes with "magic" gas mixtures (Bouclier 1970), in order to keep the electronics cost and complexity down. Part of the early problems with chamber systems was no doubt

due to this mode of operation: frequent wire breaking by accidental sparks and the creation of self-sustained discharges on critical spots on the wire surface or due to dust and deposits.

Closely connected to this is the problem of chamber lifetime under irradiation. The positive ions, often complex molecules, tend to break up upon arrival at the cathode surface and may, depending on their composition and chemistry, create detrimental deposits leading to continuous discharges and the subsequent "death" of the chamber (Charpak 1972). The addition of special agents like methylal, or the use of non-polymerizing (CO_2) or polymerization-resistive gases such as ethane (Atač 1977, Daum 1978) can alleviate the problem. Chemical decomposition is a further, strong reason to keep the gas amplification as low as possible.

Another limit encountered by wire systems is imposed by particle rates: in much the same way as the gas gain saturates with space charge created by the avalanches in the chamber gap, the chamber efficiency decreases if the rate of incident particles becomes too high (Sadoulet 1973, Breskin 1975). This seriously limits the application of wire chambers in high-rate experiments, and some of the latest developments in the field have been aimed at removing this limitation.

Charpak and collaborators have developed a new multistep proportional chamber (Charpak 1979a). The idea is to keep the gas amplification extremely low in the "active" chamber volume and to finally admit, for high-gain amplification, only the small fraction of events that are interesting for the specific experiment and are selected by an external trigger. The selection is achieved by transporting the preamplified ionization through a wire grid that is pulsed by the trigger and acts as a gate. In order to achieve this, a new method of avalanche propagation involving photons is employed. The rate capability of the device is several orders of magnitude above that of conventional chambers.

At the same time, one can also dispense with the very thin sense wires normally used for one-step amplification. This new development is, like many other ideas from Charpak's group at CERN, a beautiful example of the fact that the evolution of proportional chambers has by no means come to an end yet.

2.4.4 Streamer chambers

If the avalanche formation in gases is pushed beyond the proportional regime, up to gas amplifications above 10^8, it can grow into the so-called streamer mode and become visible by light emission. Streamer propagation starts when the space charge inside the avalanche is strong enough to effectively shield the external electric field. Recombination and corresponding photon emission can set in. The resulting secondary ionization can develop new avalanches in the strong field regions in front of and behind the initial avalanche (Rice-Evans 1974). The process will propagate until complete breakdown occurs between the electrodes. If, however, only a short high-voltage pulse (typically 10-50 kV/cm during 5-20 ns) is applied across a flat electrode structure (figure 10), the streamer development can be "frozen" at a length of a few millimetres. Direct track images can then be obtained by optical recording, in most cases through the (transparent) electrodes. The resulting streamer chamber (Chikovani 1964, Dolgoshein 1964) is a very attractive detector that combines excellent multiparticle efficiency and multitrack resolution with space resolution and vertex reconstruction capabilities similar to those of the bubble chamber. In addition, the device is triggerable and comparably fast: the recording rate is essentially limited by the film transport time.

Since the streamer formation starts from the centres of primary ionization along the track, the measurement of streamer density can be used for mass identification, including the region of relativistic rise (Davidenko 1969, Eckardt 1977).

One of the limitations of the technique is given by the large voltage amplitudes required. Consequently, considerable technological effort has gone into the development of high-voltage pulse systems (Rice-Evans 1974). Pulses of 650 kV with 1 ns rise-time and 3 ns duration have been obtained (Rohrbach 1977).

Another limit is connected to the sensitivity of the photographic recording. In normal streamer mode, neighbouring avalanches tend to merge into flares, especially in regions of high ionization around knock-on electrons or for tracks running almost parallel to the electric field. The use of image intensifiers

(Gygi 1966, Rohrbach 1977) allows a decisive reduction of streamer size resulting in improved space resolution and particle identification ("avalanche" chambers).

Today, streamer chambers are typically used as vertex detectors. Figure 11 shows the recording of a high-energy interaction from a CERN experiment (NA5, see § 4). It demonstrates the excellent quality of multitrack recording and resolution that can be obtained.

2.4.5 Spark chambers and flash tubes

In the spark chamber, a high-voltage pulse of the order of 10 kV/cm is applied for a time exceeding the early stages of streamer formation discussed in § 2.4.4. Complete breakdown by spark formation will result if an ionizing particle has traversed the device. The spark chamber can be viewed as the ultimate step in the hierarchy of increasing gas amplification: roughly 10 orders of magnitude in gas gain separate it from the no-gain ionization chamber. Corresponding to the large amount of energy released, the detection process itself becomes visible and audible -- spark chamber operation has rightly been praised as a spectacular happening (Rice-Evans 1974).

First used in the mid-1950's (Bella 1953), the spark chamber came into universal use in high-energy physics experiments during the decade 1960-1970 (Allkofer 1969). With the introduction of the multiwire proportional chamber, however, its importance diminished fairly quickly, and by now it has almost completely vanished from the detector scene: a good example of the rapid evolution of detector technology during the past 20 years.

During its short career, a large variety of construction techniques, modes of operation, and read-out methods have been invented [see, for example, the review by Charpak (1970a) and the excellent textbook by Rice-Evans (1974)]. There are, however, a number of shortcomings, most notably connected with multiparticle inefficiency, low time-resolution and repetition rate, operation difficulties in magnetic fields, and the necessity for outside triggering. Most of these problems can be solved by the proportional chamber, which does not have these drawbacks.

A good example for simple and low-cost detector construction is the flash-tube chamber introduced by Conversi (1955). A large number of independent, noble-gas-filled tubes or plastic channels are placed between two planar electrodes. Upon traversal by ionizing radiation, a short high-voltage pulse leads to streamer formation and propagation along the tubes struck by the particle, which then emit an intense light-flash. The signal can be recorded visually (film or vidicon tube) or electronically by probes protruding a short distance into the gas volume. Large arrays of flash-tube detectors have been used, mainly in cosmic-ray work (Conversi 1973). More recently, the introduction of flash chambers made of extruded plastic (Conversi 1977) has revived interest in this extremely simple and cheap detector, especially for calorimeter applications (see § 3).

2.4.6 Summary on track detectors

In table 1 we summarize the different detection methods for charged particles and compare quantities that are relevant for particle physics experimentation. Performance figures for typical applications are provided as a guide; rather large deviations are possible for special applications.

This is evidently true for the *spatial resolution* achieved with the different methods: the average figures are surprisingly close to each other, in the region of a few hundred microns. In contrast, optimal performance shown in the next column exhibits considerable differences. It has in general been reached only in special-purpose, small-size detectors, an illustration of the difficulty of maintaining a high standard of excellence in large-scale detector systems.

The *occupation time* of a detector limits the maximum input event rate: any additional event within this interval will not be recorded as a distinct new event. However, this need not constitute a major limitation. It is often possible, by using the time information, to disentangle the different events in off-line reconstruction (see § 4). The drift chambers may therefore be superior to proportional chambers in *instantaneous rate* capability, and even the bubble chambers, with their very long "memories", can handle event rates of up to 10^4 Hz.

Table 1

Operating characteristics of track detectors

	Detector	Space resolution		Occupation time (ns)	Maximum instant. rate per element (Hz)	Recovery time (ns)	Read-out
		Practical (μm)	Optimal (μm)				
Continuously sensitive devices	Scintillator	300	300	1-10	10^7	Rate limit 10^4 Hz per mm anode wire	Photomultiplier
	Prop. chamber	600	100	100	10^6		Pulse electronics
	Drift chamber	150	50	100 to $\sim$ 1000	10^7		Pulse electronics (time measuring)
Pulsed devices	Spark chamber	300	100	10^3	10^5	10^6	Film or electronics
	Streamer chamber	200	20	10^3	10^5	10^6	Film
	Bubble chamber	250	50	10^6	10^4	10^7	Film

The *recovery time*, on the other hand, really limits the data-taking speed: all pulsed detectors are inferior in this respect, since it takes time to sweep away the spark or streamer discharges and reload the pulsing system, or to restore the pre-expansion thermodynamics in the case of the bubble chamber. In contrast, the d.c. operated devices show recovery effects only on a microscopic scale, e.g. of the order of the avalanche size in proportional chambers. This leads to a limitation in radiation density rather than in total rate.

Finally, the *read-out* method plays a decisive role in data-acquisition speed: pulse electronics can operate orders of magnitude faster than film transport systems and is in addition well adapted to the trigger selection schemes that will be discussed in § 4.

2.5 Čerenkov detectors

2.5.1 Characteristics of Čerenkov radiation

Uniformly moving charged particles may lose energy by emitting visible or ultraviolet light. One such effect, "Čerenkov radiation", was observed experimentally by Čerenkov and Vasilov; Tamm and Frank developed a classical theory for this radiation phenomenon; later, Ginzburg provided a quantum mechanical description (Čerenkov 1964). The classical theory is based on the idea that a charged particle moving with velocity $\beta = v/c$ in a medium with refractive index $n(\lambda)$ may emit light along a conical wave front. The angle of emission θ at a given wavelength λ is connected to the particle velocity v by: $\cos\theta(\lambda) = v_{light}(\lambda)/v = 1/\beta \cdot n(\lambda)$. This relation explains the usefulness of this effect for elementary particle physics: a measurement of the emission angle of the light, together with the knowledge of $n(\lambda)$, affords a direct measurement of the particle's velocity. Knowing the momentum of the particle, a measurement of its mass can be obtained with an accuracy

$$\frac{dm}{m} = \frac{1}{1-\beta^2}\frac{d\beta}{\beta} + \frac{dp}{p} .$$

Optical methods have been developed to measure β with a relative accuracy up to $d\beta/\beta \approx 10^{-7}$ (Litt 1973). Within the classical Frank-Tamm theory the average

number of Čerenkov photons dN_γ/dE emitted per unit photon energy interval and for a radiator of length L is given as

$$\frac{dN_\gamma}{dE} = \frac{\alpha L}{\hbar c} \sin^2 \theta \ .$$

Integrating over the energy acceptance of the photon detector (E_1 to E_2), and taking $\varepsilon_{det}(E)$ as the efficiency for detecting photons emitted with energy E, gives the average number of detected photons N:

$$N = N_0 \ L \sin^2 \theta \ ,$$

with

$$N_0 = \frac{\alpha}{\hbar c} \int_{E_1}^{E_2} \varepsilon_{det}(E) \ dE \quad \simeq 370 \int_{E_1}^{E_2} \varepsilon_{det}(E) \ dE \quad (eV \cdot cm^{-1}).$$

Typical values for N_0 are around 50, ranging up to 100 to 200 if the ultraviolet photons can be detected efficiently. This form of energy has to be compared with the energy loss by ionization and excitation: typically one finds for the ratio,

$$R = \frac{(dE/dx)_{\check{C}erenkov}}{(dE/dx)_{ioniz.,exc.}} \approx 10^{-2} \text{ to } 10^{-3} \ ,$$

for gaseous, liquid, and solid media. Minimization of photon emission from excitation processes is therefore mandatory for useful Čerenkov detection.

2.5.2 Features of Čerenkov detectors

Čerenkov radiators, suitable for elementary particle physics, have refractive indices $n(\lambda)$ in the range $n > 1$ up to ~ 2, as illustrated in figure 12. It shows the variation of the Čerenkov angle θ as a function of the particle velocity and the refractive index of the material. Table 2 gives a summary of the identification properties of various substances. Note, in particular, that the range $n = 1.02$ to 1.1 corresponds to particle momenta characterized as "minimum ionizing" (see § 2.2); in this velocity range no other method of particle identification, such as multiple ionization measurements, has been proved practical. The recent

Table 2

Identification properties of selected Čerenkov radiators

Radiator	α $(= n - 1)^*$	Threshold value (γ_{th})	Comment
Scintillator	5.8×10^{-1}	1.30	
LiF	4.0×10^{-1}	1.43	
Plexiglass	4.0×10^{-1}	1.43	
FC 75	2.8×10^{-1}	1.60	Lowest-index room temperature liquid
Liquid N_2	2.0×10^{-1}	1.81	
Liquid H_2	1.1×10^{-1}	2.40	
Liquid He	2.1×10^{-2}	5.0	
Aerogel	$(2\text{-}10) \times 10^{-2}$	2-5	Transparent solid; index can be tuned during production
C_5H_{12}	1.7×10^{-3}	17	Highest-index STP gas
CO_2	4.3×10^{-4}	34	at STP
He	3.3×10^{-5}	123	

* In visible wavelength region.

development of the Aerogel-type radiator (Cantin 1974, Benot 1978) appears to be the first practical possibility for constructing relatively large solid-angle identifiers in a momentum range of particular interest for physics at the existing pp and e^+e^- colliders. Gaseous radiators have found the widest applications, as the refractive index can be altered by changing the gas pressure P with approximately

$$(n - 1) = (n_0 - 1)P \ ,$$

where n_0 is the refractive index at atmospheric pressure.

Threshold Čerenkov counters (TCC) detect particles that have a velocity sufficient to produce Čerenkov light in the radiator. At threshold the emission angle $\theta = 0$ corresponds to the threshold velocity $\beta_0 = 1/n$; at saturation, $\beta = 1$, the emission angle is $\cos \theta_L = 1/n$. The rapid change of emission angle above threshold results in a strongly varying light yield ($\langle N_\gamma \rangle \sim \sin^2 \theta$) for particles above threshold momentum, and hence a strongly varying detection efficiency $\varepsilon = 1 - \exp(-N_\gamma)$. This indicates another reason for careful optimization of the optics and photon detection to minimize the momentum range with low efficiency. Frequently, identification of π's, K's, and p's is required over a range of momenta p for which a succession of threshold counters is necessary, each one optimized for a different average Čerenkov angle $\langle\theta\rangle$; for relativistic particles these design parameters are approximately determined as

$$\langle\theta\rangle = \left(\frac{N}{N_0 L}\right)^{1/2} \lesssim \left[(m_1^2 - m_0^2)^{1/2}\right]/p \ ,$$

$$L \gtrsim \left(\frac{N}{N_0}\right)\left[p^2/(m_1^2 - m_0^2)\right] \ ,$$

where the lighter (m_0) particle is detected at $\langle\theta\rangle$ and the heavier (m_1) particle is below threshold.

As an illustration of present-day applications, a photograph of a particle identifier constructed for an experiment at the CERN Intersecting Storage Rings (ISR) is shown in figure 13, which uses three different threshold counters to provide a mass measurement in the momentum range from 3 to 20 GeV/c.

The advent of high-energy secondary beams (p = 20 to 400 GeV/c) has prompted the developments of *ring-imaging Čerenkov counters*. The light cone is focused into a ring with lenses or spherical mirrors; the diameter of this ring is related to the Čerenkov angle and thus to the particle velocity.

The achievable velocity resolution depends on a number of factors, such as energy loss and multiple scattering of the particles in the counter, required phase-space acceptance of the particles, and degree of corrections of the optical system. "Differential" gas counters have been developed to provide particle identification in the 100 GeV/c range, requiring a velocity resolution $\Delta\beta/\beta \sim 10^{-5}$. For this momentum range, chromatic dispersion in the radiator is found to be the most important limitation to the velocity resolution. As a consequence, optical systems have been developed which reduce this dispersion error substantially. These achromatic counters ("DISC") achieve resolutions $\Delta\beta/\beta \approx 10^{-6}$-$10^{-7}$. The performance of these three groups of counters are summarized graphically in figure 14 (Benot 1973).

The effect of improved photon detection on the performance of imaging Čerenkov counters has been repeatedly stressed. Large arrays of photomultipliers (Benot 1979) or MWPCs, sensitive to ultraviolet radiation (Séguinot 1977), have been considered for the measurement of the imaged Čerenkov ring. These techniques are being actively pursued, as they promise high-resolution velocity measurements over a range of momenta combined with a large phase-space acceptance. A conceptual design of a ring-imaging Čerenkov counter for a particle collider facility is shown in figure 15. A radial succession of two or three such detectors would allow identification of secondary particles in a range from $\sim$ 1 GeV/c to $\sim$ 100 GeV/c (Séguinot 1977).

2.6 Transition radiation detectors

2.6.1 Characteristic features of transition radiation

Transition radiation (TR) is produced whenever charged particles traverse the interface between substances of different dielectric properties. Like Čerenkov radiation, it is emitted by particles in uniform and rectilinear motion and is also rather intimately connected with the optical properties of the material traversed.

The effect of TR was predicted theoretically by Ginzburg and Frank (Ginzburg 1946, Čerenkov 1964). Already in the original work, which concerned the properties of TR in the optical region only, a unique feature of this radiation was appreciated: the intensity of the emitted light is a function of the particle's energy $E = m_0\gamma$, $\gamma = (1 - \beta^2)^{-1/2}$; hence a measurement of this radiation should offer the possibility of identifying ultrarelativistic particles in an energy regime where other effects (e.g. Čerenkov radiation), which are sensitive to the particle velocity, can no longer provide useful particle discrimination.

While this energy dependence was always intriguing to experimental physicists (Alikhanian 1973), it was Garibian (1973) who showed that the TR phenomenon must also occur in the X-ray region (XTR) and thereby laid the foundation for the practical use of this effect in particle physics.

Simplified derivations have been given for the ultrarelativistic limit, $\gamma >> 1$, $\omega_{TR} >> \omega_{plasma}$, which is the most interesting case for practical applications (Durand 1975, Jackson 1977). The particle traversing the medium with a macroscopically varying dielectric constant $\varepsilon(\omega)$ produces a time-dependent electric field, resulting in a transient polarization of the medium. The induced polarization current is at the origin of TR emission. For a radiator geometry as shown in figure 16, one finds approximately for the radiated energy per unit solid angle $d\Omega$, unit frequency ω, and per foil:

$$\frac{d^2E}{\hbar d\omega d\Omega} = \frac{\alpha}{\pi^2}\left|\frac{\theta}{\gamma^{-2} + \theta^2 + \zeta_1^2} - \frac{\theta}{\gamma^{-2} + \theta^2 + \zeta_2^2}\right|^2 4\sin^2\frac{\phi_1}{2},$$

where α denotes the fine-structure constant and $\zeta_i = \omega_{plasma,i}/\omega$, the reduced plasma frequency in the medium i. The angle $\phi_1 = (d_1\omega/2c)(\gamma^{-2} + \theta^2 + \zeta_1^2)$ gives the phase difference between the radiation emitted from the two interfaces.

The above expression exhibits the characteristic features of XTR:

i) The <u>angular distribution</u> is forward peaked and has a sharp maximum for $\theta \sim 1/\gamma$. Such a distribution is typical for radiation from ultrarelativistic particles and is also found for bremsstrahlung and synchrotron radiation.

ii) The total energy radiated is found to be ($\omega_{plasma,1} >> \omega_{plasma,2}$)

$$E = \frac{2}{3}\alpha(\hbar\omega_{plasma,1})\gamma \ ;$$

it is proportional to γ with an average number of radiated photons $\langle N\rangle$ of order α:

$$\langle N\rangle \sim \alpha \frac{\gamma\cdot\hbar\omega_{plasma,1}}{\hbar\langle\omega\rangle} \sim \alpha \ .$$

iii) Formation zone: the formula for emission from a foil predicts maxima of emission for $\phi_1 = n\pi$. Sometimes, the quantity $Z_1 = (2c/\omega)(\gamma^{-2} + \theta^2 + \zeta_1^2)^{-1}$ is called the "formation zone", and corresponds physically to the minimum distance the particle has to penetrate into the new medium before the electromagnetic field reaches its corresponding equilibrium value. It demonstrates that TR is a macroscopic effect with an intensity tending towards zero with decreasing foil thickness $d_1 << \pi Z_1$. Similar macroscopic relaxation effects have been observed for the relativistic rise of the ionization, which eventually saturates owing to macroscopic polarization effects (§ 1). If, however, particles traverse foils that are thinner than the formation zone, such polarization effects and consequently the "density effect" are reduced (Alikhanian 1963).

iv) Emission from a periodic stack of N foils ("radiator"). The derivation of XTR can be generalized for a periodic arrangement of N foils (thickness d_1) spaced d_2 apart:

$$\frac{d^2E}{\hbar d\omega d\Omega} = \frac{\alpha}{\pi^2}\left|\frac{\theta}{\gamma^{-2} + \theta^2 + \zeta_1^2} - \frac{\theta}{\gamma^{-2} + \theta^2 + \zeta_2^2}\right|^2 \cdot 4\sin\frac{\phi_1}{2}\cdot F_N(\phi_1 + \phi_2) \ ,$$

where

$$F_N(\phi) = \frac{\left[1 + \exp(-N\sigma) - 2\exp(-N\sigma/2)\cos N\phi\right]}{\left[1 + \exp(-\sigma) - 2\exp(-\sigma/2)\cos\phi\right]} \ ,$$

and $\sigma = \mu_1 d_1 + \mu_2 d_2$. This formula describes the radiation yield at the end of the radiator, including absorption of XTR in the material (mass absorption coefficients μ_1 and μ_2). There are two new features introduced by the possibility of multiple-foil interference (Artru 1975, Fabjan 1975a). The emitted radiation will show very sharp angular maxima for $\phi = 2\pi n$, where $F_N(\phi = 2\pi n) \approx 4/\sigma^2$, and

with width $\Delta\theta \sim \sigma^{1/2}/\gamma$. Secondly, the multiple-foil interference influences the γ response of a radiator, giving rise to saturation in the emitted radiation determined by the formation zone Z_2. In addition, constructive, multiple-foil interference sharpens the threshold behaviour of the emitted radiation as a function of γ. The role of TR detectors in particle physics is therefore rather similar to that of threshold Čerenkov detectors.

2.6.2 Optimization and performance of TR detectors

Useful detector performance may only be achieved by careful optimization of all parameters of both the radiator and the X-ray detector (Fischer 1974, Cobb 1977b). Such optimization procedures are best understood qualitatively by using a dimensionless analysis introduced by Artru et al. (1975). They noted that any transition radiator can be described in terms of a universal function of certain dimensionless parameters, independent of the material and the spectral range used. These parameters are:

a dimensionless particle energy $\Gamma = \gamma/\gamma_1$, where $\gamma_1 = d_1\omega_{plasma,1}/2$;

a dimensionless frequency $\nu = \omega/\gamma_1\omega_{plasma,1}$

and the ratio $d_2/d_1 = \kappa$.

Inspection of the universal curves (figure 17) shows that

i) very little radiation is produced for $\nu > 1$, for any Γ;

ii) there is a strong peak at $\nu = 0.3$ for $\Gamma > \frac{1}{2}$;

iii) there is a strong interference minimum at $\nu = 0.18$, due to a phase slip of π within the foil;

iv) the amount of radiation is small for $\Gamma < \frac{1}{2}$;

v) d_2 can be made such that the phase slip in the gap is 2π and there is constructive interference.

More detailed numerical studies have confirmed that TR detectors designed to have good efficiency near threshold will have $\Gamma = 1$, $\nu = 0.3$, $\kappa \approx 5$. Given a certain material with ω_{plasma}, the foil thickness is then determined by the desired threshold $\gamma = \gamma_1$.

The choice of the material and the design of the X-ray detector depend on the specific detector structure. Most frequently used are arrangements where the TR radiator is followed by a MWPC to measure the XTR yield. The total signal measured is then the sum of the XTR and the ionization loss of the charged particle, and in the optimization the ratio [(ionization + detected XTR)/ionization] has to be maximized. One finds rather generally for this ratio (Cobb 1977b, Willis 1977)

$$\frac{\text{(ionization + XTR-detected)}}{\text{ionization}} \sim \frac{1}{Z^{3.5}} ,$$

where Z is the number of protons of the radiator material. This very strong dependence on Z explains that, for practical detectors, thin lithium foils have been chosen to achieve a useful performance (Cobb 1977b). A typical energy loss spectrum, as measured in a MWPC, is given in figure 18, both for the ionization loss only, and for combined ionization and TR energy loss. In figure 19 the XTR yield from various radiator geometries is shown as a function of particle momentum. It is noteworthy that the TR yield computed for such detector combinations agrees very well with the measured values. The prediction of the TR theory can be reliably used for detailed optimization and performance evaluation of practical instruments (figure 20).

2.6.3 Future TR developments

So far, TR detectors have mostly been used for identification of electrons and ultrarelativistic cosmic-ray pions with γ-values above 2000. Several approaches have been considered (Camps 1975, Fabjan 1977a) for extending the γ-range down to 100, where these detectors would serve as large-acceptance hadron identifiers. This operating range is very difficult as the typical foil thicknesses approach 5 μm, and X-ray photons in the energy range 1-5 keV have to be detected. A novel approach has been suggested (Alikhanian 1978). The angular distribution of the XTR photons becomes sufficiently wide at these low γ-values so that spatial discrimination between XTR photons and the ionization clusters may be possible.

2.7 Summary of particle identification methods

A summary of particle identification methods is provided in table 3. Although the physics of these methods has been known for many decades, only recent developments (mostly on electronics systems) and a growing need in high-energy experimentation have prompted these detector advances. A graphic summary is given in figure 21 (Willis 1978), showing the γ-range that can be covered by each technique as a function of the detector length. The gap between the identification range, conveniently handled by Čerenkov techniques, and the TR range, can be related to the fact that the spectral region between the ultraviolet (Čerenkov) and few keV X-rays (XTR) requires special measurement techniques which have not yet permitted practical detectors (Willis 1978). Multiple ionization measurements are now being developed to bridge the gap; this requires sufficiently accurate measurement of the average ionization, which rises logarithmically as a function of γ. Physically this "inaccessible" frequency range is probed with virtual photons, exciting the deep atomic shells not affected by the macroscopic polarization phenomena.

3. DESTRUCTIVE METHODS

3.1 Principle of detection

A class of detectors measures the energy and position of particles through total absorption in these devices. In the process of absorption, secondary particles are generated, which themselves react inside the detector; eventually, all (or most of) the incident particle's energy will be converted into heat -- hence the name "calorimeter" for this kind of detector. The increase in temperature, however, is usually too small to be measurable practically, and some characteristic interaction with matter (e.g. atomic excitation or ionization) is used to derive a detectable signal. There are several reasons why these devices are attractive for high-energy physics: i) it is the only way to measure neutral particles among the secondaries produced in high-energy collisions; ii) absorption of the particles is a statistical process: the accuracy of the energy measurement improves with increasing particle energy E as $E^{-1/2}$; therefore with

Table 3

Particle identification; available techniques

Technique	γ range	Comments
Aerogel	$\gamma_t \gtrsim 2$	With $\gamma \approx 6$ can resolve π/K ambiguity at cross-over of ionization.
Multiple ionization measurement in homogeneous medium	$\gamma < 6$	Owing to $dE/dx \sim 1/\beta^2$ for $\gamma \lesssim 6$, powerful discrimination obtainable with modest resolution in the dE/dx measurement.
Time-of-flight	$\gamma \lesssim 6$	$\sigma \sim 300$ ps has been achieved with large scintillator systems. $\sigma \leq 100$ ps has been obtained with special spark chambers.
Gas threshold Čerenkov	$\gamma_t > 10$	Not suitable for storage ring (SR) applications where 4π coverage is required.
Multiple ionization measurement on relativistic rise in homogeneous medium	$2 \lesssim \gamma \lesssim 50$	Requires $\sigma(dE/dx) \sim 2$-3%; achieved so far in planar geometries only, but not in SR geometries.
Imaging Čerenkovs	$2 < \gamma \lesssim 200$	Č-photons detected with UV-sensitized proportional chamber structures (PIC); or special optical systems, with severely limited phase-space acceptance for particles.
Transition radiation	$\gamma \gtrsim 1000$	Useful as compact threshold detector for specialized applications.

the increasing energy of accelerators, absorptive spectroscopy is becoming frequently more accurate than magnetic methods; iii) the signal from these detectors related to the energy of the incident particle is formed on a time scale of 10^{-8} to 10^{-7} s and is therefore useful for very fast decisions ("triggering") to select events which have as signature a characteristic distribution of energy deposit.

It is useful to group calorimeters according to the type of particle to be detected. Electrons and photons interact electromagnetically with the absorbing material; dominant are bremsstrahlung, pair production, and Compton scattering reactions. The magnitude of these cross-sections will determine the features of "electromagnetic calorimeters", such as size and depth. Hadrons will mostly interact strongly and hence the nuclear interaction length is the appropriate scale. The largest calorimeters have been built to study neutrino interactions, which interact only weakly with the absorber. Secondaries in such reactions are mostly hadrons, and the instrumental features of such detectors are those of hadronic calorimeters.

In recent years much was learnt about the properties of electromagnetic and hadronic showers, as will be discussed in the following section. Considerable effort was also devoted to instrumental work in order to develop large and complex devices capable of measuring the particle energy with the intrinsic calorimeter resolution. Extensive discussions are found elsewhere (Murzin 1967, Rossi 1964, Atač (ed.) 1975, Iwata 1979).

In recent years very powerful Monte Carlo shower simulation programs have been developed, for both electromagnetic cascades (Ford 1978) and hadronic showers (Gabriel 1977). These very refined programs allow detailed performance simulations of complex calorimeter devices.

3.2 Electromagnetic shower detectors

3.2.1 Showering process

The cross-sections for bremsstrahlung and electron pair production, which are the dominant interaction processes for high-energy electrons and photons, become nearly energy-independent above 1 GeV. They are usually expressed in units

of "radiation length" X_0, which is defined as the mean path-length for an electron in a material (A,Z) and is found to be, in a Born approximation calculation,

$$X_0 \left[g/cm^2\right] \approx 716\ A/Z^2\ \ln\ (183\ Z^{-1/3})\ .$$

It decreases with the atomic number of the absorber as $X_0 \sim 1/Z$. The secondaries produced in the electromagnetic interaction of a photon or electron are again electrons or an electron and a photon. The cascade develops through repeated similar interactions, producing an increasing number of secondary photons and electrons. Eventually, the shower maximum with the largest number of secondaries will have developed when their average energy becomes low enough to stop further multiplication. From there on, the shower decays slowly through ionization of the electrons or Compton scattering of the photons. This change in the relative strength of interaction processes is characterized by the "critical energy ε" in the material: ε is that electron energy for which energy losses by radiation equal the collision and ionization losses. In this simplified discussion we have ignored nuclear interactions (photonuclear effects), which play a negligible role. It is this dominance of the electromagnetic processes which distinguish the electromagnetic showers from hadronic ones.

Experimental results on shower distributions can be parametrized in the following way:

i) The position of the shower maximum t_{max} induced by particles with energy E is approximately

$$t_{max} \left[\text{in units of } X_0\right] = \ln E/\varepsilon - 1.0\ .$$

Some representative results are shown in figures 22 and 23.

ii) The total longitudinal depth D, beyond which no increase in detected signal can be measured, is of the form

$$D \left[\text{in units of } X_0\right] = t_{max} + 4\ \lambda_{att}\ ,$$

where λ_{att} defines the exponential decay of the shower beyond the shower maximum.

iii) The transverse shower dimensions are characterized by the r.m.s. spread of electrons of critical energy ε after passing through one radiation length. When expressed in "Moliere" units $R_M = 21\ \text{MeV} \cdot X_0/\varepsilon$, scaling of the radial shower dimensions is found (figure 24). Approximately 90% of the shower energy is contained in a cylinder of radius $r \approx 1\ R_M$.

3.2.2 Performance of electromagnetic shower detectors

Homogeneous shower counters combine in one substance the functions of "passive" particle absorption and "active" signal read-out; for example, a correctly sized block of scintillator may serve as such a detector. In practice, preference is given to materials with a small radiation length. In table 4 the properties of the two most frequently used homogeneous shower counters are summarized.

In *heterogeneous counters* the functions of particle absorption and active signal read-out are separated. This allows the optimal choice of absorber materials and a certain freedom in the signal treatment. Traditionally, such devices are built as sandwich counters, with alternately one sheet of absorber, e.g. lead, followed by an "active" material, such as a plane of scintillator. In such devices only that fraction of the shower energy absorbed in the active material is measured, whence the name "sampling calorimeter". Fluctuations in the energy deposit in the active medium is the sole limit to the energy resolution of such devices (Fabjan 1977b). In practical constructions, the ratio of energy loss in the passive and the active material is rather large, typically of the order of 10. Then the "sampling fluctuations" are essentially due to the statistical variation of the electron path length in the active material. One finds for the percent energy resolution ["Rossi's approximation B" (Rossi 1964)], $\sigma/E \approx \sqrt{2/n_e}$, where $n_e/2$ is the number of samplings for the electron pairs in the absorber; $n_e \approx (E_{incident}/\Delta E_{gap})$, ΔE_{gap} being the energy loss per sampling gap. In figure 25 a comparison of some representative measurements is made with this approximation, which in convenient units is written as

$$\frac{\sigma}{E} \approx 0.05 \sqrt{\Delta E_{gap}\ (\text{MeV})} \Big/ \sqrt{E_{incident}\ (\text{GeV})}\ .$$

Table 4

Properties of two homogeneous electromagnetic shower detectors

Physical properties	Lead glass (55% PbO, 45% SiO_2)	NaI(Tl)
X_0 (cm)	2.36	2.60
ρ (g/cm^3)	4.08	3.67
Refractive index	1.67	1.78
ε (MeV)	15.8	12.5
Detection mechanism	Čerenkov emission from electron pairs;	Scintillation light; about five times more light compared to plastic scintillator.
Limitation to energy resolution	For $E_{particle} \gtrsim 2$ GeV: photostatistics. For $E_{particle} \lesssim 2$ GeV: instrumental effects.	Non-uniformities in production and collection of the scintillator light.
$\frac{\sigma(E)}{E}$ (typically)	$\gtrsim \frac{5\%}{\sqrt{E\ (GeV)}}$	$\gtrsim 1.5\%/E^{1/4}$ (GeV)

From measurements it is found that this approximation is valid for $E_{gap} \gtrsim 1$ MeV and $0.05 \lesssim \kappa \lesssim 0.4$, where κ is defined as $\kappa = \Delta E_{active}/\Delta E_{passive}$. For detectors with $\kappa < 0.05$, multiple scattering effects of electrons crossing the interface between the different materials contribute to additional fluctuations, resulting in worse energy resolution. In practice, it is also not possible to improve the energy resolution beyond certain limits by simply increasing the sampling ratio κ. Owing to the usually rather different active and passive materials, characterized by very different ε, abrupt changes in the shower composition produced at each interface are thought to be at the origin of the levelling of the energy resolution, for which values as low as $\sigma = 0.03/\sqrt{E}$ have been achieved.

The position of showers can be measured with a suitable read-out geometry (see § 3.4.1) and with an accuracy which depends on the transverse size of the showers: in practice, a spatial localization of $\sigma_{spatial} \approx 0.3\ X_0$ can be readily obtained (Cobb 1979).

3.3 Hadronic shower detectors

3.3.1 Hadronic showers

The hadronic shower is far more complex than the electromagnetic processes. It is propagated by a succession of inelastic hadronic interactions, which, at high energies, are characterized by multiparticle production and in addition by particle emission originating from nuclear disintegration of excited nuclei. Today we know that these complex nuclear processes determine the energy resolution achievable with such hadron calorimeters. The hadronic multiplication process determines the longitudinal and transverse shower distributions, measured on the scale of nuclear absorption length $\lambda_0 = A/N_A\ \rho\ \sigma_i$ (cm); A is the atomic mass number of the material, N_A Avogadro's number, ρ the density, and σ_i the inelastic cross-section. Above the resonance region, λ_0 is essentially energy-independent (table 5). In figures 26 and 27 some experimental results on longitudinal and transverse distributions are shown. Approximately 95% of the energy of the shower is contained in a cylinder with radius $r \approx 1\ \lambda_0$.

Table 5

Parameters of materials used for calorimeters

Material	Z	A	ρ a) (g/cm^2)	dE/dx a) (MeV/cm)	λ_0 (cm)		X_0 a) (cm)	ε (MeV)	e.m. λ_{att} c) (X_0)
					N a)	π b)			
C	6	12.0	≈ 1.55	≈ 2.76	49.9	64.9	≈ 27.5	75.9	
Al	13	27.0	2.70	4.37	37.2	45.8	8.9	39.3	2.7
Liquid A	18	40.0	1.40	2.11	80.9	97.7	14.0	29.8	
Fe	26	55.9	7.87	11.6	17.1	18.9	1.76	20.5	
Cu	29	63.5	8.96	12.9	14.8	17.2	1.43	18.7	3.0
Sn	50	118.7	7.31	9.4	22.8	24.7	1.21	11.4	3.5
W	74	183.9	19.3	22.6	10.3	10.5	0.35	7.9	4.1
Pb	82	207.2	11.35	12.8	18.5	18.4	0.56	7.2	3.9
U	92	238.0	18.95	20.7	12.0	11.4	0.32	6.6	
NaI			3.67	4.84	41.3		2.59	12.5	
Plastic scintillator			1.032	2.03	68.5		42.9	87.1	
Lucite			≃ 1.2	2.32	65.0		34.5	80.0	

Note: λ_0 = nuclear absorption length, X_0 = radiation length, ε = critical energy.

a) From Particle Data Group (1978).

b) Pion inelastic cross-section $\sigma_i = 31.2\ A^{0.744}$ (mb) was used.

c) Values correspond to 6 GeV electron showers.

3.3.2 Performance of hadron calorimeters

Recent experimental work has elucidated the physics mechanisms, which affect the energy resolution of hadronic calorimeters (Fabjan 1975b, Fabjan 1977b). Because of the nature of the hadronic interaction, a considerable fraction of the incident particle's energy is spent in reactions which do not result in an observable signal within the detector. Such processes may be energy leakage of various forms, e.g. back-scattering (albedo), or leakage of muons, neutrinos, and slow neutrons. Nuclear excitation, break-up, and "nucleon evaporation" is, however, the most important source of energy loss or "invisible energy". Experimentally, this is most clearly demonstrated by comparing the signal of electrons, where such nuclear effects are absent, with hadrons of the same energy. Typically, this ratio $S_{h/e}$ = hadrons/electrons is *on the average* about 0.7 in the energy range 1-20 GeV (figure 28). However, owing to fluctuations, the nuclear cascade may develop with a dominant electromagnetic (π^0) component and hence produce signals up to the level of electrons. The energy resolution measured is shown in figure 29 and can be parametrized for non-uranium absorbers as

$$\frac{\sigma}{E} \approx 0.50 \frac{1}{\sqrt{E\ (\mathrm{GeV})}} .$$

Note that the larger size required for hadron calorimeters makes it mandatory to choose sampling calorimeters for practical applications. Measurements (Fabjan 1977b) on hadronic sampling fluctuations can be parametrized as

$$\frac{\sigma^{\mathrm{hadrons}}_{\mathrm{sampling}}}{E_{\mathrm{incident}}} \approx 0.1 \sqrt{E_{\mathrm{gap}}\ (\mathrm{MeV})} \Big/ \sqrt{E_{\mathrm{incident}}\ (\mathrm{GeV})} ,$$

approximately twice as large as for electromagnetic showers. However, in contrast to electromagnetic detectors, hadronic sampling can be made smaller than the measured hadronic energy resolution: it can be concluded that the fluctuations in the visible energy deposit are solely responsible for the intrinsic hadron energy resolution.

Several possible ways of correcting for these nuclear fluctuations have been considered, with the aim of improving the energy measurement.

One method, which has been tested successfully, is based on fission compensation in ^{238}U. This material has a very high fission cross-section for relatively energetic neutrons (1-10 MeV), the typical energy spectrum of neutrons produced in the nuclear break-up. Estimates show that approximately the fraction of the energy spent in such break-up processes is recaptured through the neutron-induced fission and made observable in the calorimeter, mostly in the form of energetic fission photons. The results shown in figure 28 indicate that such fission compensation is indeed achieved on the average ($S_{h/e}^{uranium} \approx 1.0$). Measurements on the energy resolution (figure 29) show an improvement of approximately 2, and demonstrate that this compensation mechanism also works event-by-event (Fabjan 1975b, Fabjan 1977b). Table 6 summarizes measurements on energy resolution for various hadronic calorimeter configurations.

3.4 Calorimeter instrumentation

The need for large calorimeter facilities, particularly at storage rings, has prompted considerable technical development. In figure 30 the principal methods are schematically shown; characteristic features are summarized in table 7.

Recent revival of optical methods based on light collection in wavelength shifters (WLS) (Garwin 1960, Atwood 1976) is the basis for the construction of several hadron calorimeters with almost 4π coverage. The principle of this method is indicated in figure 30b: photons with a relatively short wavelength λ_1 are produced in the scintillator and guided by internal reflection to one edge; a fraction of the photons are then absorbed in the WLS and re-emitted with $\lambda_2 > \lambda_1$, and finally registered by a photomultiplier. As an example of the possibilities offered by this technique, the layout of a calorimeter facility, at present under construction at CERN for an ISR experiment, is shown in figure 31 (see also figure 36). In this design, adequate transverse and longitudinal subdivision has been achieved without introducing more than $\sim$ 5% inactive volume.

A class of read-out methods is based on charge collection in an appropriately chosen medium (liquid or gas). Large-scale detectors operating in the ion chamber mode have been using liquid argon exclusively (Willis 1974, Cobb 1979). This

Table 6

Hadronic energy resolution in sampling calorimeters

Calorimeter type; numbers in brackets give cell thickness in mm	Energy range (GeV)	Sampling fluctuations (%)	Global energy resolution (measured)	Intrinsic energy resolution (computed)	Reference
Fe (1.5) - LA (2)	1-10	$15/\sqrt{E}$ (*)	$47/\sqrt{E}$	$45/\sqrt{E}$	Fabjan (1977b)
U (1.7) - LA (2)	4-10	$20/\sqrt{E}$ (*)	$30/\sqrt{E}$	$20/\sqrt{E}$	Fabjan (1977b)
Fe (50) - Scint (6)	15-140	$\sim 77/\sqrt{E}$	$82/\sqrt{E}$	Dominated by sampling fluctuations	Holder (1978)
Marble (80) - Scint (30)	15-140	$\sim 55/\sqrt{E}$ formula appears to overestimate for light materials	$\sim 45/\sqrt{E}$	Not applicable	Udo (1980)
Fe (27) - Proportional tubes	1-15	$56/\sqrt{E}$	$75/\sqrt{E}$	$50/\sqrt{E}$	Anderson (1978)

The starred (*) values represent measurements; the other values have been computed with the formula given in the text.

Table 7

Characteristic features of common calorimeter read-out techniques

Type	Advantages	Disadvantages	Calibration	Systematic effects	Comments
1. Photon collecting					
a) Scintillator + light-guide	Not suitable for large-acceptance storage ring detectors.				
b) Scintillator + wavelength shifter	Fast (∿ 50 ns pulses). Relatively small insensitive area due to read-out. Relatively simple mechanical assembly.	Limited granularity. Non-uniformities in light collection at ∿ 10% level. Ageing effects of scintillator; photomultiplier read-out sensitive to magnetic field.	Short-term and uniformity: optical methods: Am-loaded NaI light-source and glass-fibre fan-out; integrated radioactive sources. Long-term and energy: *in situ* calibration in conjunction with magnetic spectrometer (?). Mass determination of known resonances.	Non-uniformity in scintillator response. Total-thickness variations of scintillator. Non-uniform ageing of scintillator. Calibration non-uniformities.	Progress on optimized scintillator/WLS combinations likely. Development of avalanche photodiodes would facilitate operation in magnetic fields.
c) Čerenkov light read-out	Proposed for e/h discrimination; for e.m. showers (lead glass); for general storage ring applications: not suitable.				
d) Flash tubes	See "Comments" for (i).				

./.

Table 7 (contd.)

Type	Advantages	Disadvantages	Calibration	Systematic effects	Comments
2. Charge collecting					
- Ionization chamber mode					
e) Liquid argon	Optimum control of systematic effects. Very fine granularity possible. Very high uniformity for signal collection. Preamplifiers can be made insensitive to magnetic field.	Cryogenic techniques; consequently, more complex construction techniques required. Relatively slow.	Short-term and uniformity: easy to < 0.5%, but requires control of LA purity. Long-term and energy: same as (b).	Purity of LA; global mechanical tolerances.	To date, most widely used technique at storage rings. Only proven technique with instrumental effects at the 1% level.
- Proportional chamber mode					
f) MWPC read-out	High granularity	Gain variations; relatively slow.	Non-uniformity in gain requires complete calibration with particles.	Gain uniformity	Reduced energy resolution for e.m. showers; new collection geometries should improve energy resolution.

./.

Table 7 (contd.)

Type	Advantages	Disadvantages	Calibration	Systematic effects	Comments
g) MWPC at high (∿ 10 atm) pressure	Operating characteristics expected to be similar to those of (f)				Parallel electrode geometry at low gas gain may allow simplified construction; energy resolution for e.m. showers in between methods (e) and (f).
h) Proportional tubes	High granularity	Relatively bulky	Gain non-uniformities reduced compared to (f)		
- Geiger mode					
i) Flash tubes	High granularity, simple construction	Dynamic range limited by saturation effects	Long-term: as (b). Short-term: ? (sensitivity of flash tubes appears to depend on many parameters, not all of which can be controlled).	Saturation effects	

technique allows very uniform signal collection even in highly segmented detector volumes, and control of other systematic effects at the 1% level. Similarly, charge collection in gases combined with internal amplification in a proportional chamber geometry permits very high detector segmentation. This technique suggests itself whenever detailed features of the hadronic shower have to be studied. In figure 32 we show the schematic layout of a neutrino detector facility: the absorber plates are made from marble and interleaved with read-out planes built up from square proportional tubes and scintillator. The total mass of this installation exceeds 500 tons.

Calorimeter facilities will play a dominant role in the new generation of colliding beam machines which are at present under construction (for instance, the $p\bar{p}$ collider at CERN and ISABELLE at Brookhaven) or in the planning stage (a 120 GeV × 120 GeV e^+e^- facility, LEP). At these new facilities, particle collisions will produce secondaries depositing hundreds of GeV of energy in these detectors, which could be measured with an over-all accuracy of a few percent. To accomplish this goal, stringent requirements will be imposed on the read-out: control of systematic effects at the 1% level; rather fine segmentation; long-term stability and possibility for calibration. Experience with the existing devices will indicate the possible directions for further technical development.

4. DETECTOR SYSTEMS

In the preceding sections we have seen that -- in the absence of revolutionary new detection principles -- the detector scene is characterized by increasing sophistication in the use of existing methods.

At the same time the simple, single-purpose detector of the past is replaced by complex, multi-purpose detector systems. Information from many different sources has to be channelled, timed, and brought together before the physics analysis can even start.

In this context, systems design and control, signal processing, pattern recognition, and event reconstruction have to be integrated into the concept of an experiment right from the start. Consequently, the experimental physicist has

to work in close collaboration with specialists in electronics systems techniques, and with experts in different domains of computer programming.

In this section we aim to cover the aspects of these diverse systems, and we discuss several large experimental facilities to stress their integration.

4.1 Information processing and transfer

High-energy physics experiments, as a rule, have exploited state-of-the-art electronics techniques, and some recent crucial developments are summarized in table 8. In a few cases, nuclear instrumentation even provided the impetus for electronics developments which found applications outside the narrow speciality. The rapid evolution of electronics and its influence on detector performance is illustrated in table 9, giving some statistics on recent track chamber systems. In less than a decade, detectors together with the matching read-out systems were developed which reduced the unit cell of information from $\sim 10^6$ mm^3 to about 1 mm^3. This improvement in spatial granularity was not accomplished solely through an increase in read-out channels (i.e. number of signal cables), but also through changes in detector operation. The drift chamber geometry, for example, provides convenient serialization of detector information, and the high-frequency response of the read-out gives the corresponding spatial quantization. This increase of signal processing power per read-out channel is a general feature of electronics development. In figure 33 the MWPC read-out electronics are schematically compared with the most recent chamber read-out techniques which are at present prepared for large facilities.

Analog signal processing is being increasingly used for large detector arrays. The most prominent recent example is the development of optimized, low-noise electronics for the liquid-argon ion chamber detectors (Radeka 1974). In such systems the charges are routinely measured at the level of 1 pC with an r.m.s. noise, contributed by the electronics, of equivalently 10^3 to 10^4 electrons. Similarly, low-noise analog electronics are being increasingly used in MWPC and drift-chamber geometries. This allows operation of these chambers at reduced gain, which greatly facilitates chamber operation and increases the chamber

Table 8

Recent landmarks in electronics for particle physics

Item	Approximate year of introduction	Characteristics and comments
NIM electronics (Nuclear Instrumentation Modules)	1967	Signal processing with standardized modular instruments; modularity allows repeated use for different experimental configurations; standardizations permit interchangeability, external serviceability, and international industrial support.
CAMAC	$\sim$ 1970	Extends the NIM concept to computer-oriented modular data acquisition systems; TTL-oriented signal levels; MHz signal transfer; subsequently becomes widely used in industry for process control.
Custom-integrated circuits	1971	First attempts to have MWPC electronics in medium-scale integration. Concept becomes viable for experiments with $\gtrsim 10^5$ identical circuits per customer.
CAMAC-compatible ADCs	1972	Packaging density of ADCs has increased by several hundred during period 1970-1979. Price decreased approximately by same factor.
Low-noise charge-sensitive preamplifiers	1974	State-of-the-art analog instrumentation techniques successfully adapted to high-energy physics; basis for instrumentation of ion- and low-gas-gain proportional chamber.
Programmable preprocessors	$\sim$ 1977	Logic decisions, too complex for conventional logic modular instrumentation, conferred to specially built programmable processor; speed of computation versus ease of programmation controversy.
CAMAC replacement	$\sim$ 1978	Start of discussions: new system ("Fast Bus") oriented towards high-speed data transfer for "fast" processing, based on ECL technology.
CCDs, flash encoders	1978	Charge-coupled devices or flash encoders permit "continuous" (up to 100 MHz sampling rate at present) digitization of detector signals; allows track chamber construction with $\sim$ 1 mm^3 granularity for information read-out.

Table 9

Some statistics on present and future track devices

Detector (year of 1st operation)	Unit cell size (approx.) (mm^3)			Space points	Granularity (mm^3) (2-particle discrim.)			Number of channels	Words/event (track ch.)	Comments
	ΔX	ΔY	ΔZ		ΔX	ΔY	ΔZ			
Split-Field Magnet/ISR (1973)	2	1000	1000	NO	2	1000	1000	$\sim$ 70,000	$\sim 10^3$	Many planes of MWPCs in large dipole magnet.
CCOR Collaboration/ISR (1976)	0.2	5	150	YES	2	10	150	$\sim$ 2,000	$\sim 10^3$	Cylindrical drift chambers in superconducting solenoid.
Mark II/SLAC (1977)	0.2	5	100	NO	2	50	100	$\sim$ 3,000	$\sim 10^3$	Cylindrical drift chambers in warm solenoid.
JADE/PETRA (1979)	0.1	20	20	YES	2	20	20	$\sim$ 4,000	$> 10^3$	Forty-eight drift chamber layers at 4 atm gas pressure.
TPC/PEP ($\sim$ 1980)	0.15	1	5	YES	0.15	3	5	$\sim$ 10,000	$\sim 10^4$	Continuous three-dimensional read-out of track information; operating at 10 atm.

lifetime in a high-rate environment. Low gas gain is also a prerequisite for truly proportional gas gain, so important for applications of ionization measurements.

Standardization of logic signal levels and data processing protocols was important for the industrial support of electronic instrumentation. The NIM Standard permits a modular construction of signal processing systems, which may receive analog signals directly from detectors, such as photomultipliers, and which may subsequently perform rather complex logic decisions based on the primary signal pattern from the detectors.

A further step in experimental complexity was achieved with extensive computer control, monitoring, and data storage. A new standard CAMAC was developed for modular, computer-oriented data acquisition systems. For todays's experiments, the original CAMAC Standard had to be extended to allow data acquisition from up to $\sim 10^5$ signal channels. Besides the advantages of modular instruments, the CAMAC Standard permitted standardization of the required computer software. These basic data acquisition software packages can be shared by all users of the same type of on-line computer, including sometimes rather advanced on-line data analysis programs (histogramming, graphics routines, etc.). The present generation of experiments has reached a size where it is economically no longer mandatory to use standard instrumentation exclusively. It is customary to find a mixture of standard instrument modules interfaced with custom-built special-purpose electronics.

4.2 Data selection and control

Most modern particle physics experiments are highly selective: they look for minute effects, characterized by small interaction cross-sections and buried in a large background coming from "normal" interactions which have to be rejected. The selectivity is imposed by practical limitations in data transmission and analysis. With present-day technology, the rate with which events can be transmitted and stored, say, on magnetic tape or disks, is of the order of 10 to 100 per second. This has to be compared with interaction rates that tend to be limited only by the occupation time of the detectors and are typically of the order of 10^4 to 10^7 per second.

Another factor in favour of selectivity is the problem of off-line analysis: the treatment of data from complex detector systems takes of the order of 0.1 to 10 s/event even on the fastest existing machines. The cost and availability of off-line computer time is therefore a major limitation of the total amount of data that can usefully be recorded in a given experiment.

As a consequence, highly selective on-line data processing has become very important, and the trend is clearly to transmit and store only those data that are relevant for final analysis.

The selection is usually done in a hierarchy of different decision levels with increasing selectivity and complexity. This is imposed by efficiency considerations: since each step occupies a definite time interval and the corresponding dead-time of the detector increases sharply with the complexity of the data manipulations involved, the different selection levels have to be carefully optimized for minimum over-all dead-time losses. Corresponding to their speed of decision, several broad classes of trigger selection can be specified.

4.2.1 Fast trigger

If prompt signals from the fastest detector components, e.g. scintillators or Čerenkov counters, are combined into simple coincidence or true/false logic tests, a fast decision can be obtained within 100 ns after the event. Owing to the precise timing requirement and the complexity and cost of the corresponding fast logics, this fastest decision level is usually limited to about 100 signals and simple logic manipulations only. A wide range of standardized fast electronics equipment (NIM Standards) is available, and the improvement of these standards with respect to packing density and signal transfer is actively pursued (Verweij 1979).

4.2.2 Secondary trigger

More complex decisions on up to a few hundred channels can be performed on a secondary trigger level in a time interval of the order of 1 μs. Signals are still brought in directly from the detectors, but without stringent timing requests ("d.c." logics, see for example Brandt 1975). Rather involved logical

tests such as matrix coincidences, correlation tables, or coarse track-finding (Bell 1975, Platner 1977) can be performed.

4.2.3 On-line processors

A third level of decision, working on logical or encoded signals from the detectors in a time interval between 10 and 100 μs, is covered by the so-called hardware processors (Verkerk 1975). They are widely used in connection with wire chambers, as hard-wired (Mehrgardt 1973, Solomon 1973) and as programmable devices (Brafman 1978, Lingjaerde 1978). With the advent of fast analog-to-digital converters (ADCs) and time-to-digital converters (TDCs), it has become feasible to base complex event decisions (e.g. momentum computation on charged tracks, energy distribution in calorimeters) on this detailed information. This will be helped by the increased use of powerful, programmable microprocessors.

4.2.4 On-line filtering

On-line filtering works on all or on a subgroup of the available data after read-out -- its speed is thus determined by the read-out cycle and the analysis to be performed on the data. As the last step in data reduction before recording, it operates typically on a time scale of 10-100 ms. At this level, pattern recognition and track fitting using the full resolution of the detectors is possible, as well as the use of analog information such as pulse heights from calorimeters. The calculations are normally performed on small, dedicated "mini" computers coded in machine language. However, the development of microprocessor systems emulating known computers will greatly facilitate programming and debugging of filter algorithms in the future, while inherently allowing for a decisive speed-up of the decision. Multiprocessing systems using parallel processing of events and emulators that permit the use of full off-line analysis routines will be introduced during the next years (Kunz 1979).

4.2.5 Monitoring and control

Large detector systems grow unmanageable without the appropriate provisions for monitoring and control. Today, many detector parameters such as magnet currents, gas composition, gas pressure, or detector positions are preselected and

set under computer control. A second, more profound problem is the monitoring and checking of these parameters and the detector performance itself. The function of every signal channel has to be monitored, and with the increased use of analog information the exact calibration of absolute pulse heights from proportional chambers or photomultipliers has to be known to an accuracy of $\sim$ 1%. Calibration procedures via test pulses have to be foreseen at regular time intervals. For charge-sensitive detectors, electronics calibration pulses are injected close to the signal source (Willis 1974, Cobb 1979). The gain of photomultipliers, which can fluctuate considerably in time, is controlled by reference light-pulses from flash-lamp or laser-light sources (Appel 1975, Madaras 1979). Radioactive sources are employed for calibration and gain control of MWPCs (Lehraus 1978).

During data taking, a test sample of events can be analysed for control purposes on the on-line computer. A large part of the on-line data-handling load is thus determined by these monitoring tasks.

Finally, the usually rather complex trigger systems described above require control. The considerable reduction of data achieved in each decision step has to be carefully monitored for efficiency and stability. Here, the availability of writeable storage registers has made it possible to feed simulated test events into the trigger logic at different levels (Brafman 1978) in order to perform a complete test procedure.

4.3 Off-line analysis and event reconstruction

After read-out and transfer to the storage device, e.g. a magnetic tape, the detector information forms a considerable quantity of raw data -- up to tens of thousands of bits per event in large detectors. This bulk of data has to be transformed into physics quantities. Momentum vectors have to be determined from correlated space coordinates. Particle energies or masses have to be assigned using analog and logical information from different detector components. In order to arrive at a final reconstruction of the real event, a large amount of data manipulations is needed.

In a first step, the raw data are decoded and transformed into space coordinates or absolute pulse heights. With the modern detectors, this task can be rather involved: coordinate information may be hidden in a drift-time measurement or in a combination of pulse heights subject to calibration procedures and systematic corrections.

In a second step the complete event topology has to be determined from the microscopic bits of detector information. This concerns track finding and pattern recognition procedures as well as correlation of data from different types of detectors.

It is well known that the human eye has an admirable capability for pattern recognition even in the presence of severe uncorrelated backgrounds (Ruddock 1977). To tell a computer how to do this requires a lot of effort and experience. Clearly, pattern recognition depends critically on the density of information available. In the bubble chamber picture of figure 4, the interesting event can be detected and each track followed in spite of the many background tracks, since the average distance of bubbles along the tracks is only of the order of 1 mm. Several methods for automatic scanning of bubble or streamer chamber pictures are now available (ERASME 1974, PEPR 1970, Van Dam 1974). They have been explored up to high track multiplicities, but they are rather time-consuming: one has to count several seconds of processing time per event.

In purely electronic detectors, for instance proportional chambers, the information density is usually much reduced, down to a level of 10 or less coordinates per track. Here, the track-finding problem becomes much more severe, especially for high track multiplicities, although the number of background tracks is generally negligible owing to the good time resolution of the devices. If a track cannot be followed in small segments, pattern recognition tends to be dominated by combinatorial possibilities; hence, again, a large amount of computer time is needed, and in addition this time grows quickly with track multiplicity. Nevertheless, it has been proved that pattern recognition will work in electronics detectors up to track multiplicities of 40 with as few as 6 to 8 coordinates per track on the average (Froehlich 1976). One example from the Split-Field Magnet (SFM) detector

at CERN (see § 4.4) is shown in figure 34. Notice also the cleanliness of the event in terms of background tracks: the event rate in this particular case approached 1 MHz.

Since most track detectors work inside magnetic fields, the track-finding algorithms are influenced by the field distribution. Preference is given to field configurations with simple symmetry properties (e.g. solenoids, toroids), for which tracks can be simply transformed into straight-line projections. However, parametrization methods which estimate track parameters such as the momentum by linear combinations of coordinates (Wind 1972) have been shown to work also in rather complex field geometries and have therefore considerably reduced the constraints on field shapes (Zanella 1973).

With the newly developed "jet chambers" and "time projection chambers" (see § 2.4.3), the electronic detectors will approach the visual devices in their pattern recognition capabilities.

4.4 Some typical examples of detector systems

At CERN, four major particle accelerator facilities provide beams for altogether about 100 high-energy physics experiments. From the detector point of view, these experiments display an impressive arsenal of all the detection techniques and developments discussed in the preceding sections. In order to give a feeling for the size and sophistication which these detector systems have reached and for the evolution of detector technology involved, we have chosen some typical experimental facilities which have been built in recent years or are under construction now. Experiments of comparable complexity are also found at the other high-energy laboratories.

4.4.1 The Split-Field Magnet facility (SFM)

Designed in 1970, the Split-Field Magnet is one of the first detectors to exclusively employ MWPCs as track detectors (Bouclier 1974). It is still the biggest operating MWPC system: 70,000 sense wires of 20 μm diameter are installed in more than 200 detector planes inside the magnetic field volume of 40 m^3 (see figure 35). The reliability of this big apparatus is nevertheless impressive:

with a yearly total of about 3000 hours of data taking, the system has been working for up to two years without breakdown or repair of the wire chambers.

The detector was the first instrument to explore the problem of automatic event reconstruction in the domain of very high track multiplicities. Events with up to 40 charged tracks are handled by the off-line analysis programs (see figure 34). Several seconds of computing time are needed to reconstruct these events. The track-finding efficiency has been shown to be independent of track multiplicity, at a level of 85% to 90%.

In addition to its proportional chambers, the facility uses large atmospheric Čerenkov counters (Č), a liquid-argon calorimeter, time-of-flight scintillators (TOF), and multiple energy-loss measurements for particle identification. Typical interaction rates are of the order of 10^6 Hz. The trigger system uses a fast decision within the first 500 ns, a secondary trigger level operating within 5 μs, and an on-line filter selecting track candidates within 5 ms. The final rate of data recording is of the order of 10 to 60 Hz.

4.4.2 The Axial Field Spectrometer (AFS)

This spectrometer was built to study pp collisions at the CERN ISR which are characterized by a very large transverse energy flow (figure 36). The magnet was designed to allow a very large, unrestricted aperture around 90° with respect to the proton beams. The track detector is a drift chamber of the type shown in figure 8c, giving up to 42 measurements of unambiguous space points. Different external detectors, depending on the physics emphasis, can be used in conjunction with this magnetic spectrometer: a Čerenkov counter system, consisting of three threshold counters (Aerogel with a threshold $\gamma \simeq 5$; followed by a counter filled with freon at 4 atm, $\gamma_{thresh} \simeq 10$; and one filled with freon at 1 atm, $\gamma_{thresh} \simeq$ $\simeq 20$). A large fraction of the azimuth (up to 2π) will be covered with a hadron calorimeter, of the uranium/scintillator type (figure 31) to measure the transverse energy flow of pp collisions. Complex trigger processors, using the coordinate information from the drift chamber, select high-p_T charged particles; different, very fast processors (decision time less than 1 μs) use the energy distribution

patterns in the calorimeter to select especially interesting, very rare events. These trigger processors must achieve a selectivity of typically 1 in 10^6 to allow the study of these very rare hard-scattering processes between the nucleon constituents.

4.4.3 The NA5 experiment

This detector (Seyboth 1975) is operating in a secondary hadron beam at the CERN Super Proton Synchrotron (SPS). Interactions take place in a hydrogen target (see figure 37). A large streamer chamber inside a dipole magnet acts as the vertex detector, and records charged secondaries with essentially no limitation on track multiplicity. Figure 11 demonstrates the excellent quality of multitrack detection in the streamer chamber. Outside the magnetic field, a large array of magnetostrictive spark chambers are used for further tracking. A photon-hadron calorimeter (Eckardt 1978) is analysing narrow "jets" of charged and neutral particles. The incoming hadron beam has an intensity of a few times 10^6 particles/s, producing about 10^4 interactions/s. A trigger reduction of about 10^3 is needed to match this with the repetition rate of the streamer chamber, which is about 10 Hz.

4.4.4 The WA1 experiment

This experiment studies neutrino interactions at the highest energies available at the CERN SPS. The basis of the experiment is a massive calorimeter which serves several functions simultaneously (figure 38). The large mass of this calorimeter (about 1400 tons) is used as an active target for neutrino interactions. The energy of the reaction products is measured by calorimetric techniques: iron planes of 5 cm and 2 cm thickness are used as the passive absorber, with 1 cm gaps provided for the read-out using scintillator planes. Coils of electrical conductor are arranged around groups of iron plates to induce a toroidal magnetic field. This provides, in combination with large-area drift chambers, a momentum measurement of secondary muons -- a characteristic product of neutrino interactions.

More recently, developments in calorimetric detectors for neutrino physics have been aiming at the improved measurement of the total energy of the reaction products and of the directions of energy flow. The former is needed, for example,

for estimates of invisible energy carried away by secondary "prompt" neutrino production, as is the case in charmed meson production; the latter feature is required in the study of neutral-current events, where no secondary muon is produced (see, for example, figure 32).

4.4.5 The UA1 experiment

This 4π solid-angle detector system which is at present under construction for the CERN proton-antiproton collider facility (Rubbia 1978), is one of the biggest and most complex spectrometers conceived so far. A large dipole magnet with 80 m^3 field volume (see figure 39) surrounds a cylindrical track detector.

This detector is of the time-projection type (§ 2.4.3) and employs 20 cm drift cells. It contains 10^4 sensitive wires reading both pulse height (for current division and ionization measurement) and time information (for optimum space resolution).

It is surrounded by electromagnetic and hadronic calorimeters covering the full solid angle. The calorimeters use scintillator sampling (§ 3.4) and are read out by about 2000 photomultipliers.

This impressive number of analog electronics channels will create an equally impressive amount of data. Hadronic events at collider energies will produce total multiplicities of typically 20 to 50 secondary particles. One event registered with this detector will have more than 10^4 words of information, representing a data flow of more than 1 Mbyte/s.

4.4.6 The EMC experiment

A large facility consisting of many different detector components has been developed to study deep inelastic muon scattering and to allow an investigation of the final states.

The layout of this apparatus (figure 40) is indicative of "spectrometer" experiments. The interaction of muons takes place in a large liquid-hydrogen target. The secondary particles are momentum-analysed in a large magnet drift-chamber set-up, followed by a Čerenkov counter, a hadron calorimeter and absorber, MWPCs, and scintillators. This detector array is used for optimum identification

and momentum measurement of the scattered muons. Additional detection equipment, which will be placed around the target, is being prepared: a streamer chamber in a "vertex" magnet will surround the target in order to provide information on final states and to study special reaction channels, such as the production of charmed particles and hadronic jets by virtual photons.

The size of this facility is typical of the large installations at today's fixed-target machines. It also illustrates how different detector techniques are integrated in an attempt to provide complete information on the secondary reaction products.

5. FUTURE DEVELOPMENTS

In previous sections we have discussed the state of the art of detection techniques for elementary particle physics. A few already well-known fundamental concepts have been applied with increasing sophistication; this trend was imposed by the requirements of new particle machines, stimulated by the advances in particle physics, and made possible by new technologies.

It is likely that this pattern will continue throughout the next decade. In table 10 the characteristic features of some machines are discussed; these are expected to come into operation during this time, and will impose new requirements on detector techniques.

The new storage ring machines will be at the forefront of particle physics research; the necessary detector development will be directed towards the needs imposed by the energy, the interaction rate, and the event topology characteristic of these machines, and will be guided by the planned physics programme. It is expected that also in the future generations of detector facilities, several "all-purpose" detectors will coexist with emphasis on different event features. The connection between progress in detector physics and technological advances is traced in table 11 for the example of track chambers. Low-noise electronics has recently suggested (Charpak 1979b) the use of parallel-plate proportional chamber structures allowing a new degree of freedom in track chamber design. A further reduction in the price and size of analog-to-digital converters would

Table 10

New storage ring machines with new detector requirements

Name	Type	Expected 1st operation	Energy	Interactions/s	Basic features of interaction	Principal detector requirements
CERN $p\bar{p}$-collider (under construction)	Proton-antiproton storage ring	1981	270 GeV × 270 GeV	10^3 to 10^4	Multi-jet events; typically two forward and two or more large-angle jets requiring essentially 4π detection geometry	Very good multi-track capability; forward detectors; calorimetry
FNAL $p\bar{p}$-collider (under construction)	Proton-antiproton storage ring	1982	1000 GeV × 1000 GeV	10^2 to 10^4	As above	As above
ISABELLE at Brookhaven National Lab. (under construction)	Proton-proton storage ring	1986	400 GeV × 400 GeV	10^6 to $\sim 5 \times 10^7$	As above	As above; very high rate capability; excellent trigger and selection criteria for "unusual" events
LEP (in planning stage)	Electron-positron collider	End of 1980's	$\sim$ 120 GeV × $\sim$ 120 GeV	$\sim 10^{-3}$ to 1	Multi-jet events; all particles are frequently emitted at large angles	Extended use of calorimeters indicated, as total beam energy is frequently converted into detectable particles

Table 11

Interdependence of detector physics and technologies (track chambers)

Principles	Electronics	Mode of operation
Search for gases with smaller diffusion at lower E/P → Higher resolution, larger TPCs; measurement of primary ionization clusters; 10 μm intrinsic resolution	Low noise ($\leq 10^3$ e r.m.s.) charge amplifiers	Low gas gain → Parallel-plate structures (no more wires?) → Multigap structures
	Centre of gravity t_D electronics	
	Highly integrated electronics	TCPs with $\geq 10^5$ pads

enable centre-of-gravity techniques to localize tracks with unprecedented precision. Already one discusses electronics schemes allowing 4- to 6-bit digitization of wave forms every few nanoseconds. Provided suitable proportional chambers geometries can be found, such ultra-rapid wave-form analysis would produce an image of the primary ionization cloud surrounding a particle track on the scale of 10^{-2} cm. It is hoped that this refined analysis of a particle's signature could help in its identification.

Similarly (table 12) progress in the understanding and the technology of calorimetric methods may have important consequences for the optimization of future large detector facilities. These techniques are relatively new, but with the steadily increasing energy of accelerators, absorptive spectroscopy will eventually replace magnetic methods. The physics at these energies may suggest replacing the momentum measurement of one particle by the determination of the momentum of a jet of many individual particles.

The density of information expected from these future detectors will impose radically new methods of information processing (table 13). The new "Fast Bus" system will become the standard for fast digital signal transmissions for the 1980's, replacing to a considerable extent the present CAMAC system. This will allow sophisticated preselection adapted to the new level of data density. The on-line computer system will have integrated powerful processors, with an instruction set identical to and a processing speed approaching that of large computers, such as a CDC 7600 or an IBM 370/78.

Possibly the role of the traditional computer centres will expand to administer a whole array of such processors, via large main-frame computers and advanced input/output facilities; this should give to the experimental groups a factor of 10 increase in computing power over the present level of typically 0.3 to 0.5 of a CDC 7600.

While these scenarios of more complex and refined detection systems appear to us rather reasonable extrapolations, we must always be prepared to accommodate unexpected developments in detector physics. However, nobody can anticipate the impact, on detector requirements, of new discoveries in elementary particle physics in the exciting years ahead of us.

Table 12

Interdependence of detector physics and technologies (calorimeters)

Principles	Electronics	Mode of operation
Improved understanding of limitation to energy resolution in hadron calorimeters → needs	Gain stability at $\sim$ 1%, gain monitoring at 0.1% of $\sim 10^5$ analog channels	← needs: Further development on fine-grain shower read-out → Very high spatial resolution for electromagnetic and hadronic showers → Helps or allows pattern recognition of very complex events (jets, ...)
Calorimeters replace magnetic spectrometers at high energies	Operational systems of $\sim 10^5$ light- or charge-measuring channels	
Particle identification through energy deposit pattern (μ, e, γ, π^0, n, $\bar{p}$, K_L^0, ν)	Cheap, fast ADCs for high-level fast trigger decisions	

Table 13

Possible information flow in future large facilities

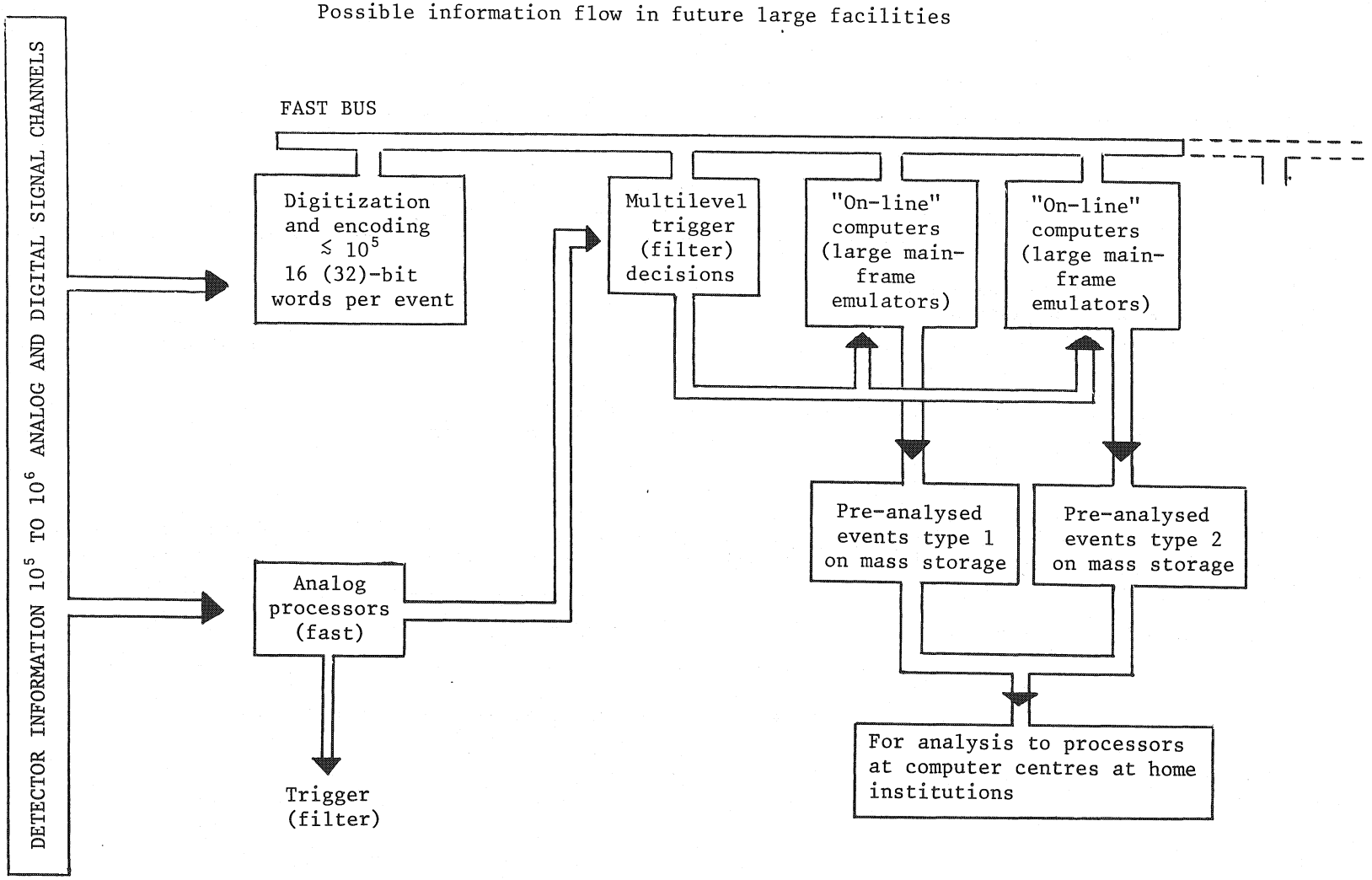

REFERENCES

Aderholz MP, Lazeyras P, Lehraus I, Matthewson R and Tejessy W 1974 *Nucl. Instr. and Meth.* 118, 419

Alikhanian AI 1963 *JETP* 44, 1122

Alikhanian AI 1973 *Proc. 5th Int. Conf. on Instrumentation for High Energy Physics*, Frascati, ed S Stipcich (Frascati: CNEN) p. 350

Alikhanian AI, Baskakov VI, Chernyatin VK, Dolgoshein BA, Fedorov VM, Gavrilenko IL, Kantserov VA, Lebedenko VN, Maiburov SN, Shmeleva AP and Vasilyev PS 1978 *CERN Proposal* SPSC/P 126

Allison WWM, Brooks CB, Bunch JN Pleming RW and Yamamoto RK 1976 *Nucl. Instr. and Meth.* 133, 325

Allison WWM, Brooks CB and Holmes AR 1978 *Nucl. Instr. and Meth.* 156, 169

Allison WWM, Brooks CB, Lyons L, Romaya AM, Shield PD and McPherson A 1979 *Nucl. Instr. and Meth.* 163, 331

Allkofer OC, Dau WD and Grupen C 1969 *Spark chambers* (Munich: Thiemig)

Anderson RL, Ash WW, Gustavson DB, Rich K, Ritson DM, Johnson JR, Prepost R and Wiser DE 1978 *IEEE Trans. Nucl. Sci.* NS-25, 340

Andresen RD, Leiman EA and Peacock A 1977 *Nucl. Instr. and Meth.* 140, 371

Appel JA, Bourquin MH, Gaines I, Hom DC, Lederman LM, Paar HP, Repellin JP, Saxon DH, Snyder HD, Weiss JM, Yoh JK, Brown BC, Brown CN, Gaillard JM, Sauer JR and Yamanouchi T 1975 *Nucl. Instr. and Meth.* 127, 495

Artru X, Yodh GB and Menessier G 1975 *Phys. Rev. D* 12, 1289

Atač M 1975 editor of *Proc. Calorimeter Workshop*, FNAL (Batavia, Ill.: FNAL)

Atač M, Bosshard R, Erhan S and Schlein P 1977 *Nucl. Instr. and Meth.* 140, 461

Atwood WB, Prescott CY, Rochester LS and Barish BC 1976 *SLAC Techn. Note* SLAC-TN-76-7

Ballam J, Blumberg R, Mark J, Skarpaas K and St. Lorant SJ 1966 *Proc. Int. Conf. on Instrumentation for High Energy Physics*, Stanford (Stanford: SLAC) p. 107

Ballam J and Watt RD 1977 *Ann. Rev. Nucl. Sci.* 27, 75

Barish BC 1977 *Caltech Report* CALT-68-623

Bathow G, Freytag E, Köbberling M, Tesch K and Kajikawa R 1970 *Nucl. Phys.* B20, 592

Bell W, Chesi E, Cooper R, Fischer HG, Flügge G, Frehse H, Gottfried C, Heck B, Innocenti PG, McLaren I, Minten A, Sciré M and Wegener D 1975 *Nucl. Instr. and Meth.* 124, 437

Bella F, Franzinetti C and Lee DW 1953 *Nuovo Cimento* 10, 1461

Benot M, Bertrand JC, Maurer A and Meunier R 1979 *CERN preprint* EP/79-51

Benot M, Carlson PJ, Tavernier S, van den Bogaert F, Henri VP, Herquet P, Kesterman J, Pingot O, Johansson KE, Norby J and Lagnaux JP 1978 *Nucl. Instr. and Meth.* 154, 253

Benot M, Howie JM, Litt J and Meunier R 1973 *Nucl. Instr. and Meth.* 111, 397

Bethe HA 1930 *Ann. Physik* 5, 325

Bethe HA 1933 *Hdb. Physik* 24, 518

Birks JB 1964 *Theory and practice of scintillation counting* (London: Pergamon Press)

Blunck O and Leisegang S 1950 *Z. Phys.* 128, 500

Bohr N 1913 *Phil. Mag.* 25, 10

Bouclier R, Charpak G, Dimčovski Z, Fischer HG, Sauli F, Coignet G and Flügge G 1970 *Nucl. Instr. and Meth.* 88, 149

Bouclier R, Charpak G, Chesi E, Dumps L, Fischer HG, Hilke HJ, Innocenti PG, Maurin G, Minten A, Naumann L, Piuz F, Santiard JC and Ullaland O 1974 *Nucl. Instr. and Meth.* 115, 235

Brafman H, Breidenbach M, Hettel R, Himel T and Horelick D 1978 *IEEE Trans. Nucl. Sci.* NS-25, 692

Brand C, Brown RCA, Chesi E, Foeth H, Gilgrass A, Hilke HJ, Jacobs D, Lazeyras P and Sacquin Y 1976 *Nucl. Instr. and Meth.* 136, 485

Brandt A, Dibon H, Flügge G, Niebergall F, Schubert KR, Schumacher PE and Wilmsen W 1975 *Nucl. Instr. and Meth.* 126, 519

Brandt S, Grupen C, Roschangar M, Schofer B and Knies G 1977 *Nucl. Instr. and Meth.* 145, 593

Braunschweig W, Königs E, Sturm W and Wallraff W 1976 *Nucl. Instr. and Meth.* 134, 261

Breskin A, Charpak G, Sauli F, Atkinson M and Schultz G 1975 *Nucl. Instr. and Meth.* 124, 189

Breskin A, Tserruya I and Zwang N 1978 *Nucl. Instr. and Meth.* 148, 275

Brooks FD 1979 *Nucl. Instr. and Meth.* 162, 477

Buchholz H 1957 *Elektrische und magnetische Potentialfelder* (Berlin: Springer)

Camilleri L, DelPapa C, Di Lella L, Doughty F, Harfield R, Onions CJ, Pope BG, Pordes SH, Singh J, Smith AM, Wind H, Blumenfeld BJ, Hollebeek RJ, Cunitz H, Lederman LM, Levinthal D, Sippach W, Vidal RA, Angelis ALS, Lyons L, Phinney N, Segar AM, Wallace JS, White TO, Chapin TJ, Cool RL, Dimčovski Z, Rothenberg AF and Tannenbaum MJ 1978 *Nucl. Instr. and Meth.* 156, 275

Camps C, Commichan V, Deutschmann M, Göldeke H, Hangarter K, Liesmann W, Pützhofen U and Schulte R 1975 *Nucl. Instr. and Meth.* 131, 411

Cantin M, Casse M, Koch L, Jonau R, Mestreau P, Roussel D, Bounin F, Moutel J and Teichner SJ 1974 *J. Chim. Phys.* 71, 1537

Ceradini F, Queru P, Rubbia C, DiBitonto D, Hanna D and Schinzel D 1978 *Nucl. Instr. and Meth.* 156, 171

Čerenkov PA, Frank IM and Tamm IE 1964 *Nobel Lectures in Physics* (New York: Elsevier Publ. Co.)

Charpak G 1970a *Ann. Rev. Nucl. Sci.* 20, 195

Charpak G 1978a *Physics Today*, October, p. 23

Charpak G, Bouclier R, Bressani T, Favier J and Zupančič Č 1968 *Nucl. Instr. and Meth.* 62, 235

Charpak G, Fischer HG, Gruhn CR, Minten A, Sauli F, Plch J and Flügge G 1972 *Nucl. Instr. and Meth.* 99, 279

Charpak G, Majewski S and Sauli F 1975 *Nucl. Instr. and Meth.* 126, 381

Charpak G, Majewski S, Sauli F and Ypsilantis T 1979a *Nucl. Instr. and Meth.* 161, 19

Charpak G, Melchart G, Petersen G and Sauli F 1979b *CERN preprint* EP/79-90

Charpak G, Petersen G, Policarpo A and Sauli F 1978b *Nucl. Instr. and Meth.* 148, 471

Charpak G, Rahm D and Steiner H 1970b *Nucl. Instr. and Meth.* 80, 13

Chechin VA and Ermilova VC 1976 *Nucl. Instr. and Meth.* 136, 551

Chechin VA, Kotenko LP, Merson GI and Ermilova VC 1972 *Nucl. Instr. and Meth.* 98, 577

Chen HH, Lathrop JF and Learned J 1978 *IEEE Trans. Nucl. Sci.* NS-25, 358

Chikovani GE, Roinishvili VN and Mikhailov VA 1964 *Nucl. Instr. and Meth.* 29, 261

Christophorou LG 1971 *Atomic and molecular radiation physics* (New York: Wiley)

Cobb JH, Allison WWM and Bunch JN 1976 *Nucl. Instr. and Meth.* 133, 315

Cobb J, Fabjan CW, Iwata S, Kourkoumelis C, Lankford AJ, Moneti G-C, Nappi A, Palmer R, Rehak P, Struczinski W and Willis W 1977b *Nucl. Instr. and Meth.* 140, 413

Cobb JH, Iwata S, Rahm DC, Rehak P, Stumer I, Fabjan CW, Harris M, Lindsay J, Mannelli I, Nakamura K, Nappi A, Struczinski W, Willis WJ, Kourkoumelis C and Lankford AJ 1979 *Nucl. Instr. and Meth.* 158, 93

Cobb JH and Miller DJ 1977a *Nucl. Instr. and Meth.* 141, 433

Comby G, Maugeot P, Augnères JL, Claudet S, Chalot JF, Tichit J, de Lignières H and Zadra A 1979 *CEA/Saclay Report* 79/06/08/227

Conversi M and Brosco G 1973 *Ann. Rev. Nucl. Sci.* 23, 75

Conversi M and Federici L 1977 *Nucl. Instr. and Meth.* 151, 93

Conversi M and Gozzini A 1955 *Nuovo Cimento* 2, 189

Criegee L, Derikum K, Franke G, Krechlok W, Knies G, Lohrmann E, Mehrgardt H, Schmitz R, Ranga Swamy TN, Timm U, Waloschek P, Winter GG and Zimmermann W 1975 *Proc. Int. Meeting on Proportional and Drift Chambers*, Dubna (Dubna report D13-9164: JINR) p. 76

Crispin A and Fowler GN 1970 *Rev. Mod. Phys.* 42, 290

Curran SC and Wilson HW 1965 *Alpha, Beta and Gamma Ray Spectroscopy*, ed K Siegbahn (Amsterdam: North Holland) p. 303

Daum H, Fabjan CW, Pordes SH, Franklin M, Dam P and Rothenberg AF 1978 *Nucl. Instr. and Meth.* 152, 541

Davidenko VA, Dolgoshein BA and Somov SV 1969 *Nucl. Instr. and Meth.* 75, 277

Davies-White W, Fischer GE, Lateur MJ, Schindler RH, Schwitters RF, Siegrist JL, Taureg H, Zaccone H and Hartill DL 1979 *Nucl. Instr. and Meth.* 160, 227

DeBoer W, Budjarek B, Fues W, Grindhammer G, Kotthaus R, Lierl H and Moss L 1978 *Nucl. Instr. and Meth.* 156, 249

Dhawan S and Majka R 1977 *IEEE Trans. Nucl. Sci.* NS-24, 270

Dolgoshein BA, Rodionov BU and Luchkov BI 1964 *Nucl. Instr. and Meth.* 29, 270

Durand L 1975 *Phys. Rev. D* 11, 89

Eckardt V, Kalbach R, Manz A, Pretzl KP, Schmitz N and Vranic D 1978 *Nucl. Instr. and Meth.* 155, 389

Eckardt V, Seyboth P, Derado I, Gebauer HJ, Odian A and Pretzl KP 1977 *Nucl. Instr. and Meth.* 143, 235

ERASME 1974 Description and status report of the ERASME system, *Proc. Oxford Conference on Computer Scanning* (Oxford: The University) p. 211

Ermilova VK, Kotenko LP, Merzon GJ and Chechin VA 1969 *Sov. Phys.-JETP* 29, 861

Erskine GA 1972 *Nucl. Instr. and Meth.* 105, 565

Ewan GT 1979 *Nucl. Instr. and Meth.* 162, 75

Eyal Y and Stelzer H 1978 *Nucl. Instr. and Meth.* 155, 157

Fabjan CW 1977a *Nucl. Instr. and Meth.* 146, 343

Fabjan CW, Lindsay J, Piuz F, Ranjard F, Rosso E, Rudge A, Serednyakov S, Willis WJ, Jensen HB and Petersen JO 1978 *Nucl. Instr. and Meth.* 156, 267

Fabjan CW and Struczinski W 1975a *Phys. Letters* 57B, 484

Fabjan CW, Struczinski W, Willis WJ, Kourkoumelis C, Lankford AJ and Rehak P 1977b *Nucl. Instr. and Meth.* 141, 61

Fabjan CW and Willis WJ 1975b *Proc. Calorimeter Workshop*, FNAL, ed M Atač (Batavia, Ill.: FNAL) p. 1

Fancher D, Hilke HJ, Loken S, Martin P, Marx JN, Nygren DR, Robrish P, Shapiro G, Urban M and Wenzel W 1979 *Nucl. Instr. and Meth.* 161, 383

Fermi E 1940 *Phys. Rev.* 57, 485

Fischer J, Fuhrmann J, Iwata S, Palmer R and Radeka V 1976 *Nucl. Instr. and Meth.* 136, 19

Fischer J, Iwata S, Radeka V, Wang CL and Willis WJ 1974 *Phys. Letters* 49B, 393

Fischer J, Okuno H and Walenta AH 1978 *IEEE Trans. Nucl. Sci.* NS-25, 794

Fischer HG, Piuz F and Ullaland O 1975 *Proc. Int. Meeting on Proportional and Drift Chambers*, Dubna (Dubna report D13-9164: JINR) p. 152

Fischer HG and Plch J 1972 *Nucl. Instr. and Meth.* 100, 515

Fisher CM 1973 *Proc. 5th Int. Conf. on Instrumentation for High Energy Physics*, Frascati, ed S. Stipcich (Frascati: CNEN) p. 21

Ford RL and Nelson WR 1978 *Stanford report* SLAC-210

Frehse H, Lapique F, Panther M and Piuz F 1978 *Nucl. Instr. and Meth.* 156, 87

Froehlich A, Grote H, Onions C and Ranjard F 1976 *CERN Internal Report* DD/76/5

Fulbright HW 1979 *Nucl. Instr. and Meth.* 162, 21

Gabriel TA, Amburgey JD and Bishop BL 1977 *Oak Ridge Report* ORNL/TM-5619

Garibian GM 1973 *Proc. 5th Int. Conf. on Instrumentation for High Energy Physics*, Frascati, ed S Stipcich (Frascati: CNEN) p. 329 and *Yerevan Report* YeFI-27

Garwin RC 1960 *Rev. Sci. Instr.* 31, 1010

Ginzburg VL and Frank IM 1946 *JETP* 16, 15

Glaser DA 1952 *Phys. Rev.* 87, 665

Gruhn CR and Edmiston MD 1978 *Phys. Rev. Letters* 40, 407

Grunberg C and LeDeveliat J 1974 *IEEE Trans. Nucl. Sci.* NS-21, 89

Gygi E and Schneider F 1966 *CERN Report* 66-14

Heath RL, Hofstadter R and Hughes EB 1979 *Nucl. Instr. and Meth.* 162, 431

Heintze J 1978 *Nucl. Instr. and Meth.* 156, 227

Hofstadter R 1975 *IEEE Trans. Nucl. Sci.* NS-22, 13

Holder M, Knobloch J, May J, Paar HP, Palazzi P, Schlatter D, Steinberger J, Suter H, Wahl H, Williams EGH, Eisele F, Geweniger C, Kleinknecht K, Spahn G, Willutzki H-J, Dorth W, Dydak F, Flottmann T, Hepp V, Tittel K, Wotschack J, Bloch P, Devaux B, Grimm M, Maillard J, Peyaud B, Rander J, Savoy-Navarro A, Turlay R and Navarria FL 1978 *Nucl. Instr. and Meth.* 151, 69

Iwata S 1979 *Nagoya Univ. Report* DPNU-3-79

Jackson JD 1977 *Classical electromagnetism* (2nd ed) (New York: Wiley) p. 685

Knies G and Glawe U 1976 *DESY Report* 76-05

Kroeger B and Werner M 1978 *Nucl. Instr. and Meth.* 156, 293

Kunz PF, Fall RN, Gravina MF, Halperin JH, Levinson LJ, Oxoby GJ and Trang QM 1979 *Stanford report* SLAC-PUB 2418

Laegsgaard E 1979 *Nucl. Instr. and Meth.* 162, 93

Landau LD 1944 *J. Exp. Physics (USSR)* 8, 201

Lecomte P and Perez-Mendez V 1978 *IEEE Trans. Nucl. Sci.* NS-25, 964

Lehraus I, Matthewson R, Tejessy W and Aderholz M 1978 *Nucl. Instr. and Meth.* 153, 347

Leutz H 1966 *CERN Internal Report* TC/BEBC 66-21, and *Nucl. Instr. and Meth.* 68, 213

Lingjaerde T 1978 *CERN Internal Report* DD/78-13

Litt J and Meunier R 1973 *Ann. Rev. Nucl. Sci.* 23, 1

Lo CC, Lecomte P and Leskovar B 1977 *IEEE Trans. Nucl. Sci.* NS-24, 302

Loeb LB 1961 *Basic processes of gaseous electronics* (Berkeley: Univ. of Calif. Press)

Lynch FJ 1975 *IEEE Trans. Nucl. Sci.* NS-22, 58

Madaras RJ, Pardoe B and Pecyner R 1979 *Nucl. Instr. and Meth.* 160, 263

McKenzie JM 1979 *Nucl. Instr. and Meth.* 162, 49

Massam T 1977 *Nucl. Instr. and Meth.* 141, 251

Mehrgardt H, Stoesser G, Waloschek P, Willutzki HJ and Winter GG 1973 *Proc. Int. Conf. on Instrumentation for High Energy Physics*, Frascati, ed S Stipcich (Frascati: CNEN) p 287

Meunier R and Maurer A 1978 *IEEE Trans Nucl. Sci.* NS-25, 528

Montanet L (spokesman) European Hybrid Spectrometer Collaboration 1976 *CERN proposal* SPSC/76-43. (See also SPSC/77-44 and 78-91)

Morton D 1975 *IEEE Trans. Nucl. Sci.* NS-22, 26

Müller D 1972 *Phys. Rev. D* 5, 2677

Murzin VS 1967 *Progress in elementary particle and cosmic ray physics*, vol IX, ed JG Wilson and IA Wouthuysen (Amsterdam: North-Holland) p. 247

Palladino V and Sadoulet B 1975 *Nucl. Instr. and Meth.* 128, 323

Particle Data Group 1978 *Phys. Letters* 75B, No. 1

PEPR 1970 Cambridge PEPR System, *Proc. Int. Conf. on Data Handling Systems*, Cambridge (Geneva: CERN 70-21) p. 61

Pietri G 1977 *IEEE Trans. Nucl. Sci.* NS-24, 228

Pisarev AF, Pisarev VF and Revenko GS 1973 *Sov. Phys.-JETP* 36, 828

Platner E 1977 *IEEE Trans. Nucl. Sci.* NS-24, 225

Policarpo A 1977 *Space Science Instrumentation* 3, 77

Radeka V 1974 *IEEE Trans. Nucl. Sci.* NS-21, 51

Raether H 1964 *Electron avalanches and breakdown in gases* (London: Butterworth)

Reinhard HP 1973 *Proc. Int. Conf. on Instrumentation for High Energy Physics*, Frascati, ed S Stipcich (Frascati: CNEN) p. 3

Rice-Evans P 1974 *Spark, streamer, proportional and drift chambers* (London: Richelieu)

Rohrbach F, Cathenoz M, Jenny J, Colas J, Fournier D, Noppe JM and Veillet JJ 1977 *Nucl. Instr. and Meth.* 141, 229

Rossi B 1964 *High-energy particles* (New York: Prentice Hall)

Rossi B and Staub H 1949 *Ionization chambers and counters* (New York: McGraw-Hill)

Rubbia C (spokesman) 1978 *CERN Proposal* SPSC/78-6, SPSC/P92

Ruddock KH 1977 *Rep. Prog. Phys.* 40, 603

Sadoulet B and Makowski B 1973 *CERN Internal Report* DPhII/Phys 73-3

Sadoulet B and Litke A 1975 *Nucl. Instr. and Meth.* 124, 349

Sauli F 1977 *CERN Report* 77-09

Sauli F 1978 *Nucl. Instr. and Meth.* 156, 147

Schröder LS 1979 *Nucl. Instr. and Meth.* 162, 395

Schultz G, Charpak G and Sauli F 1977 *Rev. Physique Appliquée* 12, 67

Séguinot J and Ypsilantis T 1977 *Nucl. Instr. and Meth.* 142, 377

Seyboth P (spokesman) NA5 Collaboration 1975 *CERN Proposal* SPSC/75-1/P37

Solomon J and Nunamaker TA 1973 *Nucl. Instr. and Meth.* 107, 15

Sternheimer RM 1952 *Phys. Rev.* 88, 851

Sternheimer RM 1956 *Phys. Rev.* 103, 511

Sternheimer RM and Peierls RF 1971 *Phys. Rev. B* 3, 3081

Talman R 1978 *Cornell Report* CLNS-368

Thévenin JC, Allemand L, Locci E, Micolou P, Palanque S and Spiro M 1979 *CEN-Saclay Report* D Ph PE 79-09

Trippe T 1969 *CERN Report* 69-18

Udo F 1980 *private communication* from the CHARM Collaboration

Van Dam PHA 1974 *Vertex guided measurement of bubble chamber pictures using HPD*, Thesis, Zeeman Lab. Amsterdam

Vavilov PV 1957 *Sov. Phys.-JETP* 5, 749

Verkerk C 1975 *CERN Internal Report* DD/75-18; also *Proc. Int. Meeting on Proportional and drift chambers*, Dubna (Dubna report D13-9164: JINR) p. 232

Verweij H 1979 *CERN preprint* EP/79-06

Walenta AH 1978 *Brookhaven Report* BNL 25153

Walenta AH, Fischer J, Okuno H and Wang CL 1979 *Nucl. Instr. and Meth.* 161, 45

Walenta AH, Heintze J and Schürlein B 1971 *Nucl. Instr. and Meth.* 92, 373

Wilkinson DH 1950 *Ionization chambers and counters* (Cambridge: University Press)

Willis WJ 1977 *Proc. Int. Conf. on Transition Radiation*, Yerevan (Yerevan: Physics Institute) p. 236

Willis WJ 1978 *Physics Today*, October, p. 32

Willis WJ and Radeka V 1974 *Nucl. Instr. and Meth.* 120, 221

Wind H 1972 *CERN Internal Reports* NP-DHG 72/16 and NP-DHG 73/2

Zanella P 1973 *Proc. Int. Conf. on Instrumentation for High Energy Phsics*, Frascati, ed S Stipcich (Frascati: CNEN) p. 477

Figure captions

Fig. 1 : Schematic view of a conceptual high-energy physics experiment. Two beams of particles collide in the centre of a large cylindrical detector arrangement, producing a large number of highly collimated secondaries. Charged particles are analysed in a track chamber (TC) inside a magnetic field (B). Their velocity is measured by a system of scintillation counters (TOF). Neutral particles (hatched areas) are detected in electromagnetic shower counters (EMC) and hadron calorimeters (HC).

Fig. 2 : Mean energy loss by ionization in argon + 5% CH_4 as a function of $\beta\gamma = p/mc$. (Measurements from Lehraus, 1978.)

Fig. 3 : Schematic view of microchannel plate and electron multiplication in a channel. (Dhawan 1977.)

Fig. 4 : Production and subsequent decay of a heavy charmed meson D^* as seen in BEBC at CERN. The original photograph, including fiducial marks (crosses) and background tracks, is shown on the left. On the right, the reconstruction of the event and the complete interpretation of its complex decay chain is given. (Courtesy D.R.O. Morrison, CERN.)

Fig. 5 : Basic structure of an MWPC. The electric field configuration corresponds to a typical structure with wires of 20 μm diameter at 2 mm distance. The influence of a slight displacement of one wire on the field geometry is indicated. (From Charpak 1970a.)

Fig. 6 : Detailed structure of a proportional chamber signal. The oscilloscope trace (a) resolves avalanches due to single electrons or small groups of electrons from primary ionization encounters. b) Computer simulation of pulse shape on the same time scale. (From Fischer 1975.)

Fig. 7 : Principle of drift chamber operation. The electrode configuration creates an almost uniform drift field towards the anode wire. Hence, the relation between track distance from the wire and drift time is linear. (From Charpak 1978a.)

Fig. 8 : Schematic representation of different geometries of MWPCs and drift chambers. (From Frehse 1978.)

Fig. 9 : Particle identification by multiple ionization measurement achieved in the External Particle Identifier at CERN. Plotted is the average pulse height of the 40% smallest recordings from 128 independent detector cells. The measured resolution is FWHM = 6%.

Fig. 10 : Principle of streamer chamber operation. The passage of a particle triggers a fast, high-voltage pulse which develops streamers in the chamber volume. The tracks are normally viewed through the transparent electrodes, parallel to the electric field. (From Schröder 1979.)

Fig. 11 : Multitrack event from the NA5 streamer chamber experiment at CERN. The distance is 100 cm between fiducial marks. (Courtesy V. Eckardt, Munich.)

Fig. 12 : Čerenkov angle as a function of particle momentum and refractive index of radiator.

Fig. 13 : Photograph of a three-stage threshold Čerenkov counter array at the CERN ISR. The first Aerogel counter, installed at the beginning of 1980, has a value of $\gamma_{thresh} = 4$, followed by a 4 atm counter filled with freon-13, $\gamma_{thresh} = 10$; an atmospheric counter, $\gamma = 20$, provides limited identification up to p = 20 GeV/c. This counter has an active detection area of approximately 20 m^2. (See also figure 36 for a schematic representation.)

Fig. 14 : The limiting velocity resolution as a function of the Čerenkov angle for threshold, differential, and DISC types of gas counters. (Benot 1973.)

Fig. 15 : Schematic representation of a ring-imaging Čerenkov counter in a geometry suitable for identification at a colliding-beam interaction region. Special UV-sensitive MWPCs are envisaged as large-area photon detectors to measure the radius of the Čerenkov ring. (Séguinot 1977.)

Fig. 16 : Geometry and nomenclature used for the simplified expression for XTR emission.

Fig. 17 : Universal yield for transition radiation from a single foil. (Artru 1975.)

Fig. 18 : Energy loss spectrum measured in an MWPC for 1.4 GeV/c pions and electrons with a "dummy" radiator and with a lithium radiator consisting of 1000 Li foils of 51 μm thickness.

Fig. 19 : Transition radiation measured in a 1.04 cm thick Xe/CO_2 (80/20)-filled MWPC after traversal by electrons through various radiator geometries. The radiator "CERN Big Li 1" contained 650 Li foils, $\sim$ 50 μm thick and with 250 μm spacing. (Cobb 1977b.)

Fig. 20 : Artist's impression of a large TR detector used in an ISR experiment for identification of electrons with $p > 1.5$ GeV/c. Four such modules are used to cover a solid angle of 4 sr. (Cobb 1977b.)

Fig. 21 : The length required for various particle identification methods and their dependence on γ. (Willis 1978.)

Fig. 22 : Measured (2 to 15 GeV) and computed (32 to 1024 GeV) longitudinal shower development for electrons. (Müller 1972.)

Fig. 23 : Longitudinal energy deposition by 6 GeV electrons in various absorbers, showing approximate scaling in radiation lengths. The measurements (solid line) agree well with Monte Carlo predictions (histogram). (Bathow 1970.)

Fig. 24 : Lateral energy distribution of 6 GeV electron showers integrated over depth, showing scaling in "Molière" units: $R_M = 21\ \text{MeV} \cdot X_0/\varepsilon$. (Bathow 1970.)

Fig. 25 : Energy resolution (standard deviation) for 1 GeV electrons. Measurements for various sampling steps are compared with the simple analytical shower model of Rossi (1964), approximation "B".

Fig. 26 : Longitudinal shower development for charged pions at various incident energies. Measurements were carried out in an iron/scintillator calorimeter. (Holder 1978.)

Fig. 27 : Calculated and measured lateral energy distribution. (Iwata 1979.)

Fig. 28 : "Visible" energy produced by electrons and hadrons in two sampling calorimeters, using iron and uranium as absorber, respectively. In calorimeters consisting of material other than uranium, the visible energy from hadrons is typically 30% smaller than the signals from electrons. If uranium is used, fission compensation results in approximately equal response. The energy scale is in arbitrary units and is different for the two calorimeters. (Fabjan 1977b.)

Fig. 29 : Energy resolution and sampling fluctuations for electrons and hadrons in a sampling calorimeter. (Fabjan 1977b.)

Fig. 30 : Schematic representation of frequently used calorimeter read-out techniques:

a) Plates of scintillator optically coupled individually to a photomultiplier.

b) Plates of scintillator read out by photon absorption and conversion in a WLS plate.

c) Charge produced in an electron-transporting medium (e.g. liquid argon) collected at electrodes, which function also as the absorber plates.

d) Charge produced in an MWPC, sandwiched between calorimeter absorber plates.

Fig. 31 : Artist's sketch of one of 128 uranium/scintillator modules, under construction at CERN for the Axial Field Spectrometer (AFS), showing the twofold longitudinal read-out. A total of 3200 photomultipliers are used to read out the energy information from this 250 ton calorimeter. The assembled facility is shown in figure 36.

Fig. 32 : A module of the ν-detector facility of the CHARM Collaboration at CERN. Neutrinos may react with the nucleons in the target calorimeter, consisting of 3 m × 3 m, 8 cm thick, marble plates, interleaved with proportional tubes and scintillator. Marble was chosen so as to minimize the differences between the electromagnetic and hadronic shower development for improved angular resolution of the reaction products. (Courtesy F. Udo, CERN.)

Fig. 33 : Schematic comparison of track chamber signal-processing electronics:

a) Typical electronics chain for an MWPC; after preamplification, the signal triggers a one-shot circuit; subsequent processing may vary, but frequently this signal is transmitted over twisted-pair cable to a "receiver", which registers the wire location and provides the corresponding signal sequence for computer-controlled recording.

b) Signal processing in modern, continuously sensitive tracking devices: controlled drift of electrons from an ionization track produces avalanches at a sense wire; the charge diffuses to the ends of the resistive sense wire (Q_ℓ, Q_r) in the ratio of the distances of impact point to the ends of the wire; the signals are amplified by low-noise preamplifiers and every 30 ns the pulse height is sampled, digitized, and recorded. This processing chain allows the measurement of unambiguous three-dimensional space points with a resolution of $\sim 0.20 \times 10 \times 10$ mm^3 and simultaneous ionization measurement. (H. Verweij, CERN, private communication.)

Fig. 34 : High-multiplicity event in the Split-Field Magnet at CERN (§ 4.4). The plane view shows about 30 tracks reconstructed from hits in the proportional chambers.

Fig. 35 : a) Layout (top view) of the Split-Field Magnet detector.
b) Photograph of the spectrometer at the CERN ISR showing additional equipment such as Čerenkov and time-of-flight counters.

Fig. 36 : Cross-section and top view of the Axial Field Spectrometer at the CERN ISR. Shown is the set-up where a large hadron calorimeter is employed together with a 1 sr particle identification detector. For a different physics phase, these Čerenkov counters may be replaced by calorimeter modules, providing a total of 8 sr coverage.

Fig. 37 : a) Layout and b) photograph of the NA5 experiment at CERN.

Fig. 38 : View of the WA1 ν-detector. Neutrinos enter the detector from the right and may interact in the magnetized iron/scintillator calorimeter. The large hexagons house drift chambers used in the momentum analysis of muons and tracking of secondaries. (Courtesy H. Wahl, CERN.)

Fig. 39 : a) Artist's view of the UA1 spectrometer in construction at CERN for the proton-antiproton facility. (Courtesy L. Naumann, CERN.)
b) Cross-section through experimental area for the UA1 experiment.

Fig. 40 : Schematic representation of the European Muon Collaboration (EMC) experimental set-up. Proportional chambers (Pi) inside a magnet and large-area drift chambers (Wi) are used for tracking and momentum analysis of muons and other secondaries. Čerenkov counters and calorimeters (Hi) provide additional information.

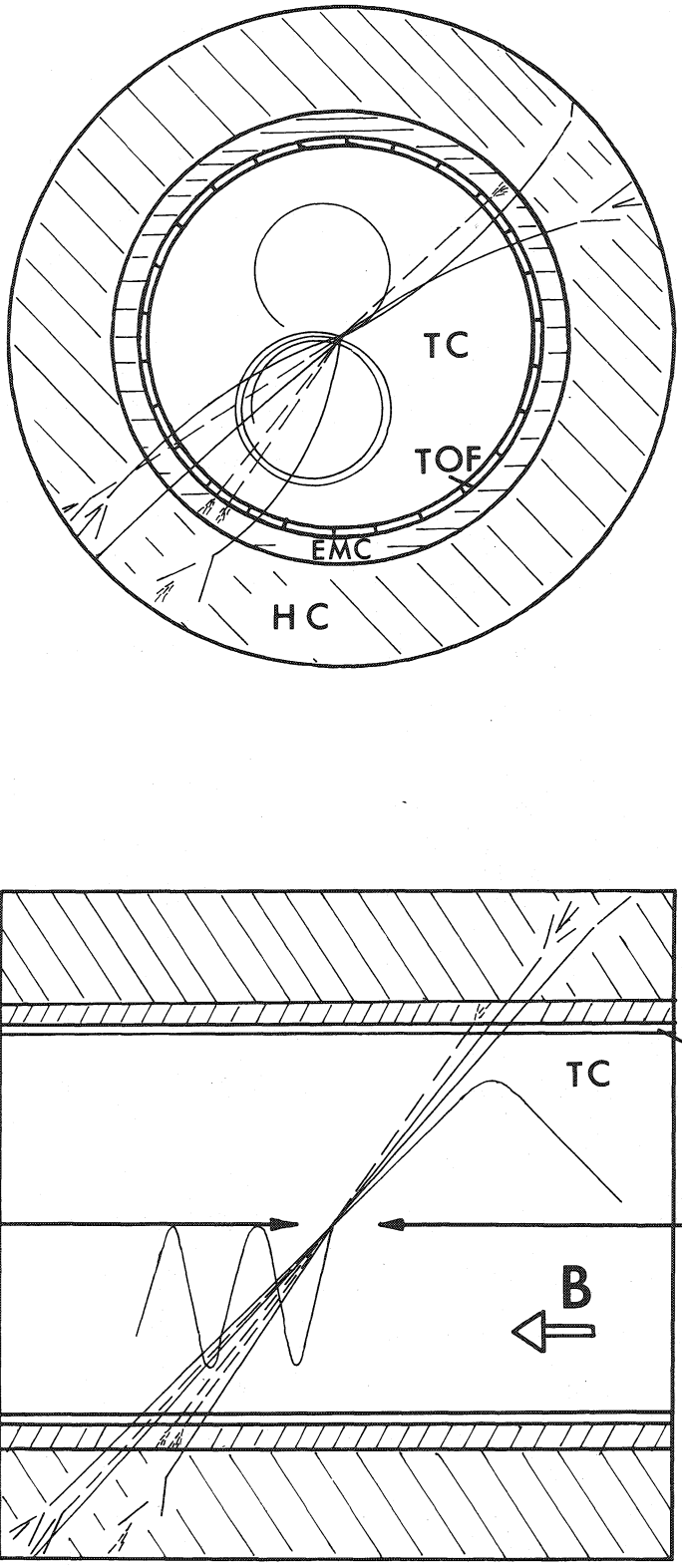

Fig. 1

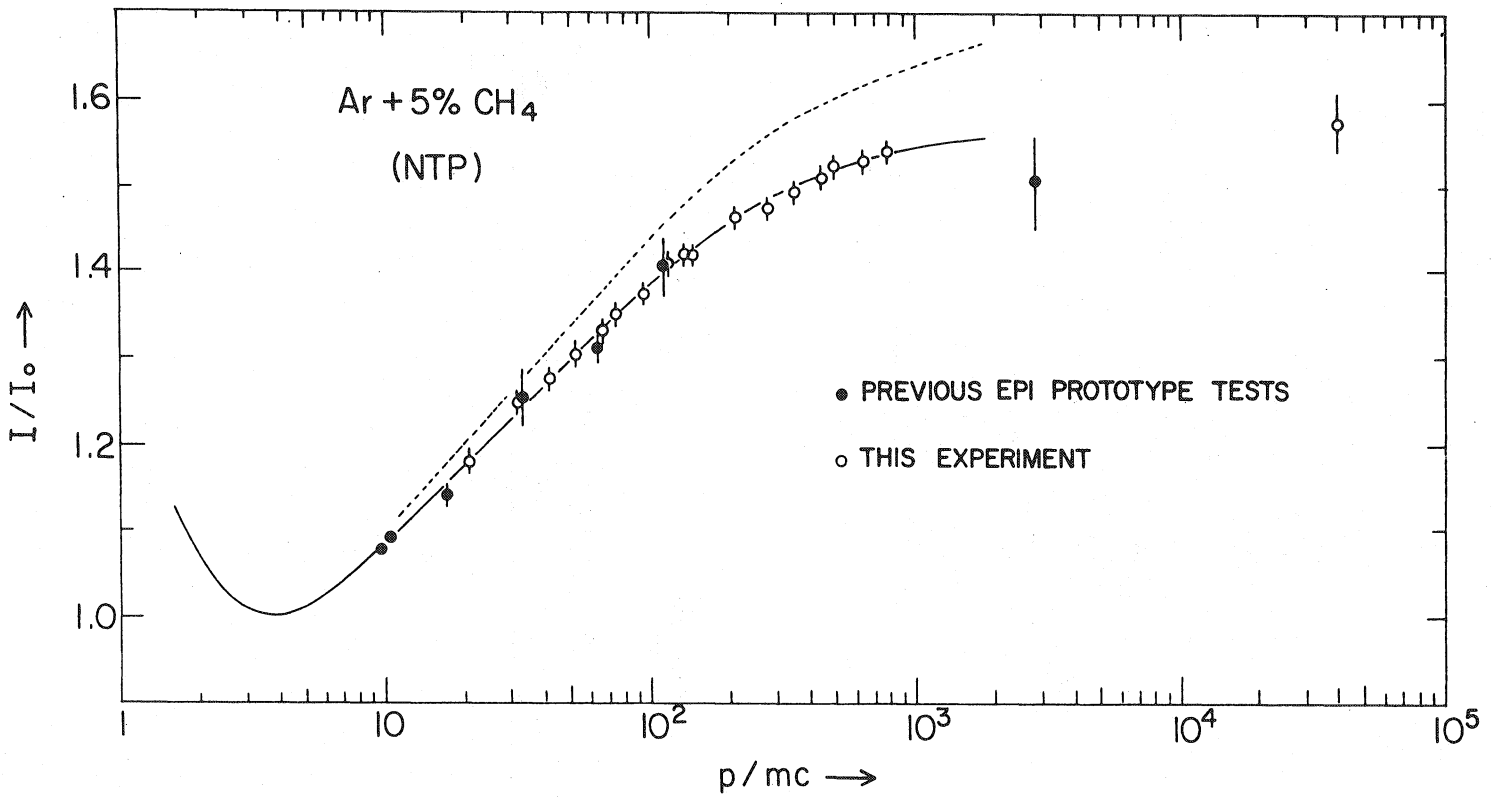
Ar + 5% CH4
(NTP)
PREVIOUS EPI PROTOTYPE TESTS
THIS EXPERIMENT
I/Io
p/mc
1.6
1.4
1.2
1.0
1
10
10^2
10^3
10^4
10^5

Fig. 2

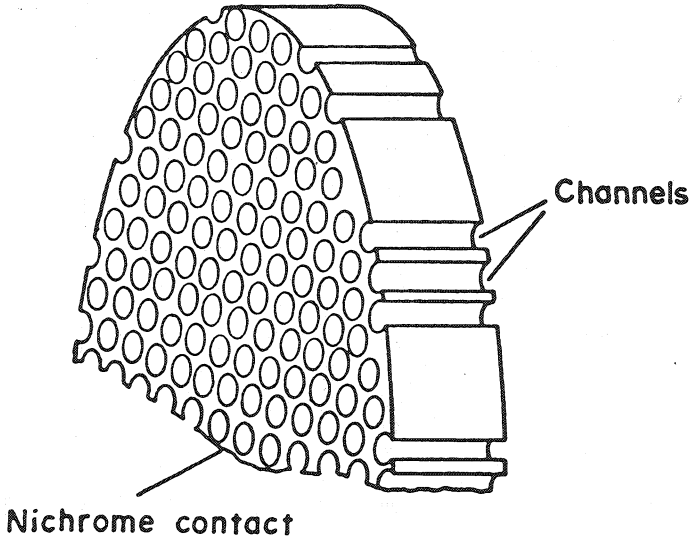
Channels
Nichrome contact

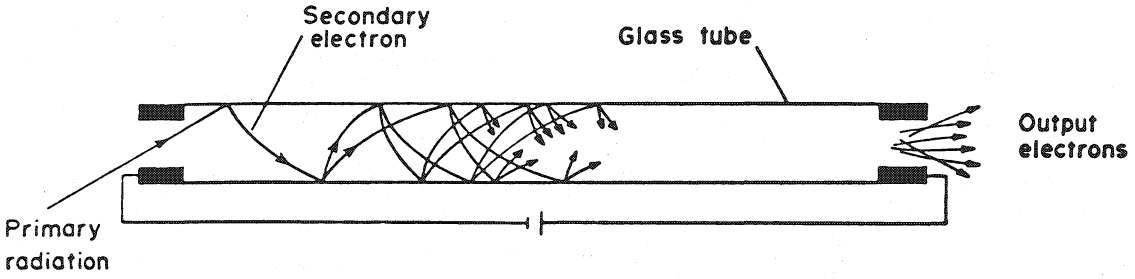
Secondary electron
Glass tube
Output electrons
Primary radiation

Fig. 3

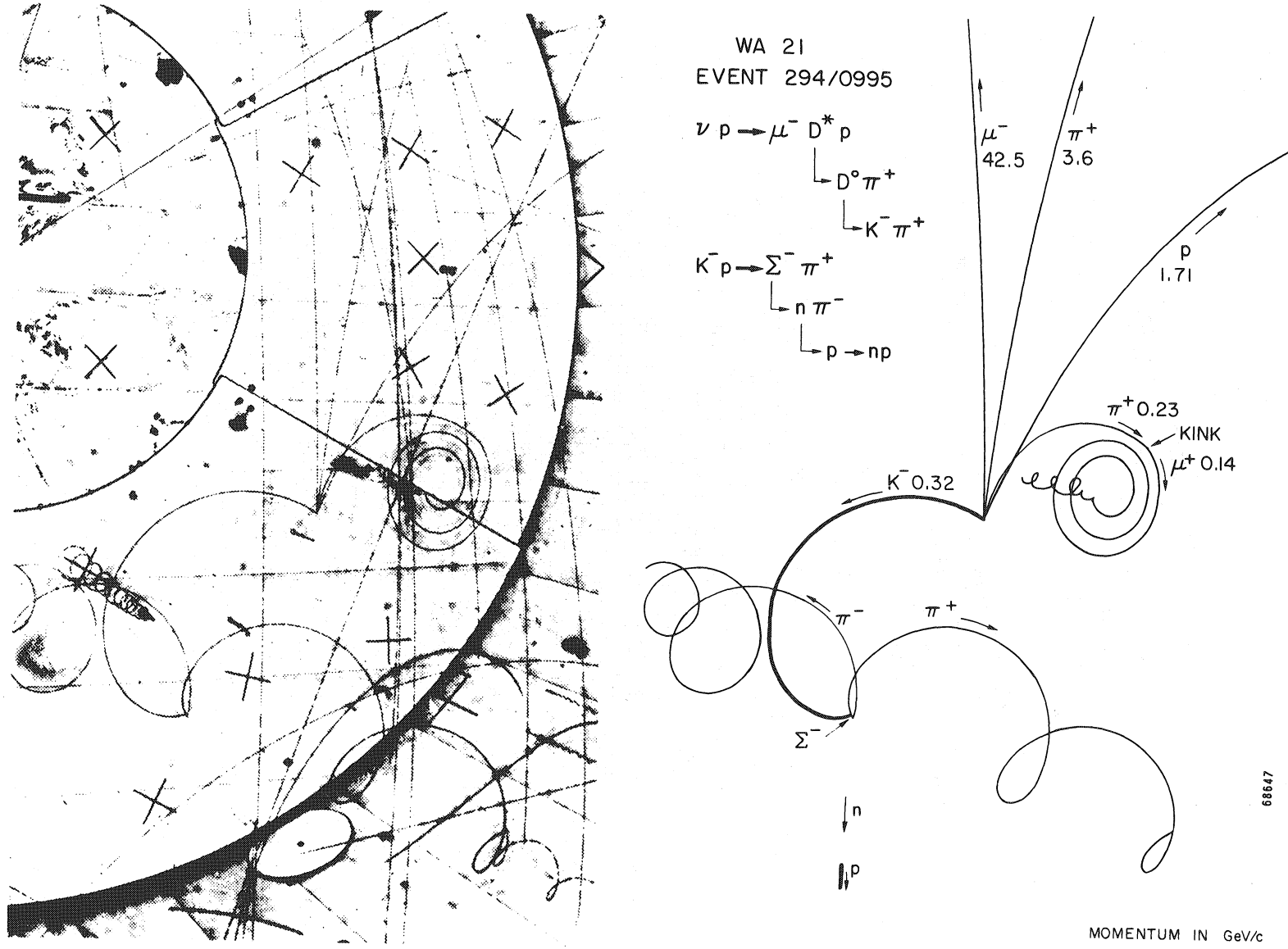
WA 21
EVENT 294/0995
$\nu p \rightarrow \mu^- D^* p$
$D^\circ \pi^+$
$K^- \pi^+$
$K^- p \rightarrow \Sigma^- \pi^+$
$n \pi^-$
$p \rightarrow np$
μ^- 42.5
π^+ 3.6
p 1.71
π^+ 0.23
KINK
μ^+ 0.14
K^- 0.32
π^-
π^+
Σ^-
n
p
MOMENTUM IN GeV/c
68647

Fig. 4

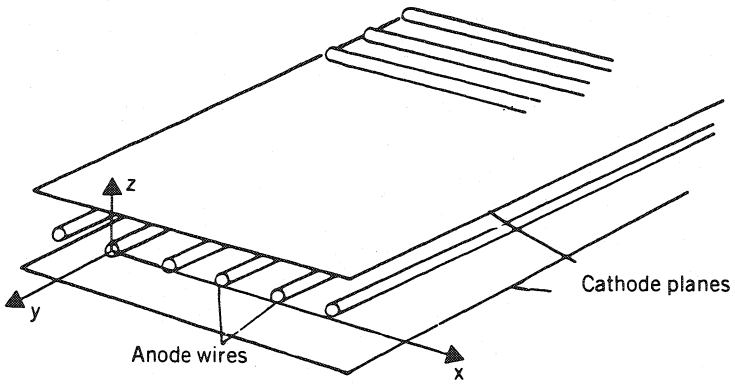

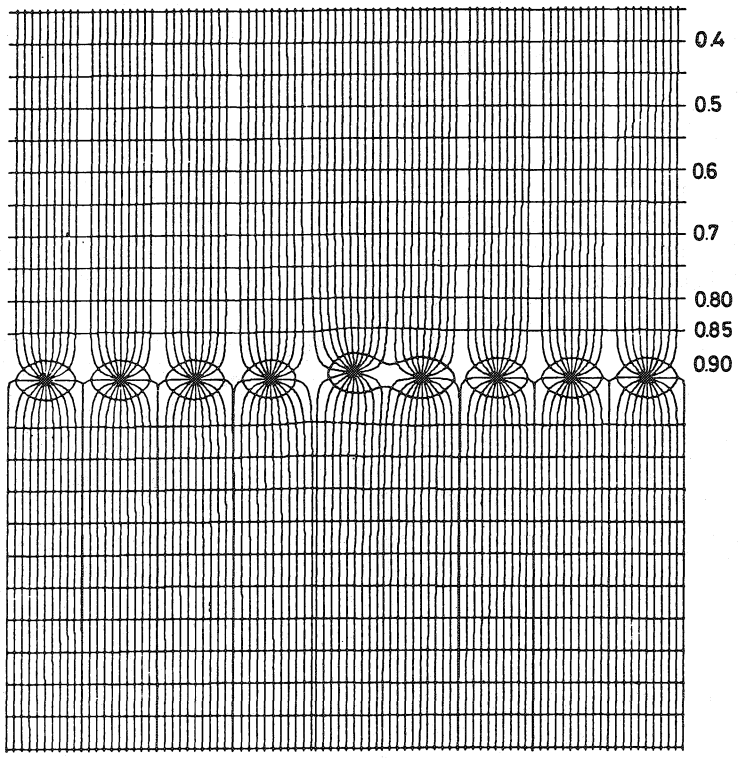

Fig. 5

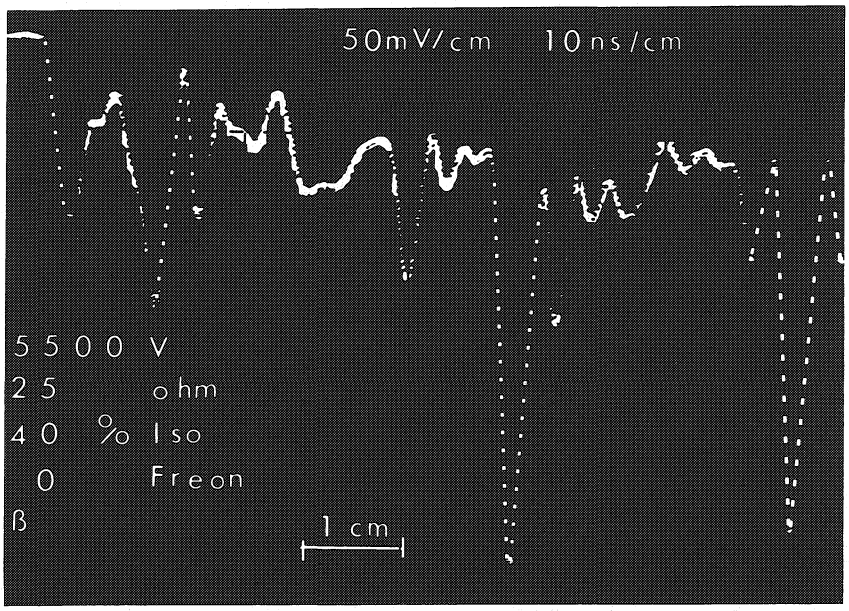
50mV/cm 10ns/cm
5500 V
25 ohm
40 % Iso
0 Freon
ß
1 cm

a)

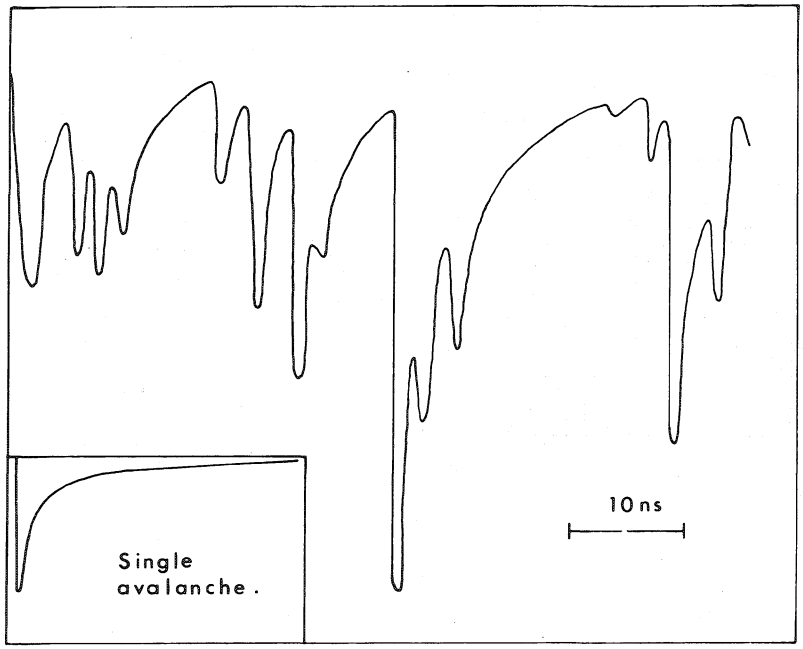
10ns
Single
avalanche.

b)

Fig. 6

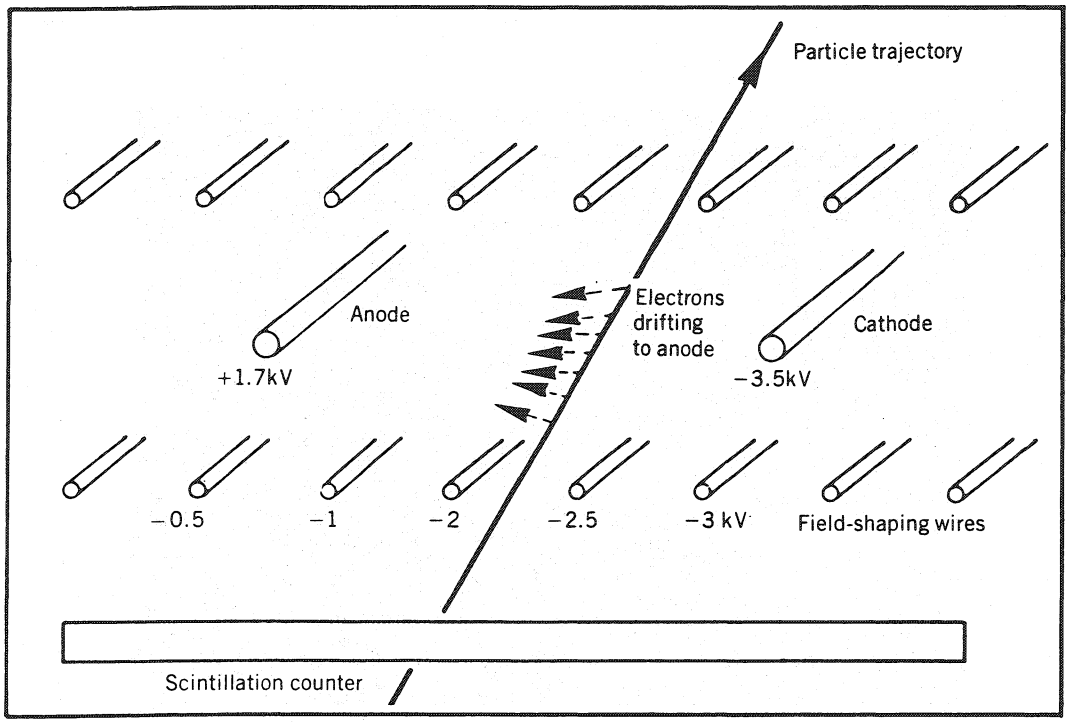
Particle trajectory
Anode
+1.7kV
Electrons
drifting
to anode
Cathode
−3.5kV
−0.5
−1
−2
−2.5
−3 kV
Field-shaping wires
Scintillation counter

Fig. 7

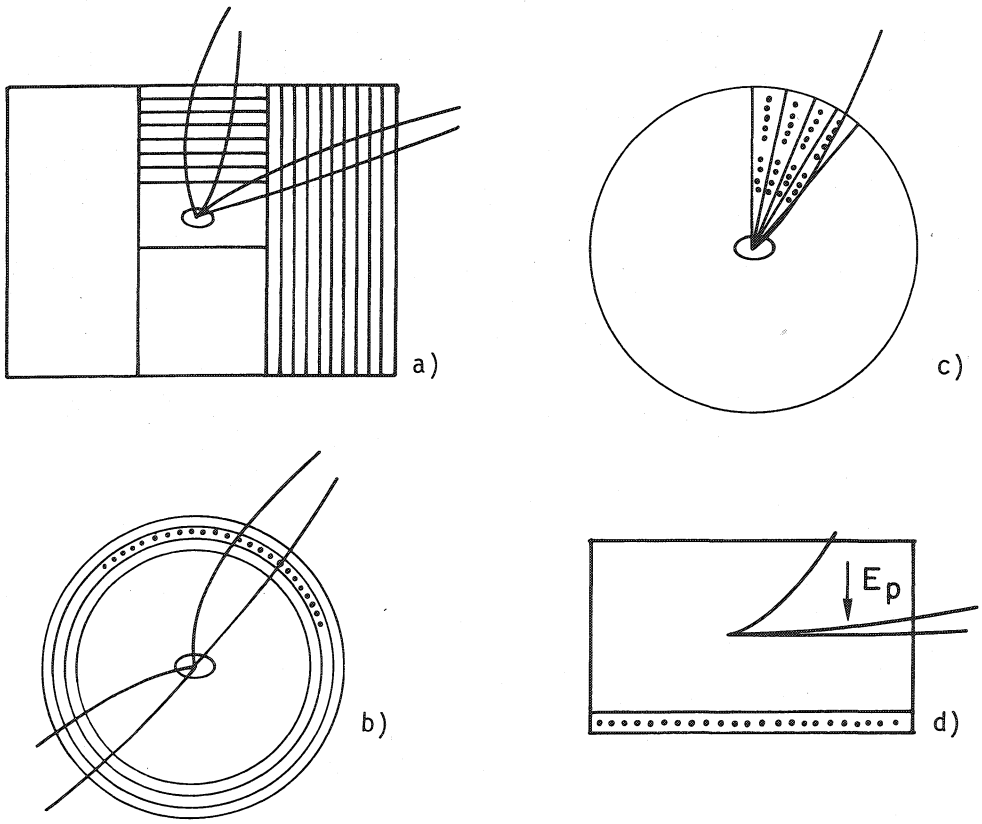
a)
c)
b)
E_p
d)

Fig. 8

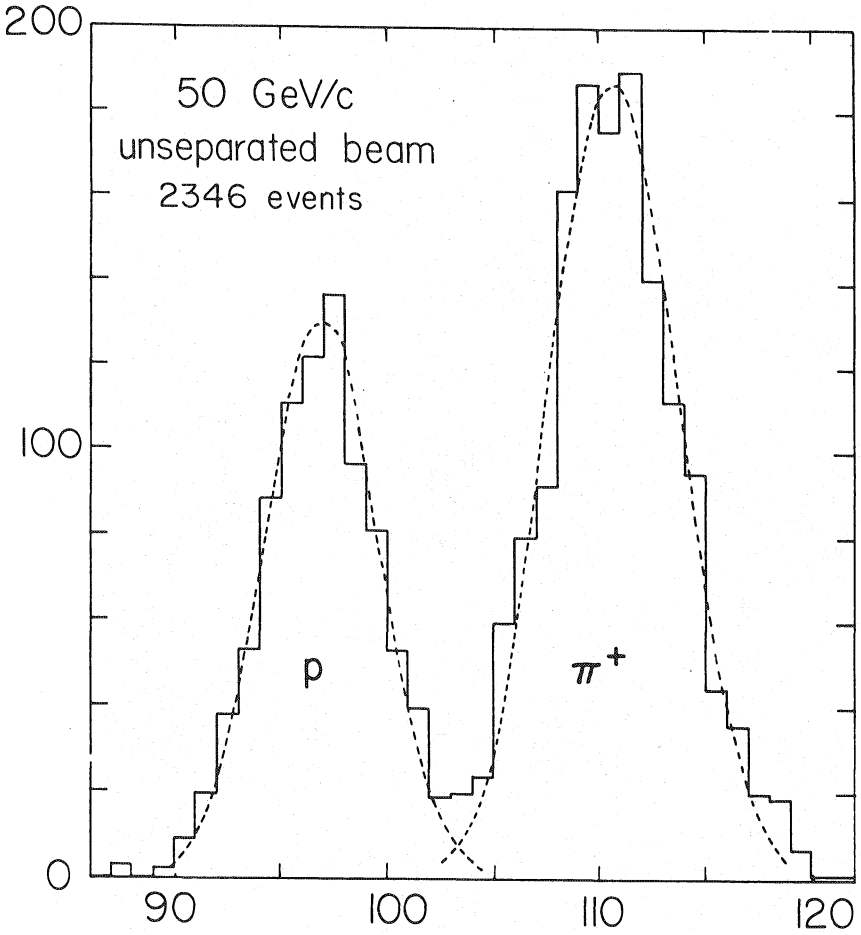

Fig. 9

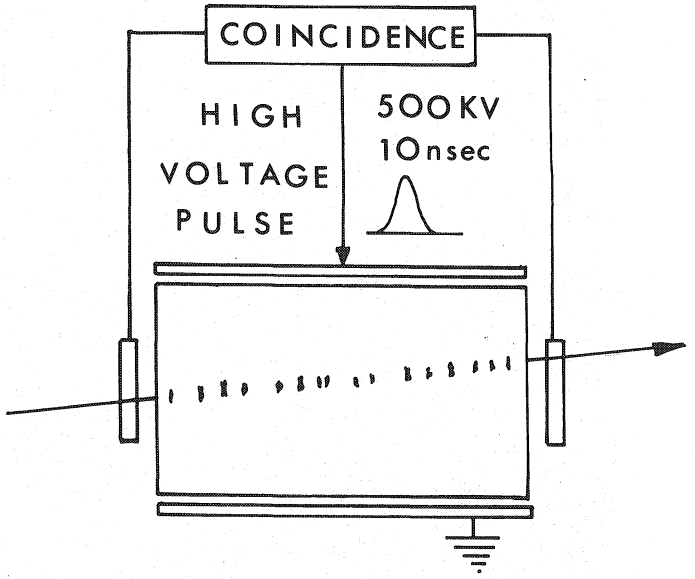

VIEW NORMAL TO E-FIELD

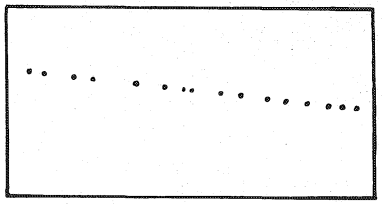

VIEW PARALLEL TO E-FIELD

Fig. 10

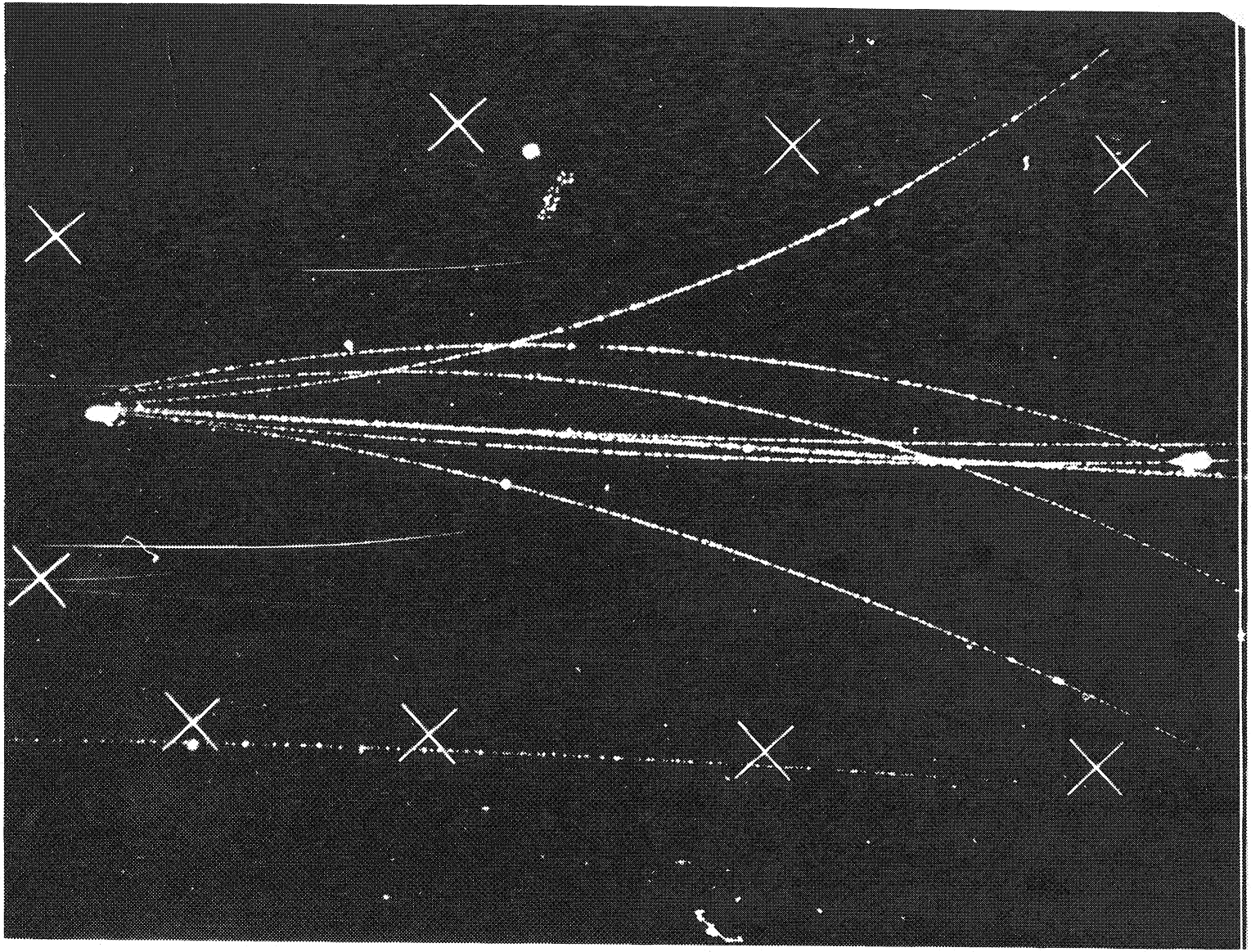

Fig. 11

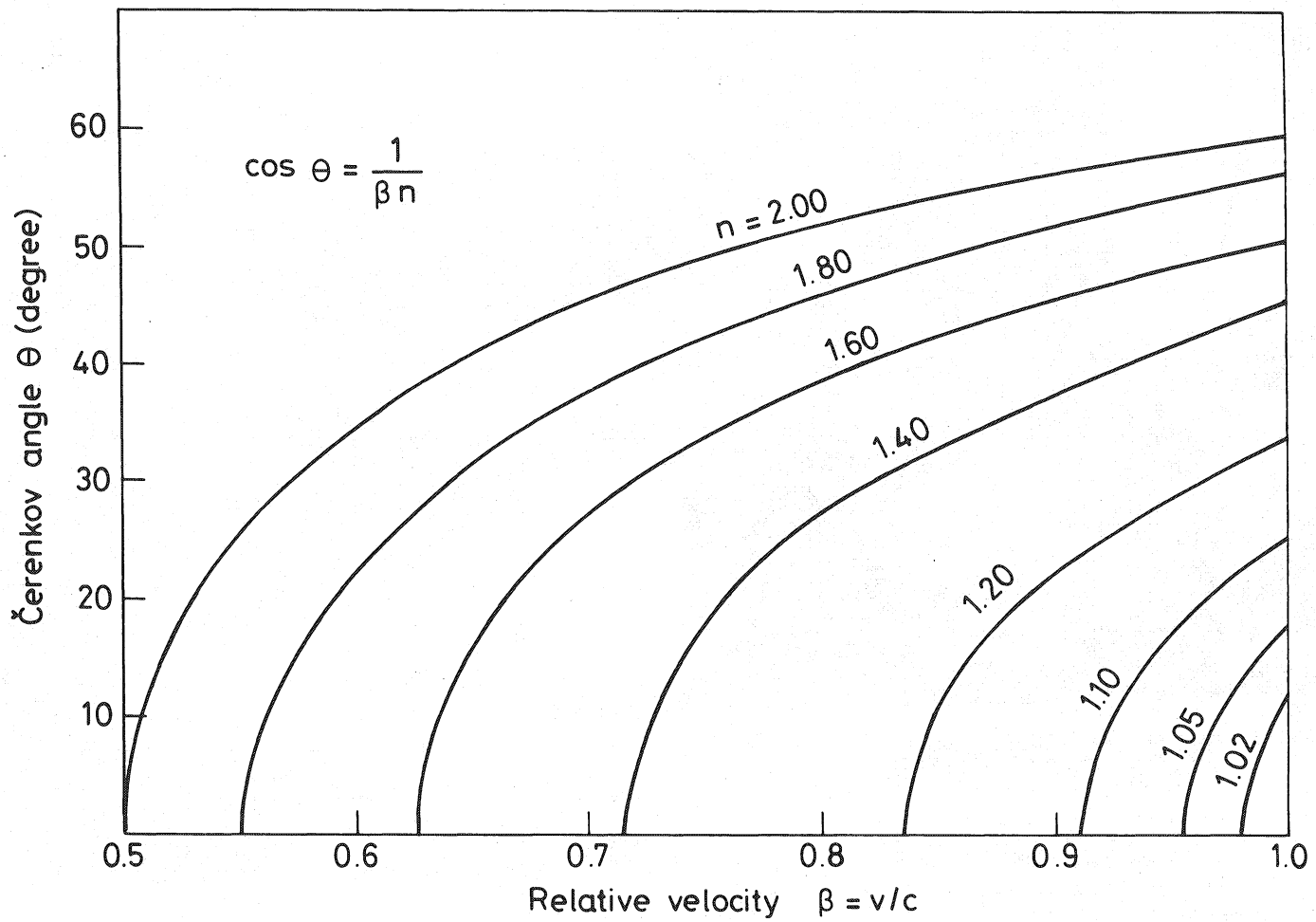
cos θ = 1/βn
n = 2.00
1.80
1.60
1.40
1.20
1.10
1.05
1.02
Čerenkov angle θ (degree)
60
50
40
30
20
10
0.5
0.6
0.7
0.8
0.9
1.0
Relative velocity β = v/c

Fig. 12

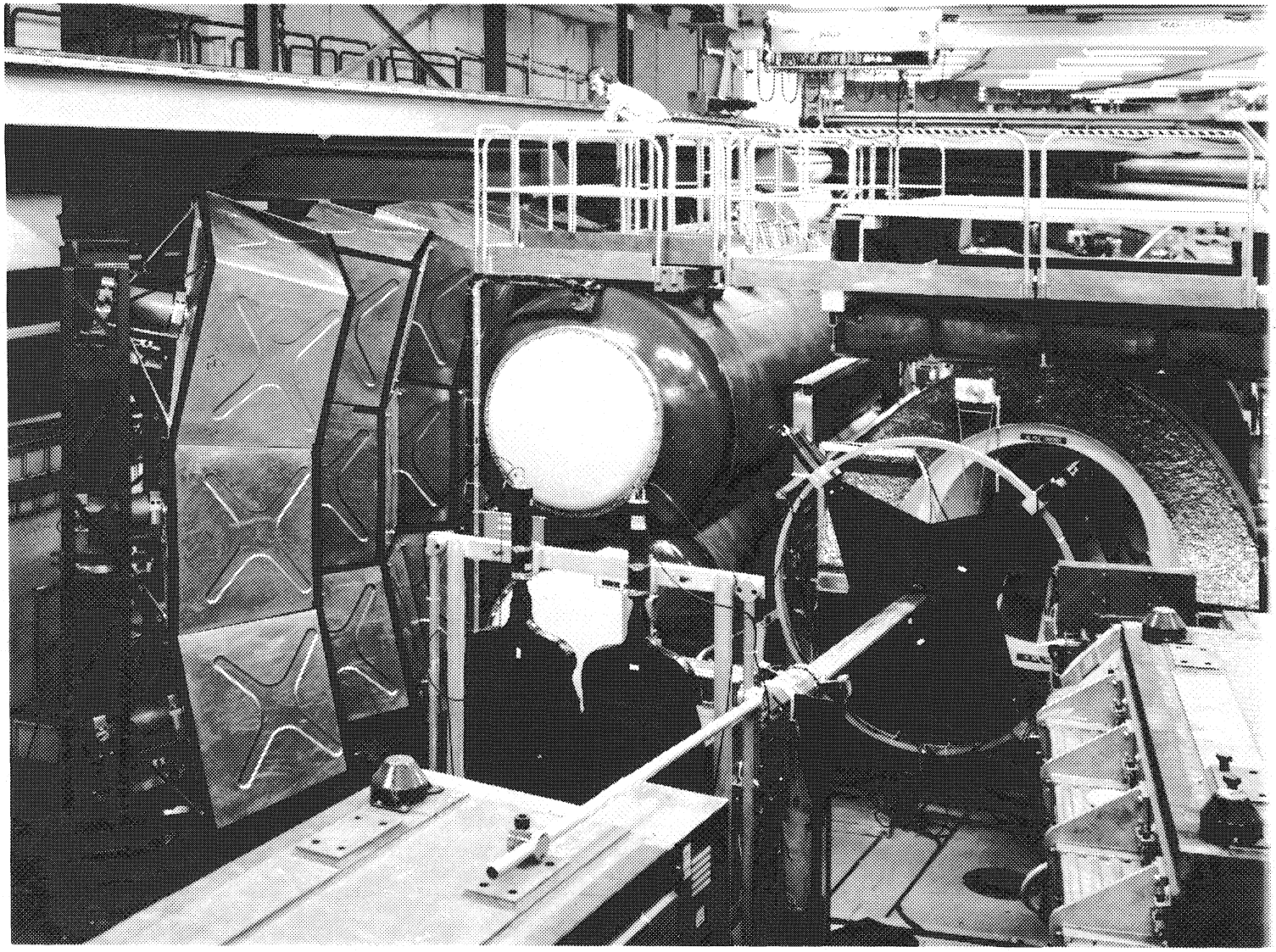

Fig. 13

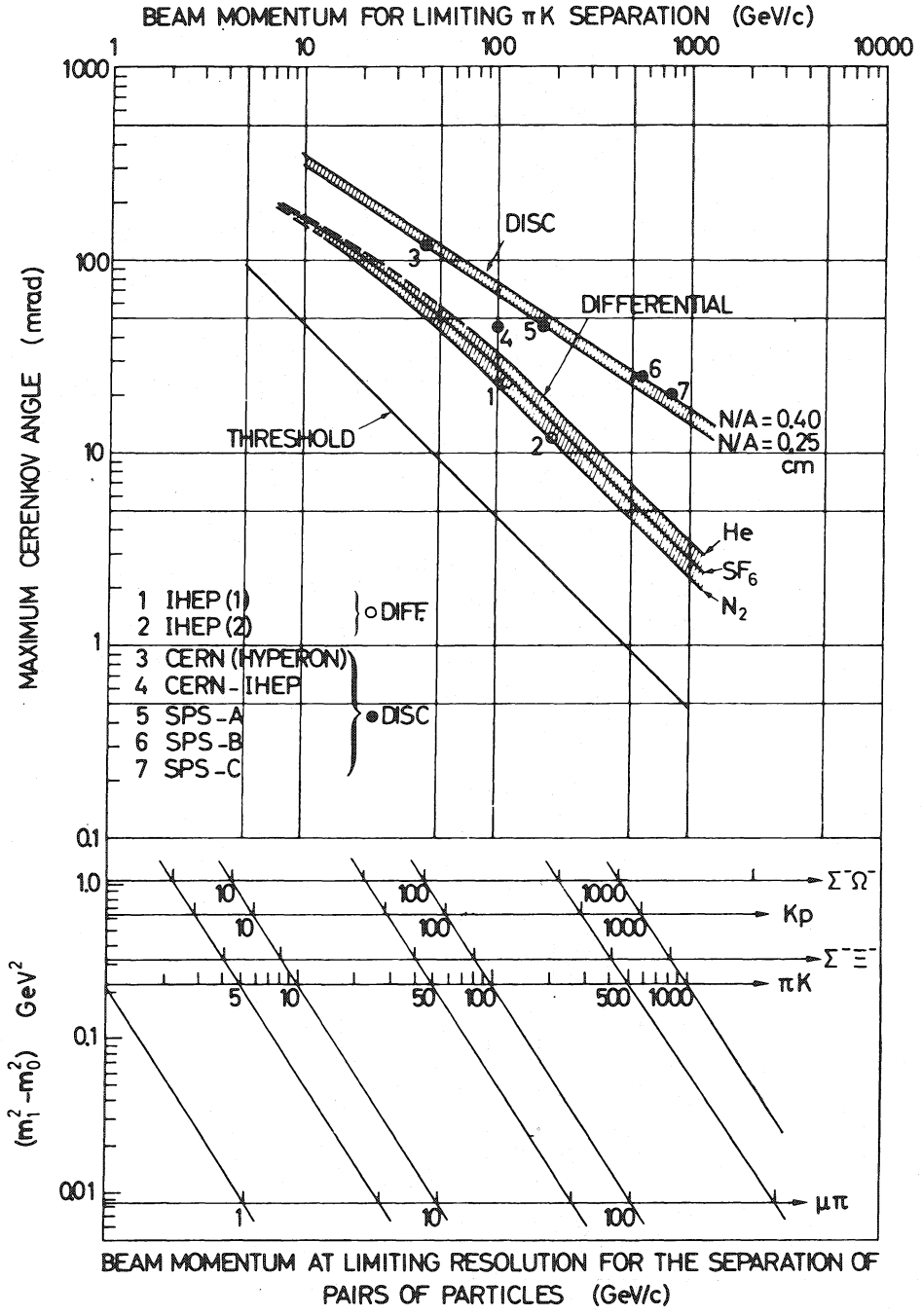
BEAM MOMENTUM FOR LIMITING πK SEPARATION (GeV/c)
1
10
100
1000
10000
1000
100
10
1
0.1
MAXIMUM CERENKOV ANGLE (mrad)
DISC
DIFFERENTIAL
THRESHOLD
N/A = 0.40
N/A = 0.25
cm
He
SF6
N2
1 IHEP (1)
2 IHEP (2)
3 CERN (HYPERON)
4 CERN - IHEP
5 SPS - A
6 SPS - B
7 SPS - C
o DIFF.
• DISC
1.0
0.1
0.01
(m1² - m0²) GeV²
Σ⁻Ω⁻
Kp
Σ⁻Ξ⁻
πK
μπ
BEAM MOMENTUM AT LIMITING RESOLUTION FOR THE SEPARATION OF PAIRS OF PARTICLES (GeV/c)

Fig. 14

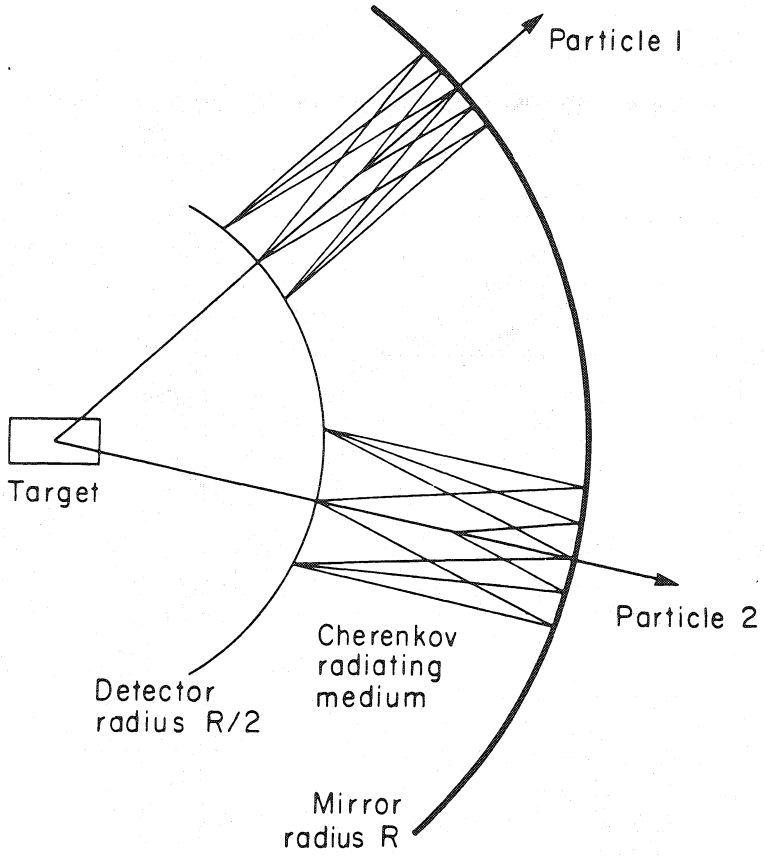
Particle 1
Target
Particle 2
Cherenkov
radiating
medium
Detector
radius R/2
Mirror
radius R

Fig. 15

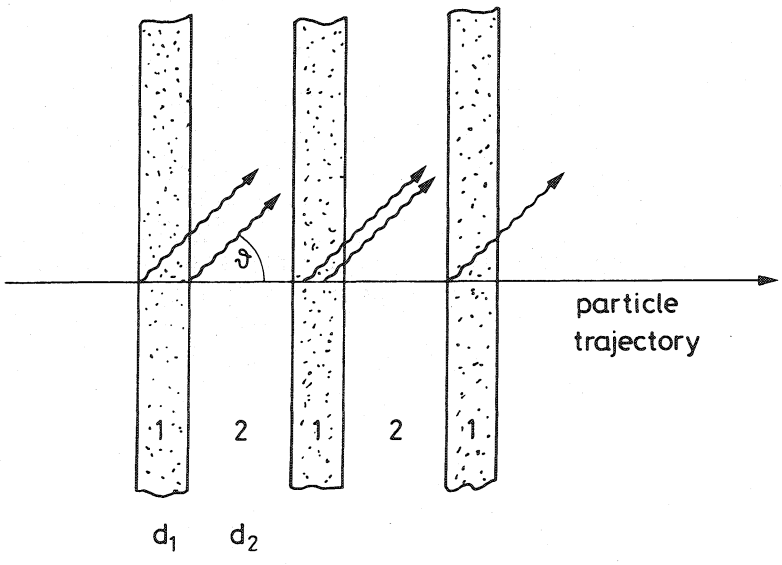
ϑ
particle
trajectory
1
2
1
2
1
d_1
d_2

Fig. 16

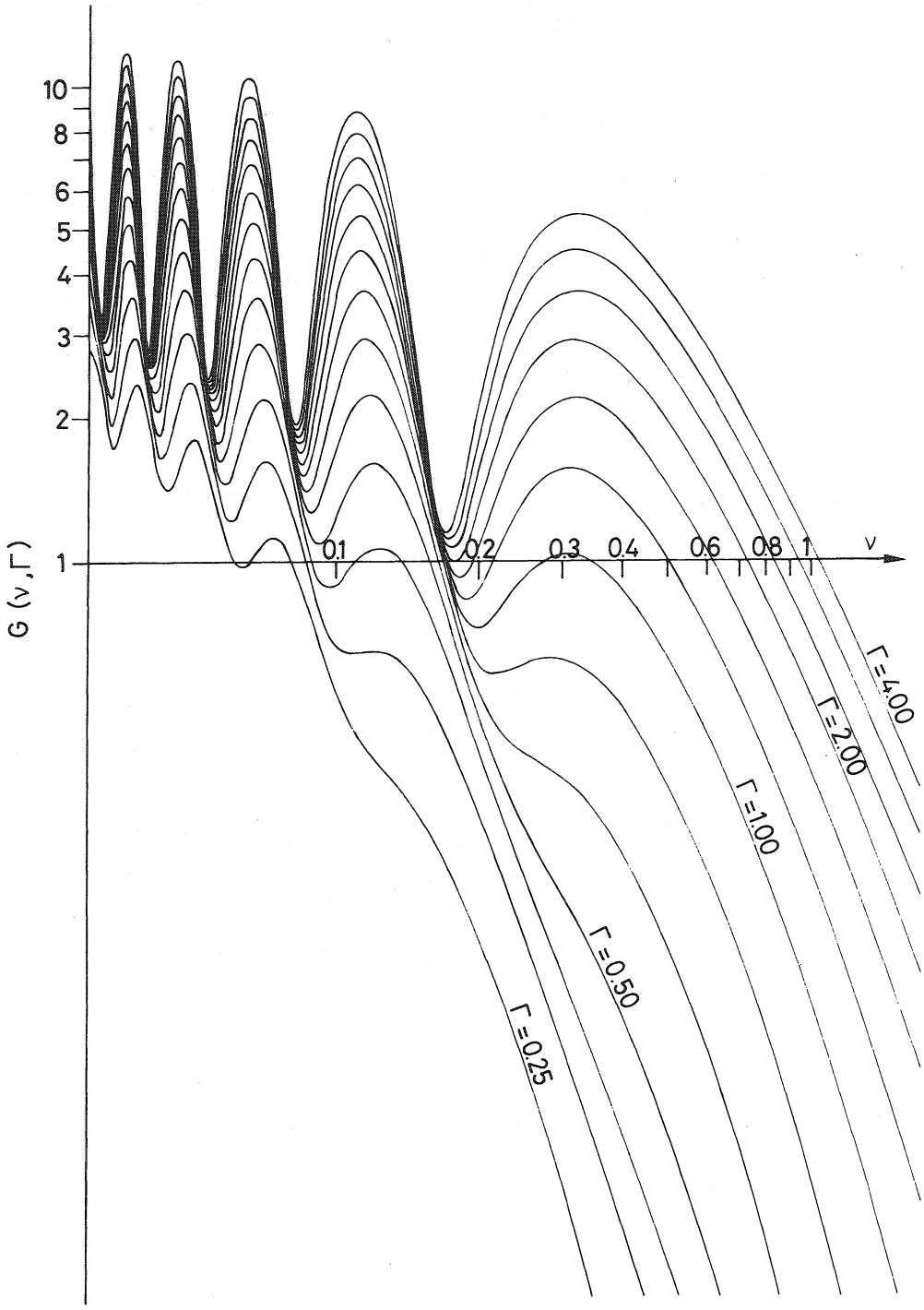

Fig. 17

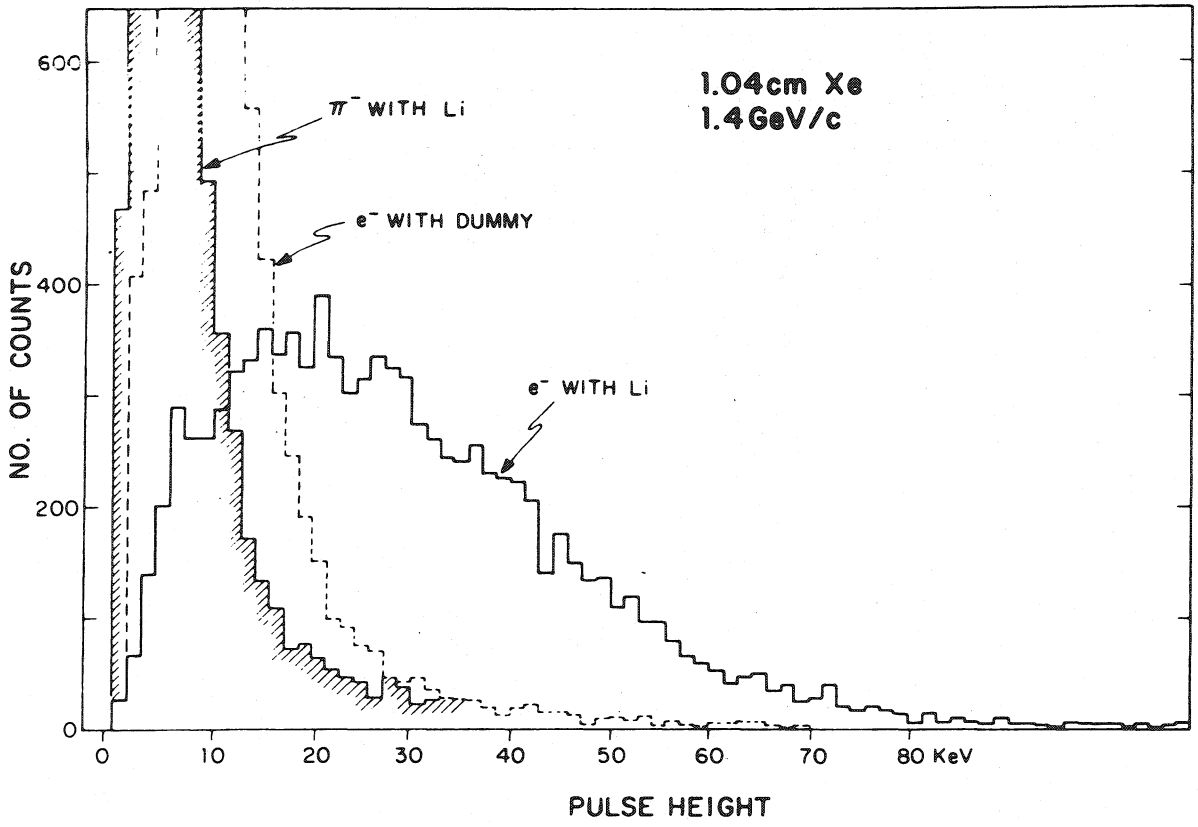
1.04cm Xe
1.4GeV/c
π⁻ WITH Li
e⁻ WITH DUMMY
e⁻ WITH Li
NO. OF COUNTS
600
400
200
0
0
10
20
30
40
50
60
70
80 KeV
PULSE HEIGHT

Fig. 18

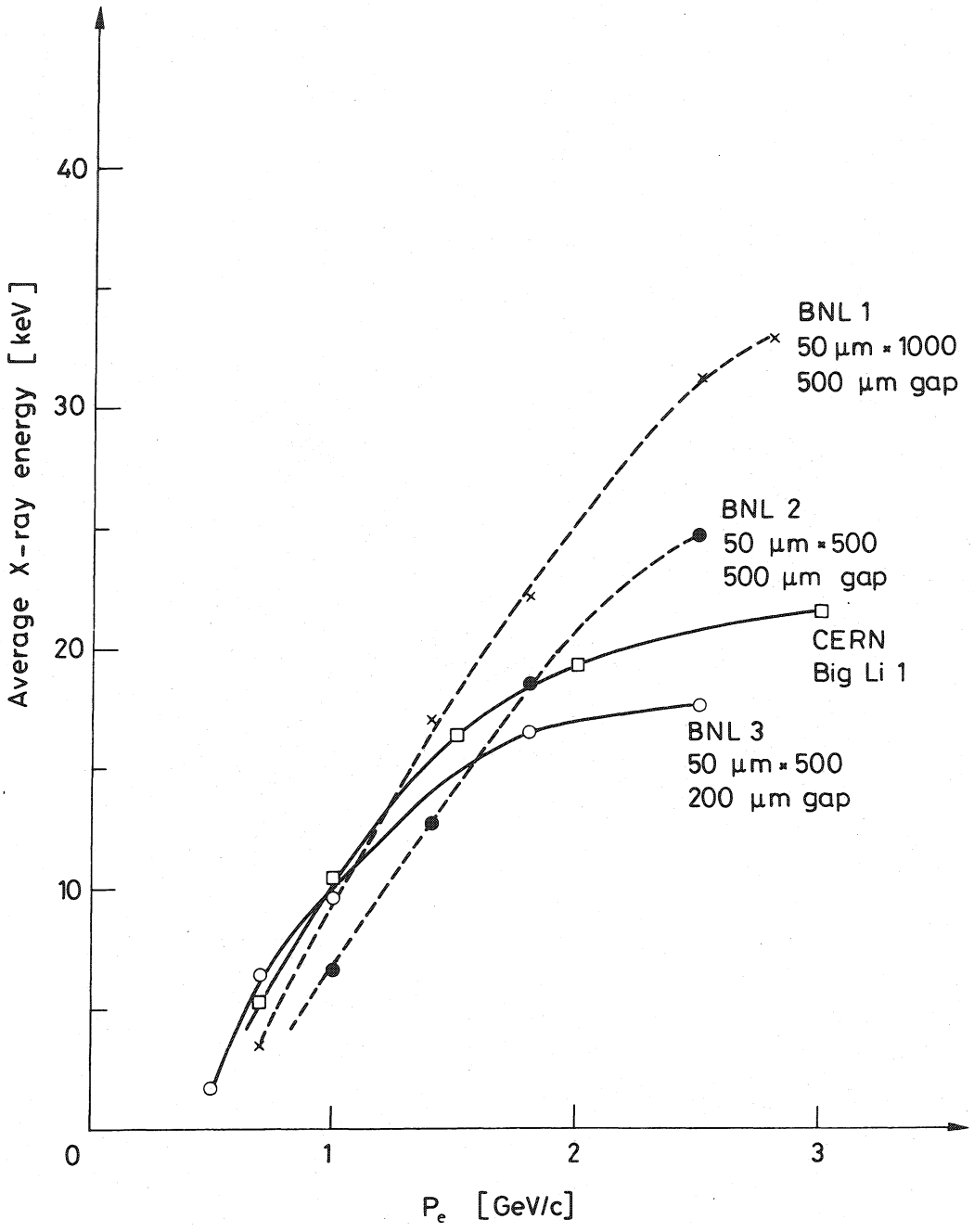
Average X-ray energy [keV]
40
30
20
10
0
1
2
3
P_e [GeV/c]
BNL 1
50 µm × 1000
500 µm gap
BNL 2
50 µm × 500
500 µm gap
CERN
Big Li 1
BNL 3
50 µm × 500
200 µm gap

Fig. 19

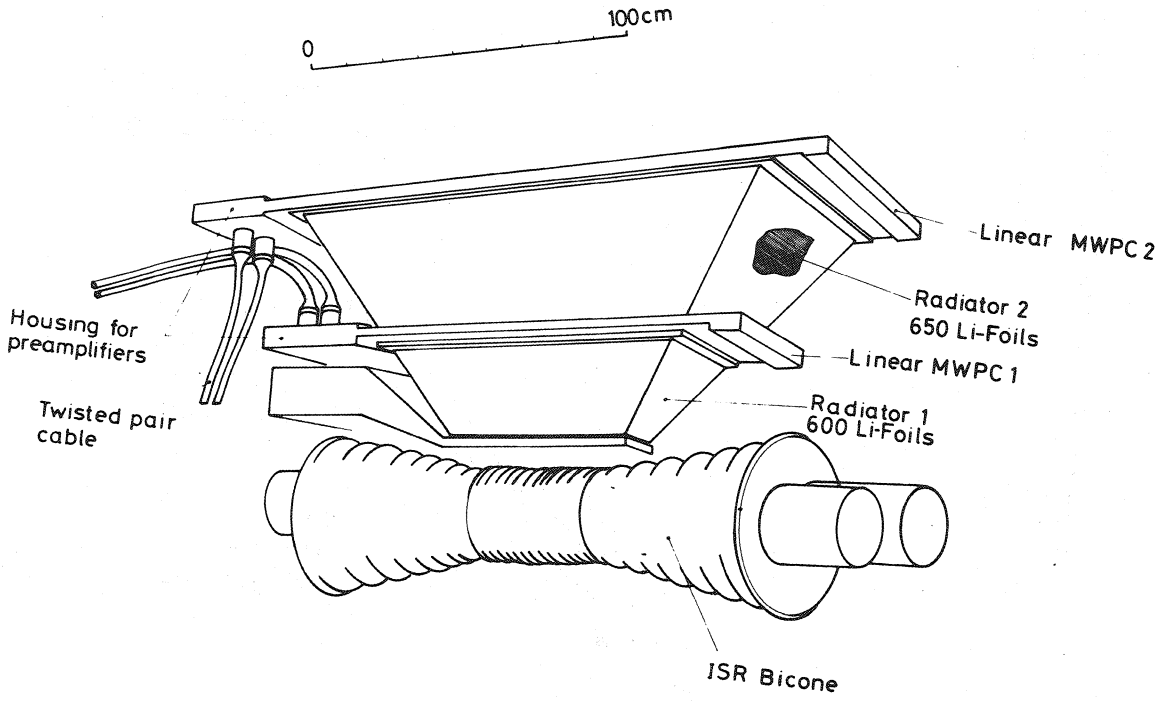
0
100cm
Linear MWPC 2
Radiator 2
650 Li-Foils
Linear MWPC 1
Radiator 1
600 Li-Foils
Housing for
preamplifiers
Twisted pair
cable
ISR Bicone

Fig. 20

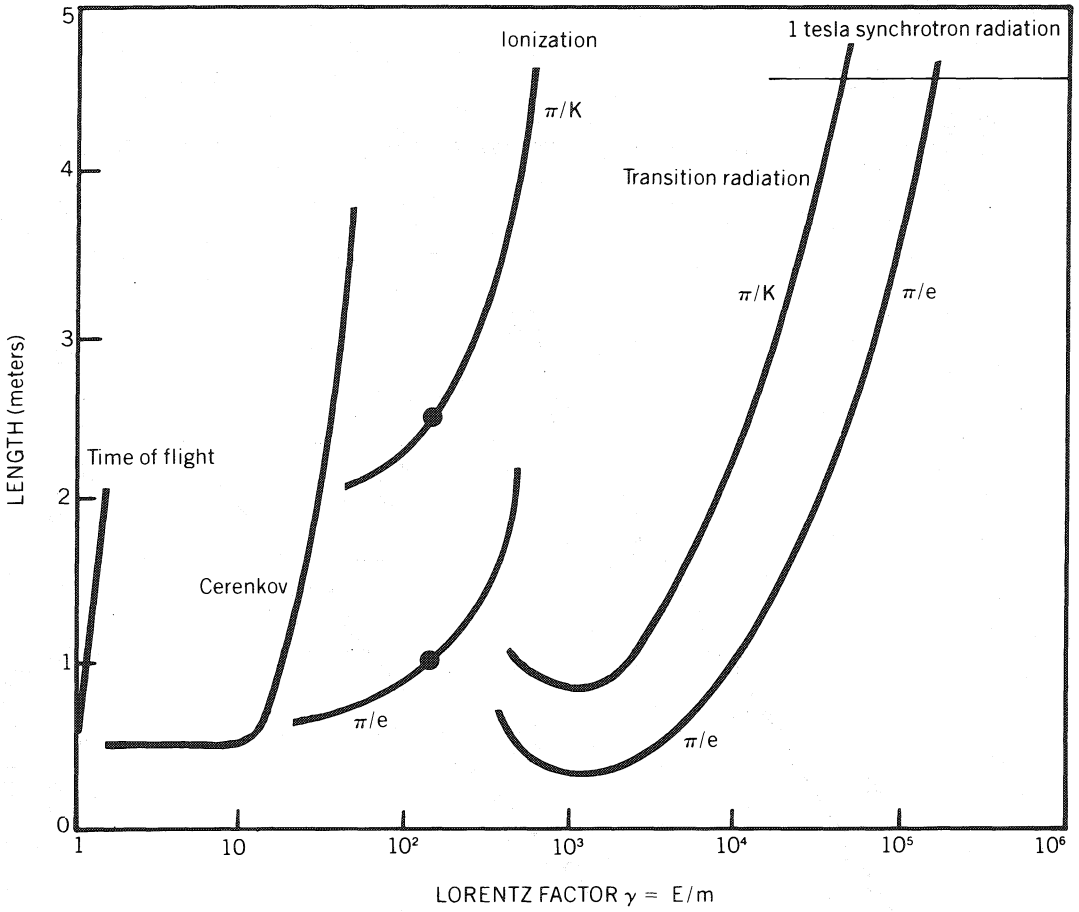
LENGTH (meters)
5
4
3
2
1
0
Ionization
1 tesla synchrotron radiation
π/K
Transition radiation
π/K
π/e
Time of flight
Cerenkov
π/e
π/e
1
10
10²
10³
10⁴
10⁵
10⁶
LORENTZ FACTOR γ = E/m

Fig. 21

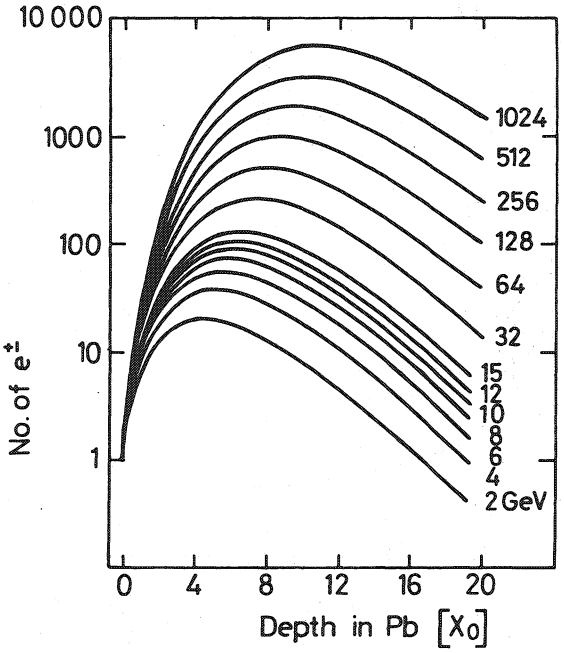
10 000
1000
100
10
1
No. of e±
1024
512
256
128
64
32
15
12
10
8
6
4
2 GeV
0
4
8
12
16
20
Depth in Pb [X0]

Fig. 22

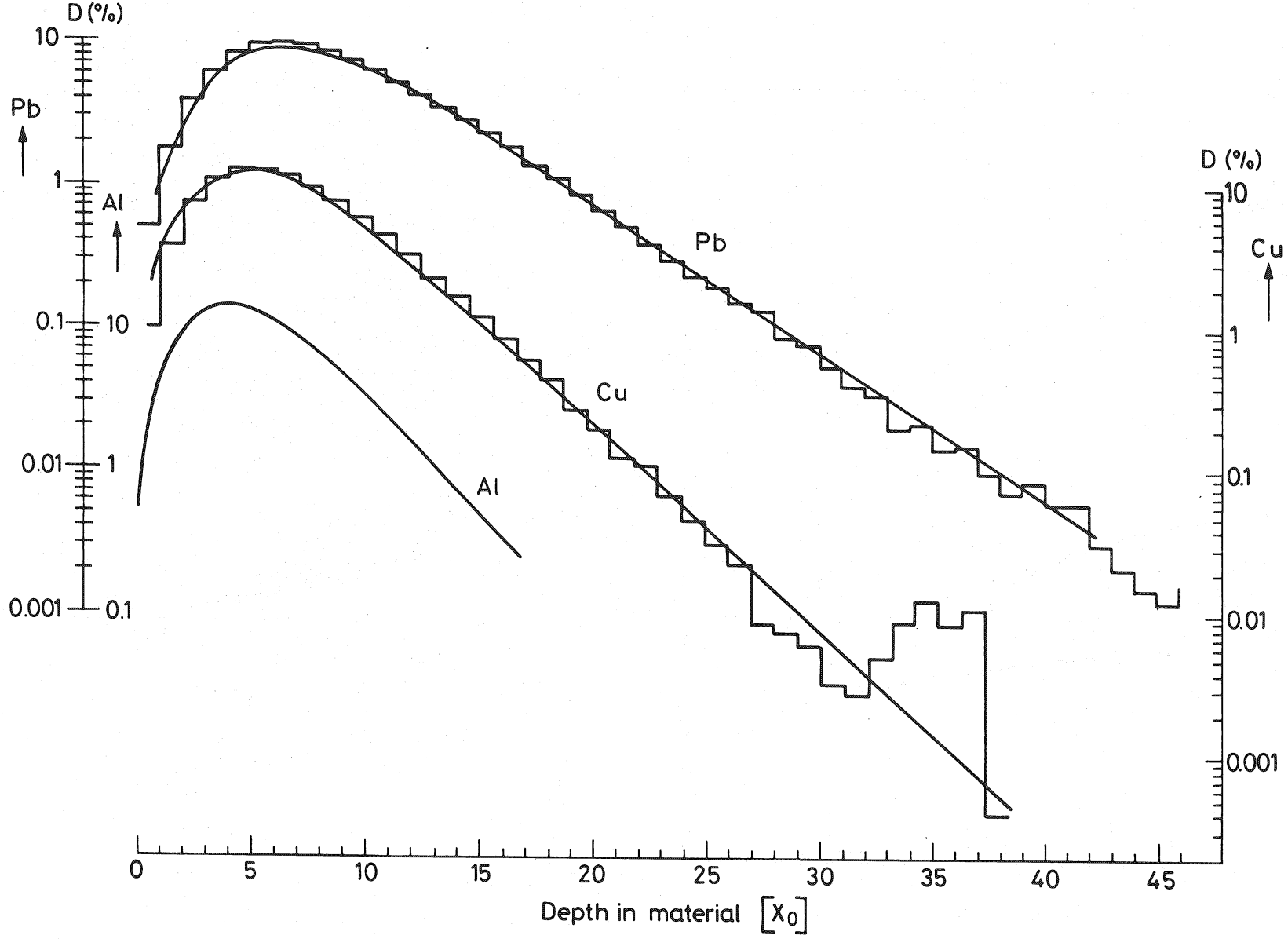
D (%)
10
Pb
1
Al
0.1
10
0.01
1
0.001
0.1
Pb
Cu
Al
D (%)
10
Cu
1
0.1
0.01
0.001
0
5
10
15
20
25
30
35
40
45
Depth in material [X0]

Fig. 23

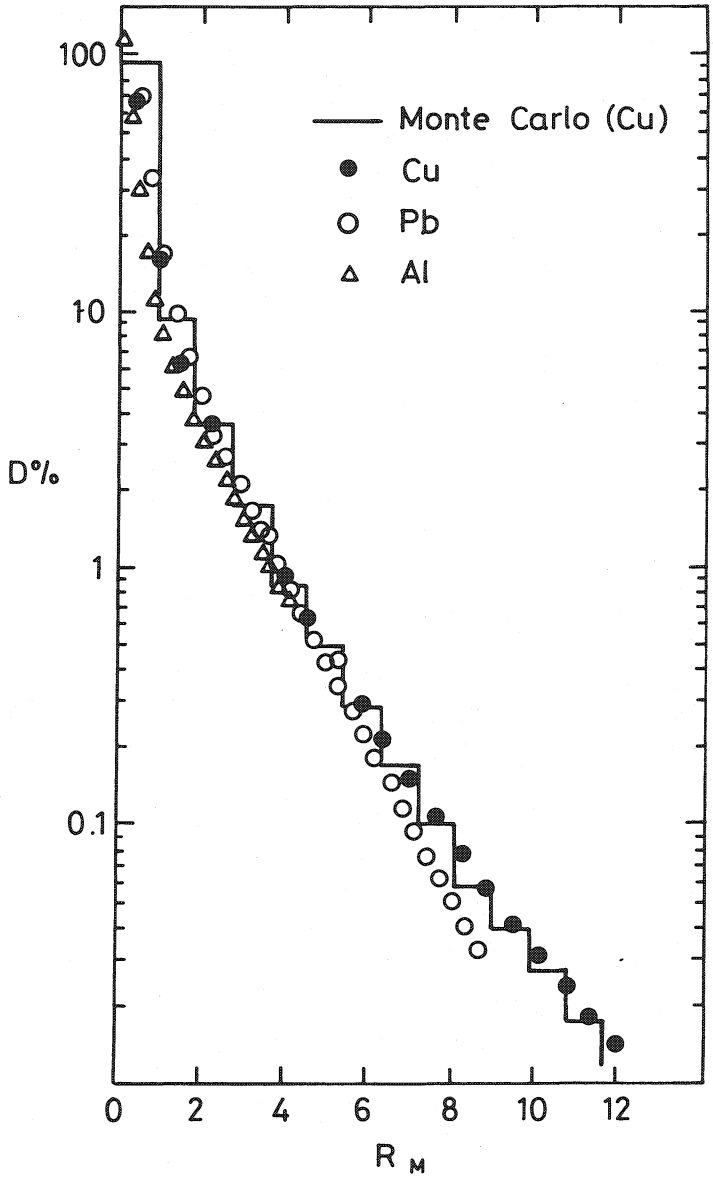

Fig. 24

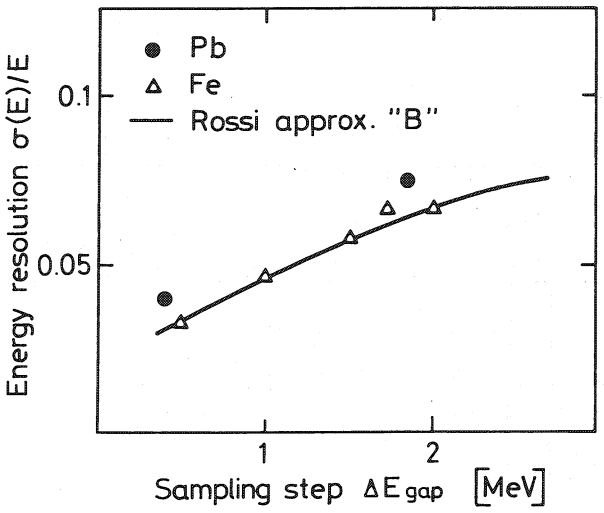
Pb
Fe
Rossi approx. "B"
Energy resolution σ(E)/E
0.1
0.05
1
2
Sampling step ΔE gap [MeV]

Fig. 25

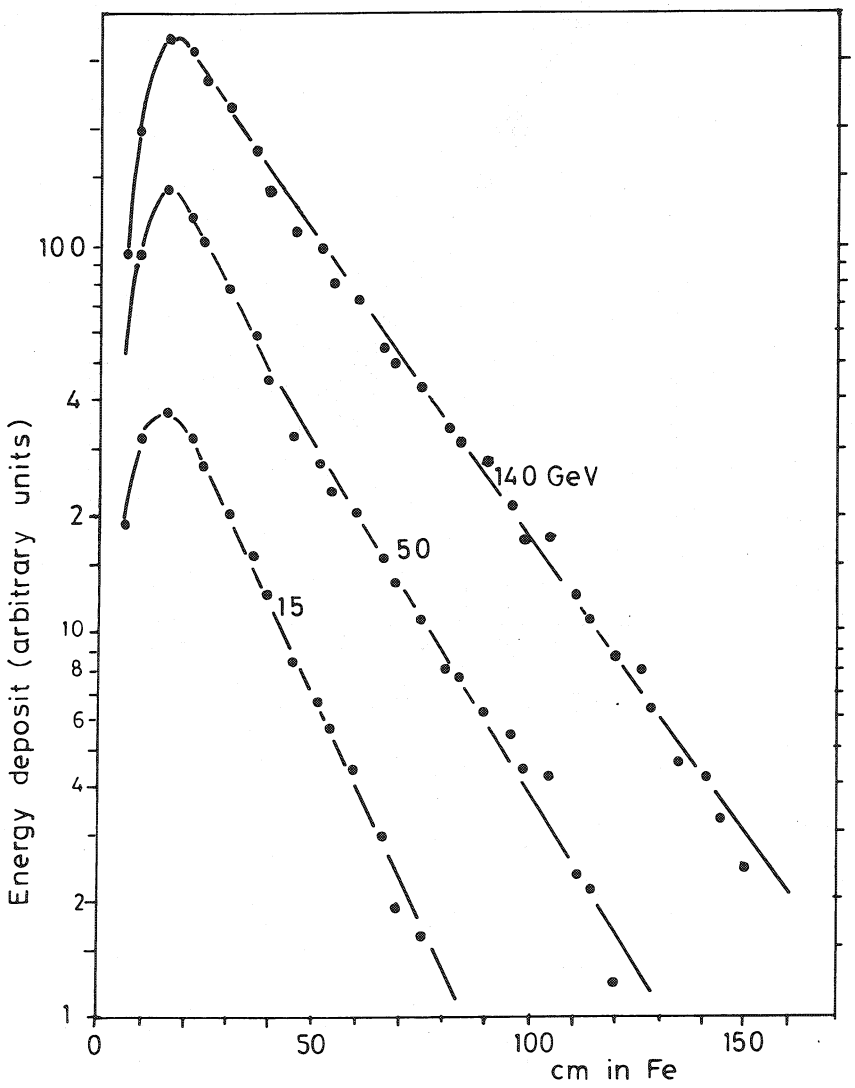
Energy deposit (arbitrary units)
100
4
2
10
8
6
4
2
1
140 GeV
50
15
0
50
100
150
cm in Fe

Fig. 26

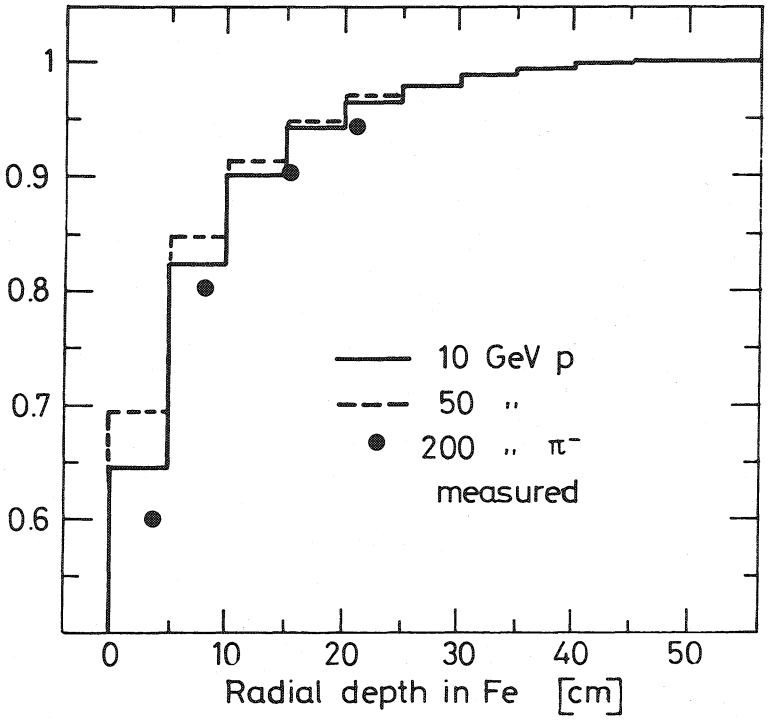
1
0.9
0.8
0.7
0.6
0
10
20
30
40
50
Radial depth in Fe [cm]
10 GeV p
50 ,,
200 ,, π⁻
measured

Fig. 27

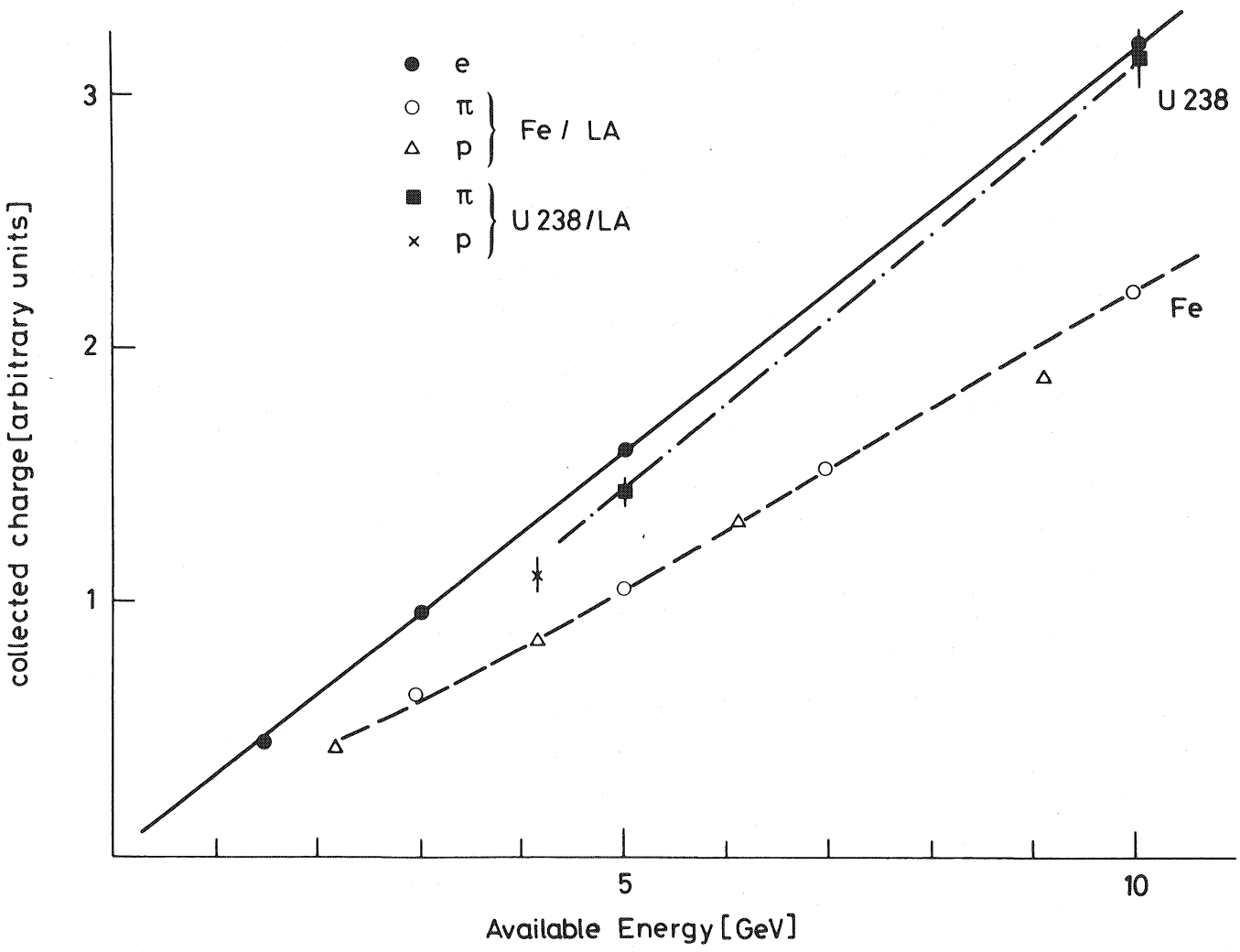
e
π
p
Fe / LA
π
p
U 238/LA
U 238
Fe
collected charge [arbitrary units]
3
2
1
5
10
Available Energy [GeV]

Fig. 28

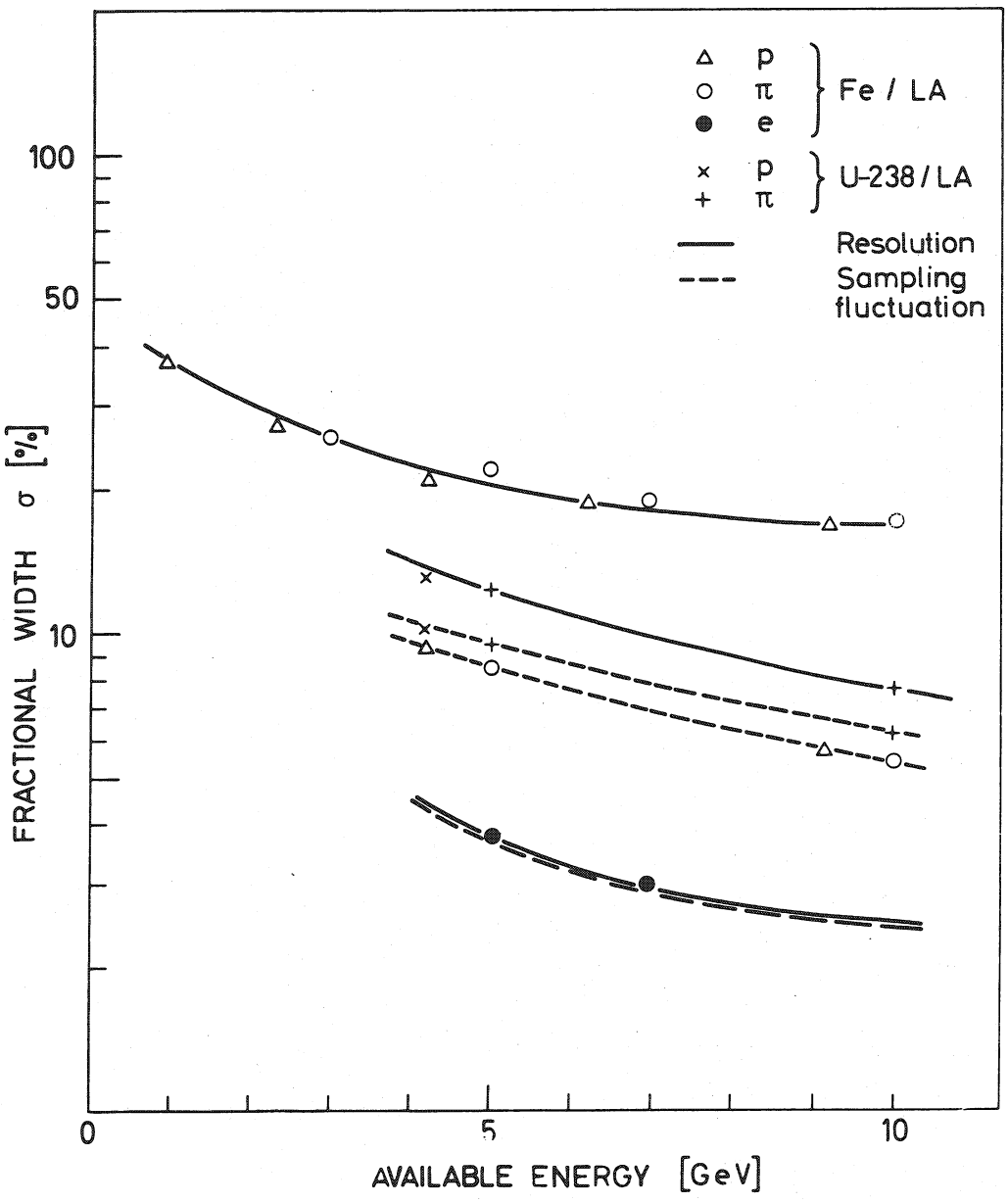
p
π
e
Fe / LA
p
π
U-238 / LA
Resolution
Sampling fluctuation
100
50
10
FRACTIONAL WIDTH σ [%]
0
5
10
AVAILABLE ENERGY [GeV]

Fig. 29

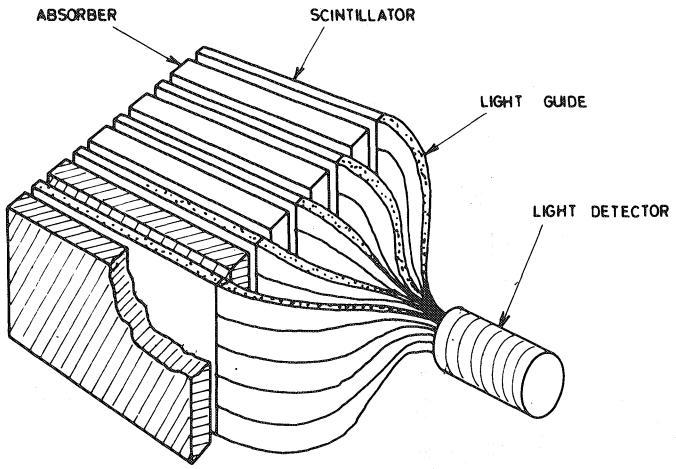
ABSORBER
SCINTILLATOR
LIGHT GUIDE
LIGHT DETECTOR

a)

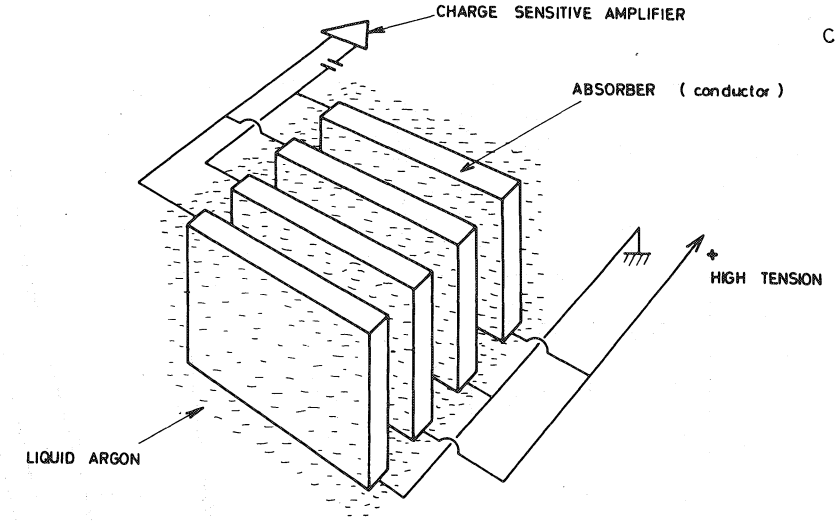
CHARGE SENSITIVE AMPLIFIER
ABSORBER (conductor)
HIGH TENSION
LIQUID ARGON

c)

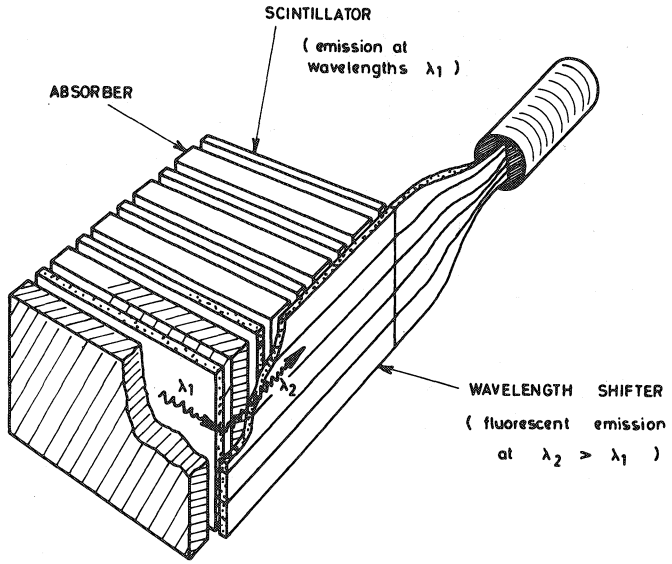
SCINTILLATOR
(emission at
wavelengths λ_1)
ABSORBER
λ_1
λ_2
WAVELENGTH SHIFTER
(fluorescent emission
at $\lambda_2 > \lambda_1$)

b)

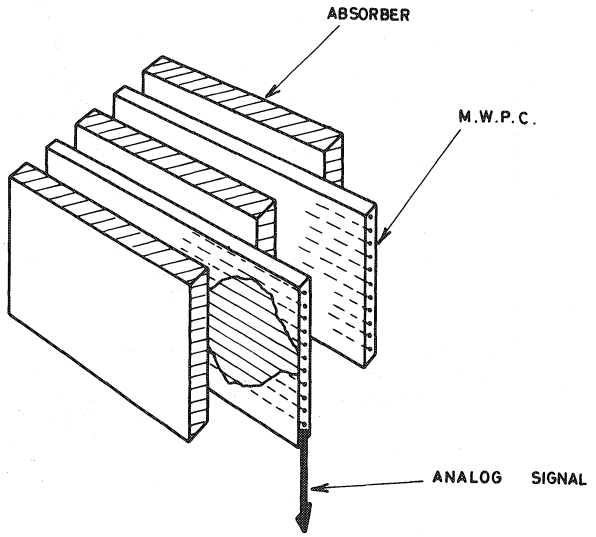
ABSORBER
M.W.P.C.
ANALOG SIGNAL

d)

Fig. 30

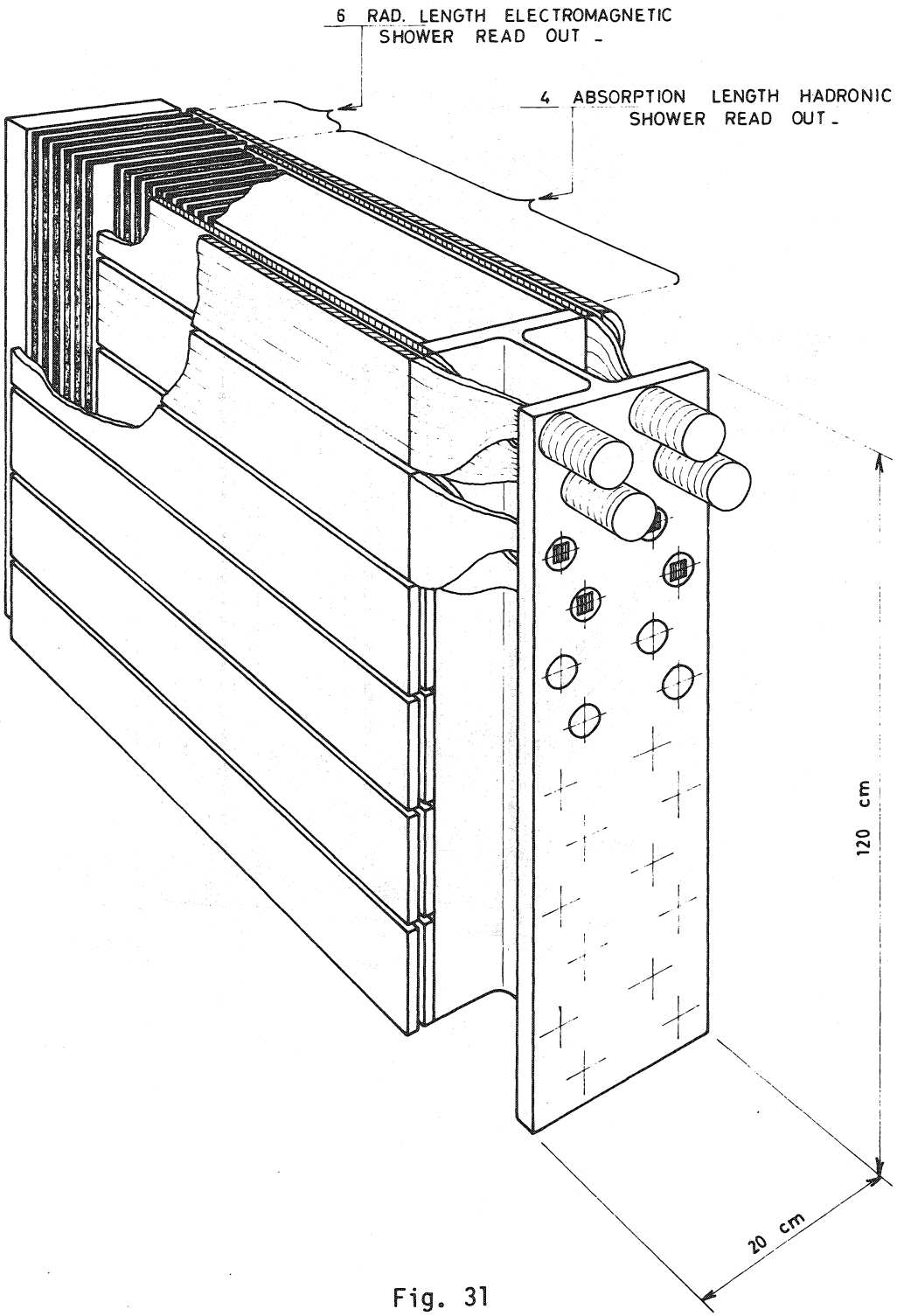
6 RAD. LENGTH ELECTROMAGNETIC
SHOWER READ OUT -
4 ABSORPTION LENGTH HADRONIC
SHOWER READ OUT -
120 cm
20 cm

Fig. 31

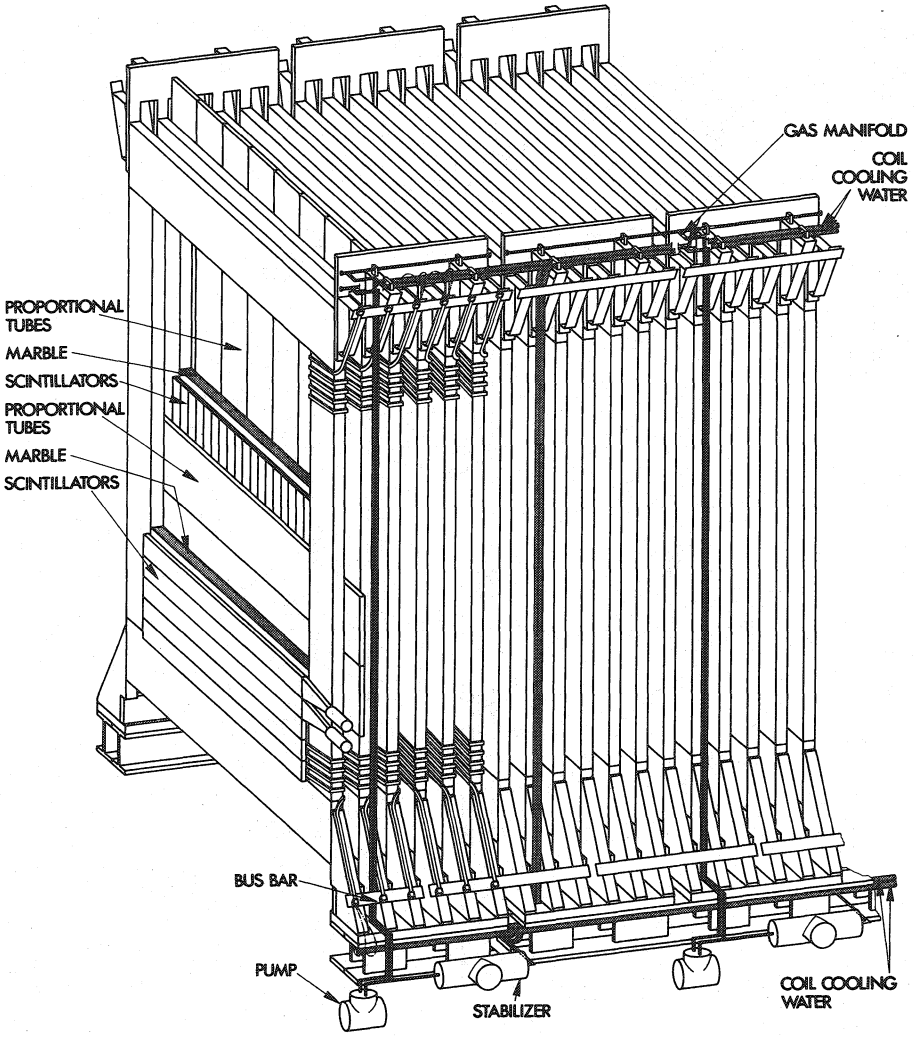
GAS MANIFOLD
COIL COOLING WATER
PROPORTIONAL TUBES
MARBLE
SCINTILLATORS
PROPORTIONAL TUBES
MARBLE
SCINTILLATORS
BUS BAR
PUMP
STABILIZER
COIL COOLING WATER

Fig. 32

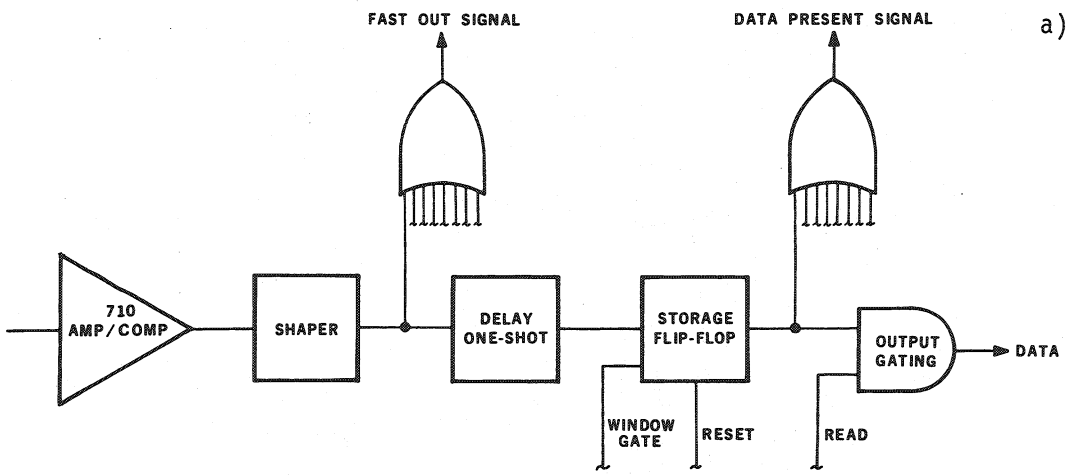
a)
FAST OUT SIGNAL
DATA PRESENT SIGNAL
710
AMP/COMP
SHAPER
DELAY
ONE-SHOT
STORAGE
FLIP-FLOP
OUTPUT
GATING
DATA
WINDOW
GATE
RESET
READ

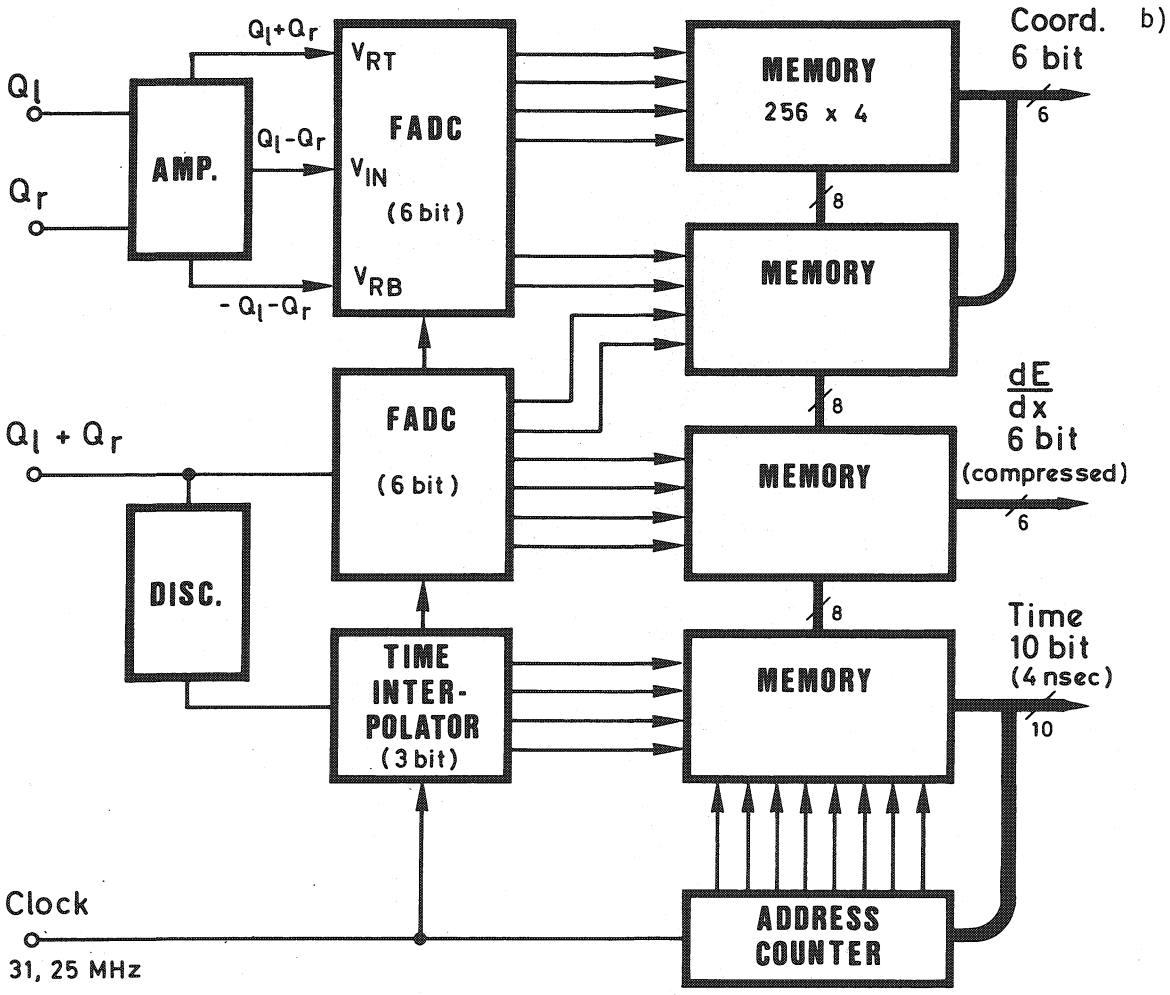
b)
Coord.
6 bit
Q_l
Q_r
AMP.
Q_l+Q_r
Q_l-Q_r
$-Q_l-Q_r$
V_{RT}
FADC
V_{IN}
(6 bit)
V_{RB}
MEMORY
256 x 4
MEMORY
FADC
(6 bit)
MEMORY
dE
dx
6 bit
(compressed)
$Q_l + Q_r$
DISC.
TIME
INTER-
POLATOR
(3 bit)
MEMORY
Time
10 bit
(4 nsec)
Clock
31, 25 MHz
ADDRESS
COUNTER

Fig. 33

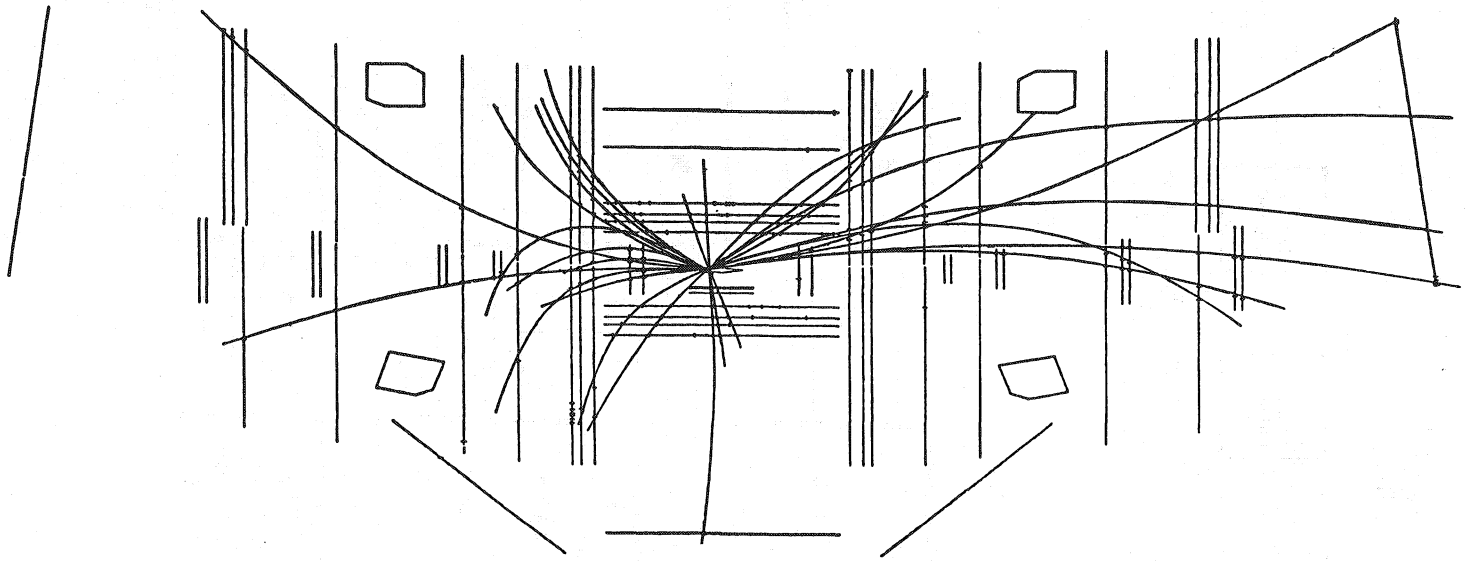

Fig. 34

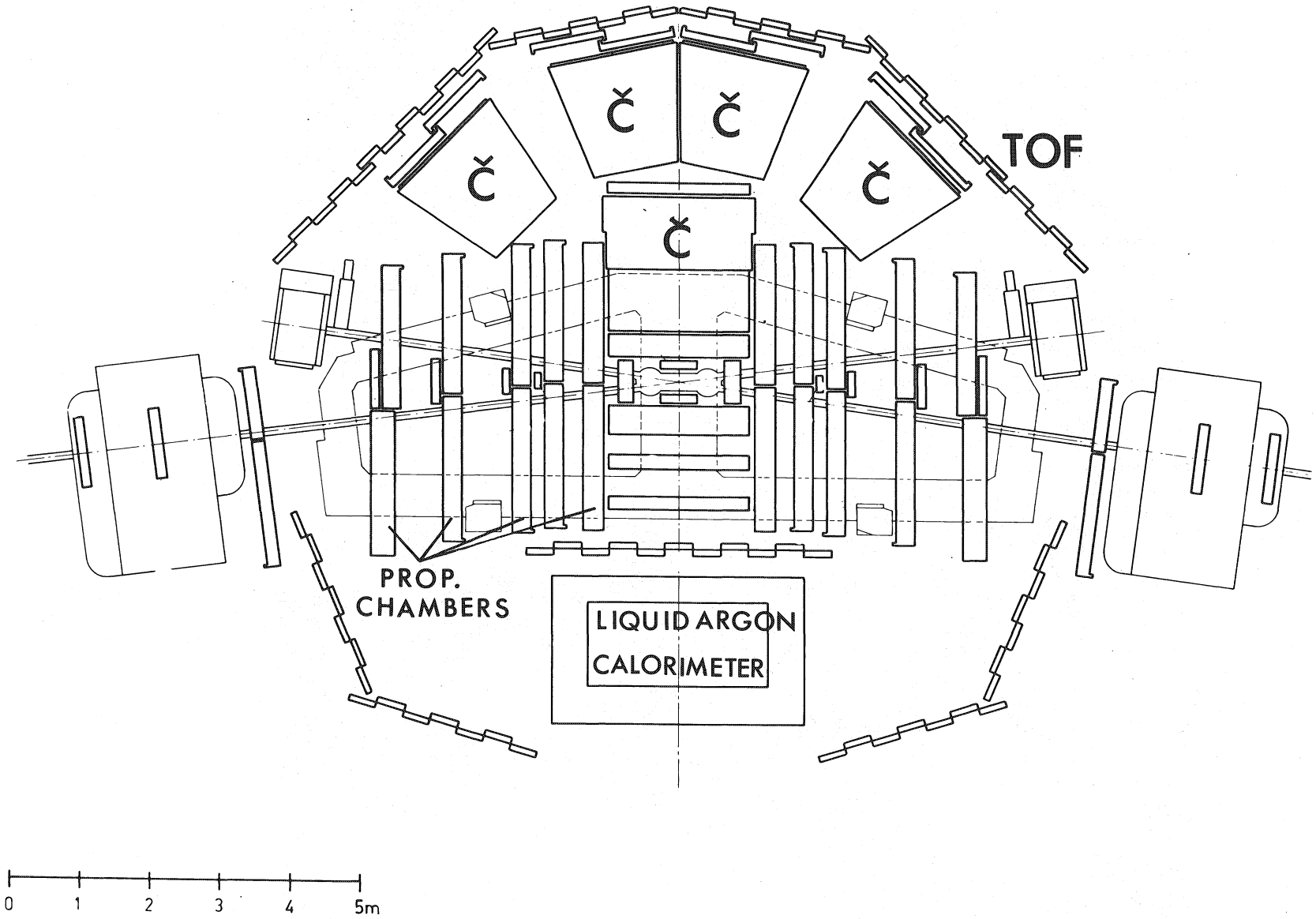

Fig. 35a

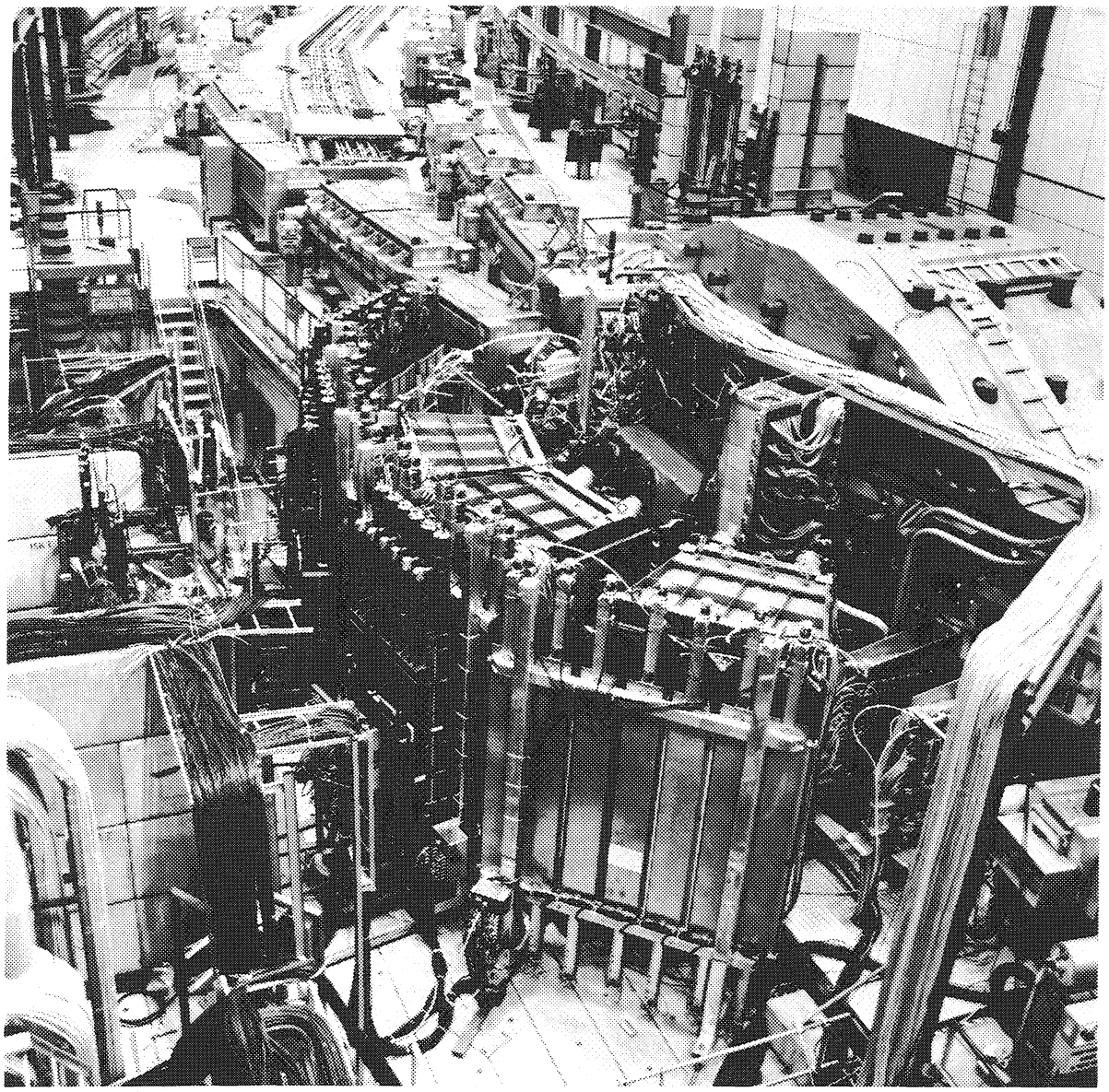

Fig. 35b

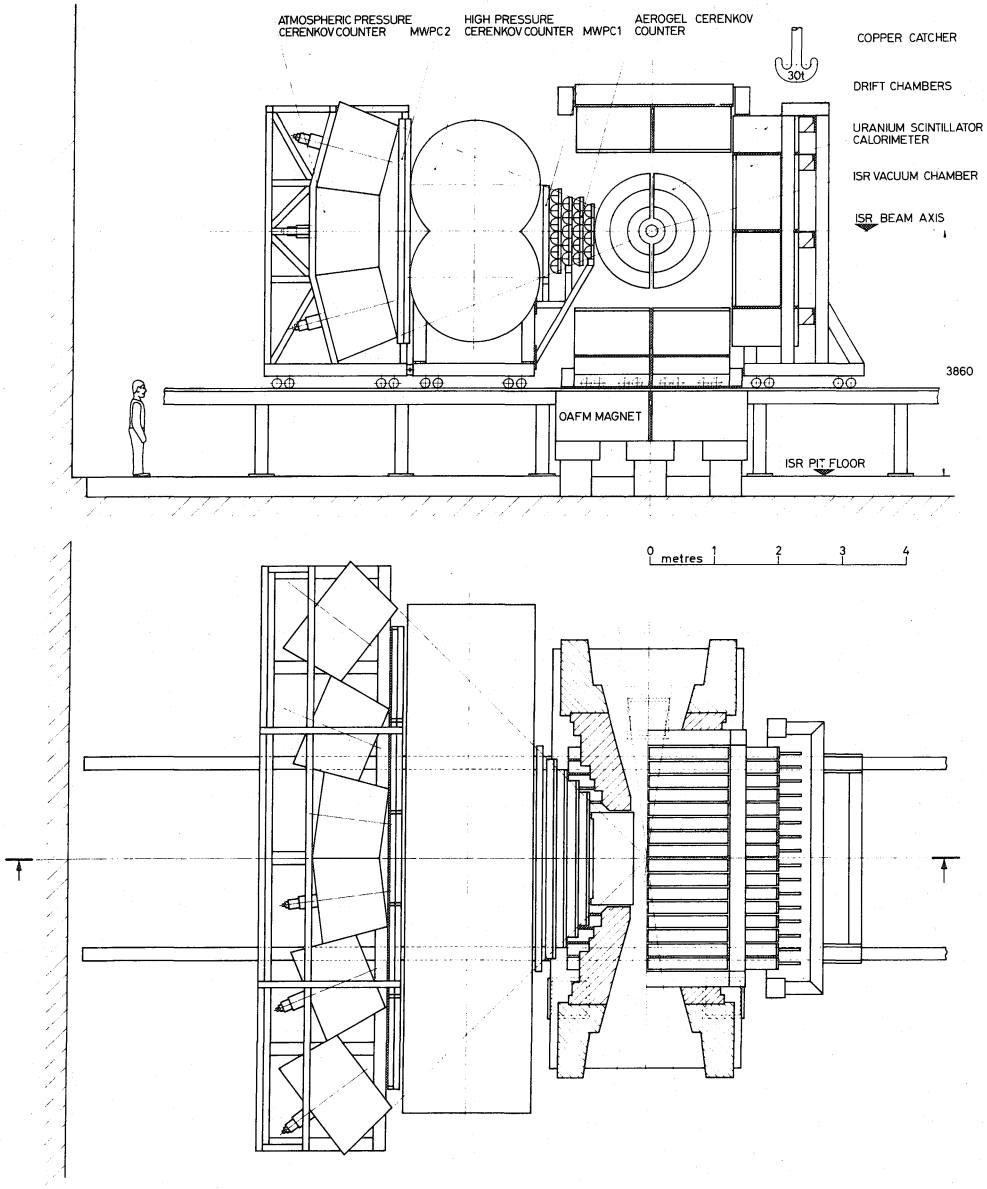
ATMOSPHERIC PRESSURE CERENKOV COUNTER
MWPC2
HIGH PRESSURE CERENKOV COUNTER
MWPC1
AEROGEL CERENKOV COUNTER
COPPER CATCHER
30t
DRIFT CHAMBERS
URANIUM SCINTILLATOR CALORIMETER
ISR VACUUM CHAMBER
ISR BEAM AXIS
3860
OAFM MAGNET
ISR PIT FLOOR
0 metres 1 2 3 4

Fig. 36

EXPERIMENTAL LAYOUT HORIZONTAL

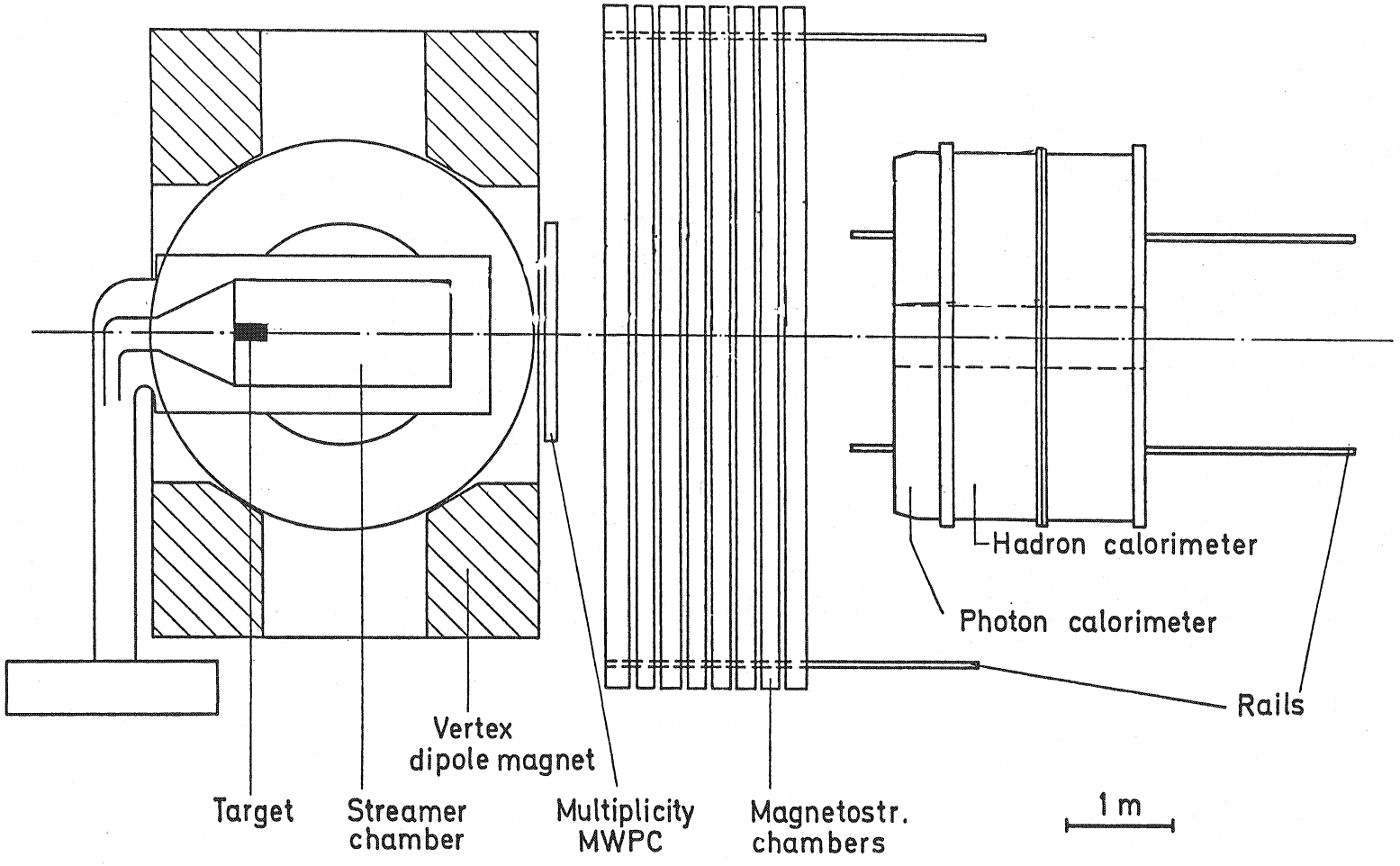

Fig. 37a

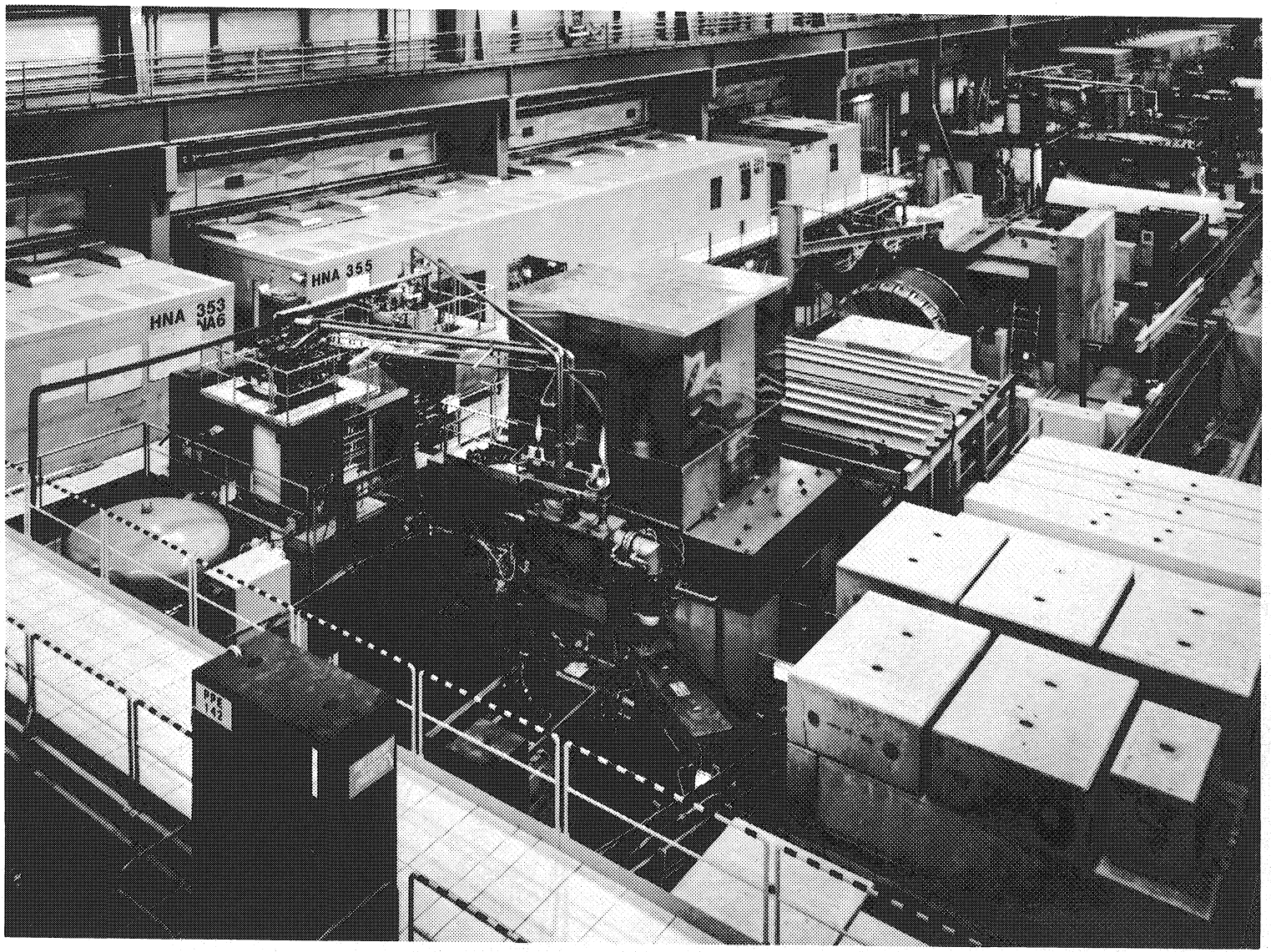

Fig. 37b

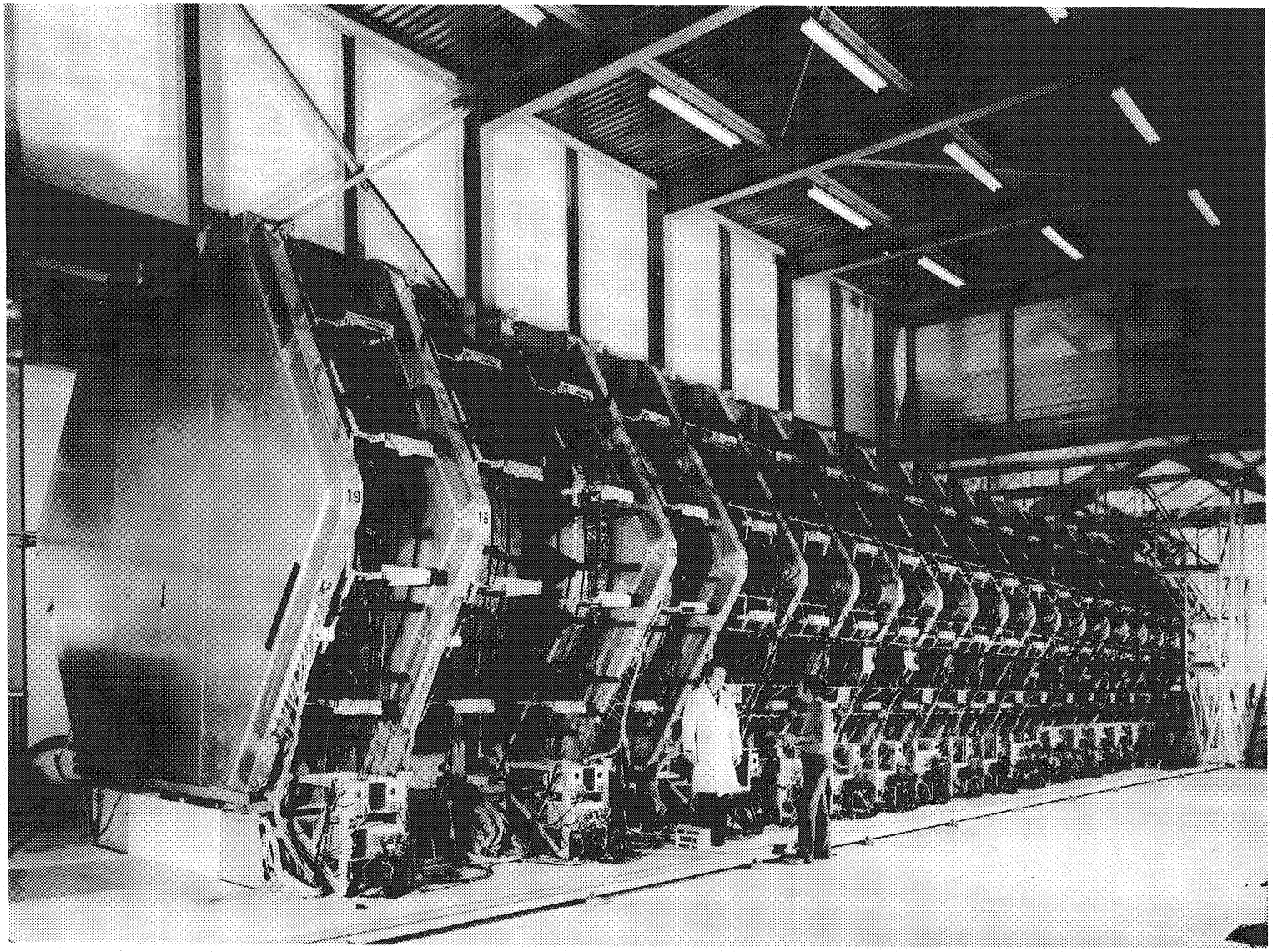

Fig. 38

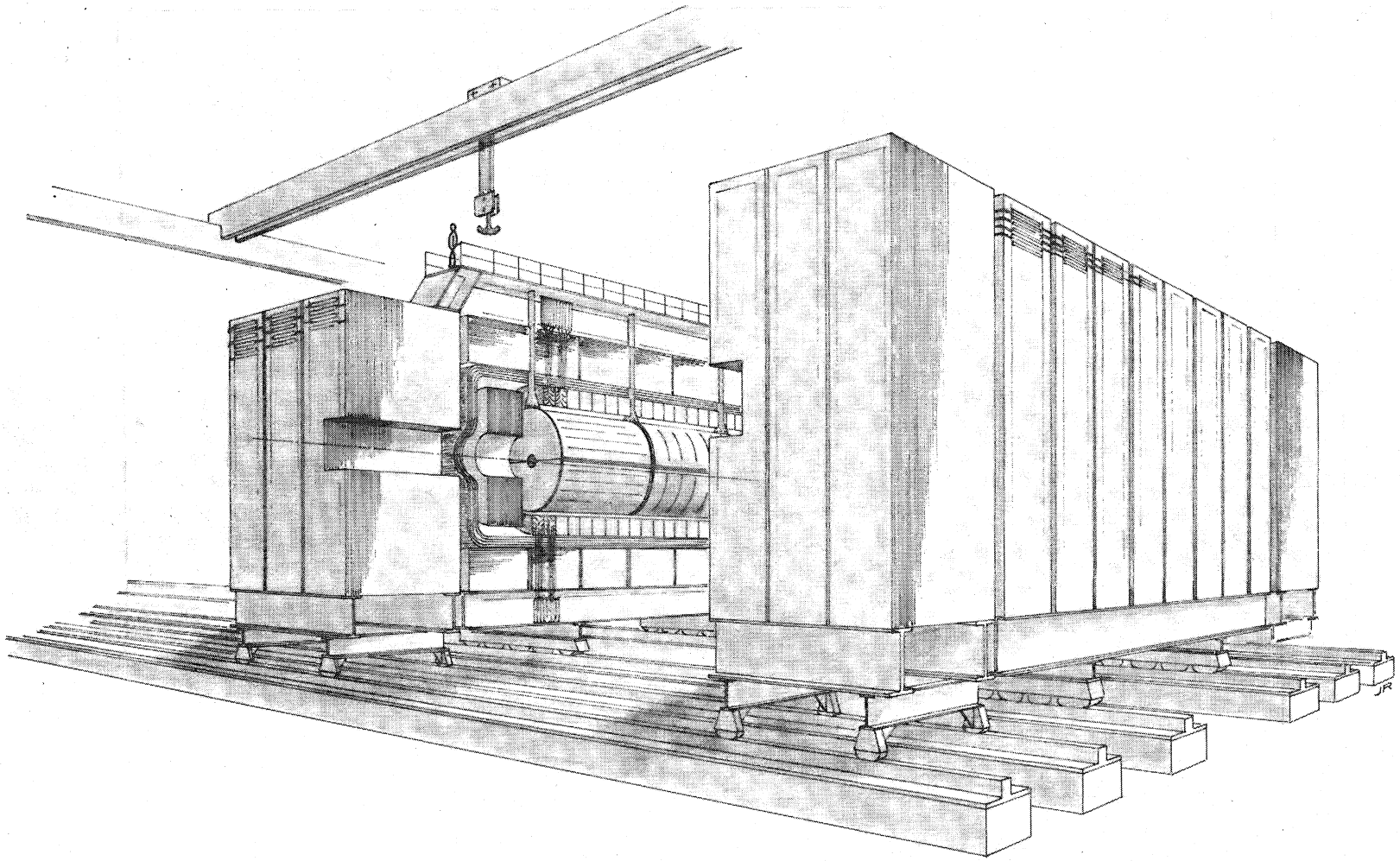

Fig. 39a

EXPERIMENTAL AREA FOR $P\bar{P}$ IN LONG STRAIGHT SECTION 5 OF THE SPS

_Vertical section in beam direction.

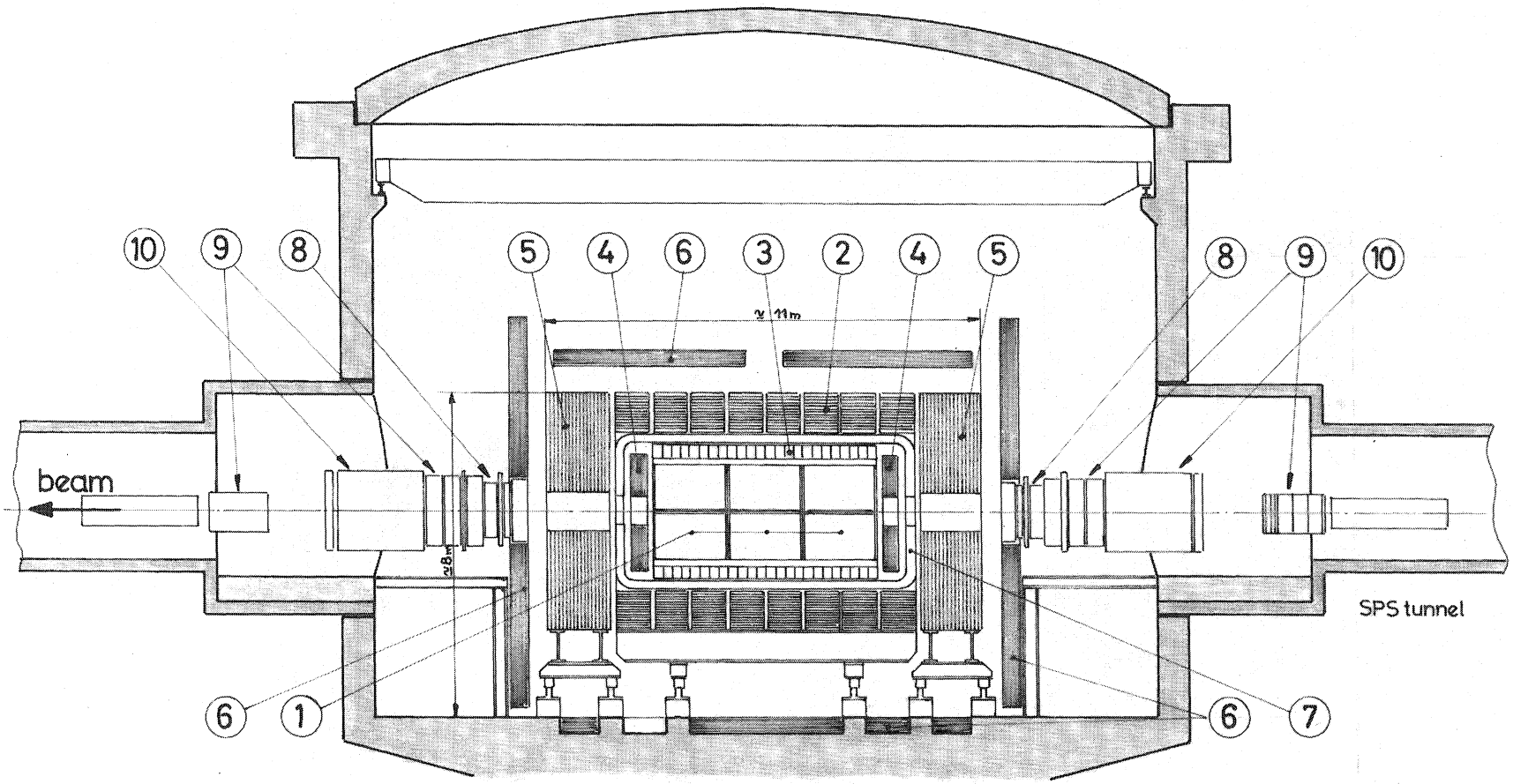

1. Central detector with image readout.
2. Large angle calorimeter and magnet yoke.
3. Large angle shower counter.
4. End cap shower counter.
5. End cap calorimeter.
6. Muon detector.
7. Aluminium coil.
8. Forward chambers
9. Forward shower counters and calorimeters
10. Compensator magnet.

Fig. 39b

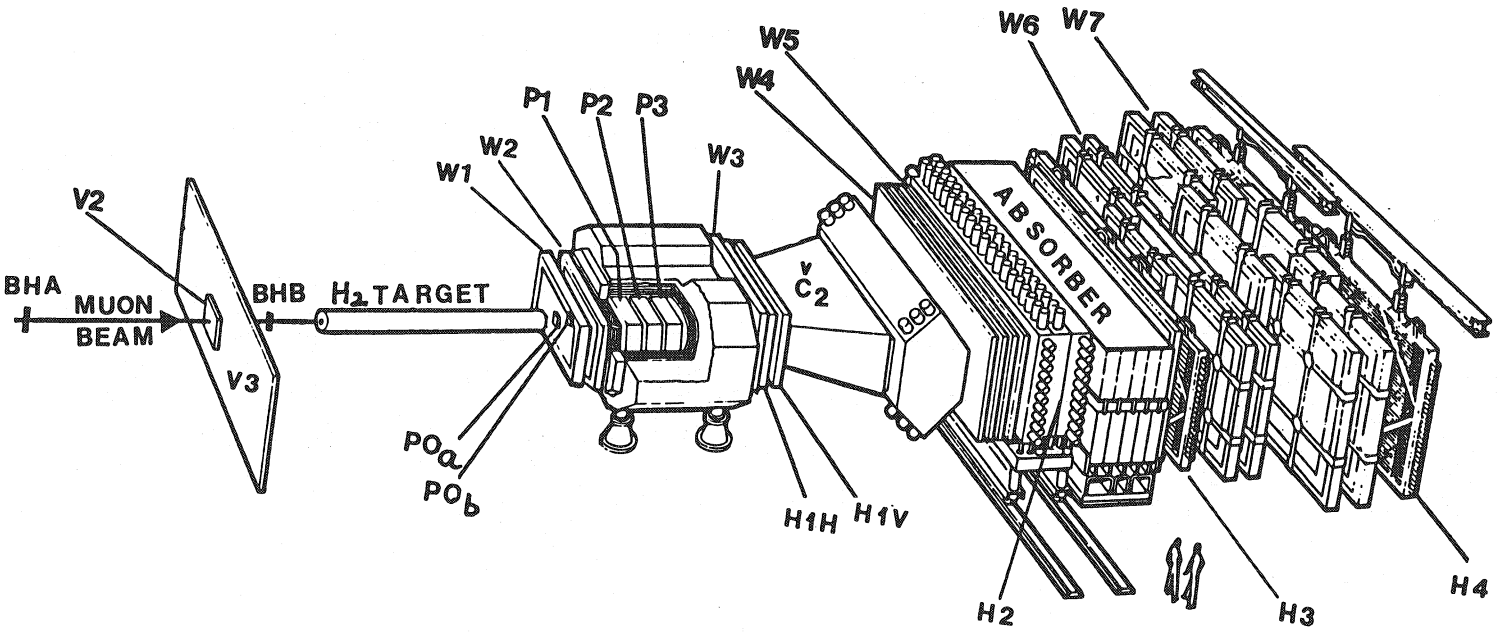
W5
W6
W7
W4
P1
P2
P3
W2
W1
W3
V2
BHA
MUON
BEAM
BHB
H2 TARGET
V3
V
C2
ABSORBER
POa
POb
H1H
H1V
H2
H3
H4

Fig. 40